SPINNING AN UNMAGNETIZED PLASMA FOR MAGNETOROTATIONAL INSTABILITY STUDIES IN THE PLASMA COUETTE EXPERIMENT

by

Cami Collins

A dissertation submitted in partial fulfillment of
the requirements for the degree of

Doctor of Philosophy

(Physics)

at the

UNIVERSITY OF WISCONSIN–MADISON

2013

Date of final oral examination: Dec 6, 2013

The dissertation is approved by the following members of the Final Oral Committee:

- Cary Forest, Professor, Physics
- Ellen Zweibel, Professor, Astronomy and Physics
- Jan Egedal, Assistant Professor, Physics
- Stanislav Boldyrev, Professor, Physics
- Hartmut Zohm, Honorary Professor, Physics (IPP Garching, Germany)

What imagination does is it allows us to conceive of delightful future possibilities, pick the most amazing one, and pull the present forward to meet it.

— J. Silva

Abstract

A new concept for creating a large, steady-state, fast flowing, hot plasma which is weakly magnetized has been demonstrated experimentally, marking an important first step towards laboratory studies of a wide variety of phenomenon important in plasma astrophysics. In particular, the magnetorotational instability (MRI) mechanism is of great interest for its role in generating the turbulence necessary for efficient outward transport of angular momentum in accretion disks. The instability has been the subject of extensive analytical and numerical investigations for several decades, yet experimental verification of the MRI remains elusive.

In the Plasma Couette Experiment, plasma is confined by a cylindrical "bucket" assembly of permanent magnets, arranged in rings of alternating polarity, to form an axisymmetric cusp magnetic field. The field is localized to the boundaries, leaving a large, unmagnetized plasma in the bulk. Plasma is produced with 2.45 GHz microwave heating, reaching $T_e < 10$ eV, T_i <1 eV, and $n = 10^{10}$-10^{11} cm^{-3}. The plasma is stirred using $\mathbf{J} \times \mathbf{B}$ forces in the magnetized edge region, where current is driven by toroidally localized, electrostatically biased hot cathodes. Torque can be applied at the inner or outer boundaries, resulting in a controlled, differentially rotating flow.

Mach probe measurements show that the azimuthal flow viscously couples momentum from the magnetized edge into the unmagnetized bulk. Collisional ion viscosity must overcome the drag due to ion-neutral collisions for the plasma to rotate. A self-consistent, rotation-induced radial electric field is also measured. Maximum speed limits have been observed for various gas species (He $\sim$ 12 km/s, Ne $\sim$ 4 km/s, Ar $\sim$ 3.2 km/s, Xe $\sim$ 1.4 km/s), consistent with a critical ionization velocity limit reported to occur in partially ionized plasmas. The experiment has achieved magnetic

Reynolds numbers of $Rm \sim 65$ and magnetic Prandtl numbers of $Pm \sim 0.2 - 10$, which are approaching regimes shown to excite the MRI in local linear analysis which incorporates dissipation, the Hall term, and momentum loss through ion-neutral collisions.

ACKNOWLEDGMENTS

Wow, what a ride! I am so incredibly fortunate to have been part of such a neat experiment for my graduate research. For that, I express deep gratitude to my academic advisor, Professor Cary Forest, whose excitement is contagious, positive attitude is impermeable, and advice is impeccable. I have grown so much from the many opportunities that he has provided for me to present and interact at conferences. From him, I have learned that nearly anything is possible, and that true understanding comes when you can predict, build, and measure it. He has pushed me to be better than I thought I was capable of being. I am grateful to have been surrounded by a group of some of the world's most talented scientists and engineers. I would like to thank John Wallace and Mike Clark; no matter how outrageous the ideas were, they found a way to make it work. Progress on this experiment would not have been possible without Dr. Noam Katz, who taught me the clever but "quick and dirty" approach to get things done, and Dr. Chris Cooper, whose spontaneous humor made me actually look forward to taking LIF data. I am grateful for the excellent work of the undergraduate researchers, especially Jon Jara-Almonte, Blair Seidlitz, Carl Wahl, and Ingrid Reese. I would also like to recognize the memory of Roch Kendrick, whose design and construction of the early phases of the experiment was nothing short of genius, and who provided the invaluable training that I needed to succeed in the laboratory.

Special thanks to Dale Schutte for his hours of hard work and dedication in finding equipment; he is the reason that UW-Madison is the best place for experimental plasma physics. Thanks to the members of MST who have so happily dropped what they were doing whenever I needed help throughout the years: The Hackers for all of the computer help, Abdul for tips on probe construction, Bill Z. for forcing me to take time out and enjoy a joke, Paul Nonn for sharing so many ingenious techniques and along with Steve Oliva, supplying the Xenon. Also thanks to

Mikhail and Dave in the electronics shop for repairing that blown-up Langmuir cart (several times), Steve Limbach for vacuum and puff valve advice, Joe and Steve in the machine shop for showing me the right way to machine things...Steve even let me into the shop on a Saturday just to spot weld! Ivan, thank you for coding and solving a problem in hours, which probably would have otherwise taken me months to figure out. I appreciate Prof. Fred Skiff, who so kindly gave us his time and loaned us the LIF equipment. Thank you to my defense committee members for the excellent comments and suggestions, and to Mark Nornberg for proofreading this thesis. I also had the pleasure of working for a summer at PPPL with Professor Hantao Ji, and I greatly appreciate his interest and support for me throughout my grad school career.

I am indebted to my parents, who have encouraged me ever since I set this goal in middle school, with Mom always saying that I've got nothing to lose by trying. Their financial support throughout college allowed me to focus entirely on my studies. They bought me new cars to ensure that I would safely make the long drive home to Montana (thanks, Dad!). My family would do anything for me, from driving me through whiteouts and ice-covered roads to get me to the airport for a conference, or driving across the country just to pick up my dog for a summer of dogsitting. The trips home for ice fishing, paddlefishing, fireworks, shooting, prime rib, BBQ ribs, endless hours of stories, and time with my nieces and nephews has lifted the stress of grad school when it was needed the most. Finally, I cannot imagine making it through this experience without my best friend, Zane, whose ability to make me laugh, unwavering patience, and steady-calm influence has provided comfort and memories that I cherish.

TABLE OF CONTENTS

Page

Appendix

Page

LIST OF TABLES

LIST OF FIGURES

Figure Page

Figure Page

Appendix
Figure

Appendix
Figure Page

Chapter 1

Introduction

1.1 The Mystery of Accretion

Virtually all astrophysical objects–from planets to stars, black holes, and galaxies– form through one common process: accretion. Due to gravity, interstellar gas and plasma collapses into a rotating disk, and matter then spirals inwards and accretes onto the central, point-like object. Accretion is thought to power some of the most luminous objects observed in the universe, including X-ray binaries, active galactic nuclei, and quasars. Multiwavelength observations often find accretion disks accompanied by well-collimated jets shooting out from the central region, spanning light years in distances that dwarf the disk itself. While direct imaging of less luminous protostellar disks is limited due to the distance and small size, spectroscopy often reveals excess infrared emission at longer wavelengths which cannot be coming from the star itself. Structural features of the disk can even be distinguished. For example, a dip in the emissions spectrum might suggest that the inner part of a disk is missing due to the formation of a planet [1].

In the accretion process, gravitational potential energy is converted to heat through friction, and a fraction of energy is radiated as light. A simple estimate of the expected disk luminosity can be made by assuming all kinetic energy of infalling matter is converted to radiation, resulting in $L = 2\eta GM\dot{M}/R$ where η is the radiative efficiency of gravitational energy release, G is the gravitational constant, M is the mass of the central object, $\dot{M}$ is the mass accretion rate, and R is its radius. Thus, accretion disks surrounding neutron stars or black holes can be especially bright.

When cast in terms of mc^2, the amount of energy released is astonishing: the efficiency of accretion can be $25 - 40\%$ in neutron star and black hole systems. In comparison, nuclear fusion converts only 0.7% of rest mass to energy [2].

The key question, though, is *why* does matter fall inward in accretion disks? The orbiting matter is Keplerian, where centrifugal forces are balanced by gravitation and $\Omega \propto r^{-3/2}$. Since angular momentum is conserved, one should expect that a perturbed particle would undergo periodic retrograde epicycles around its circular orbit if only gravitational forces are present. In order for matter to fall inward, there must exist an efficient mechanism for transporting angular momentum outwards. Ordinary viscous diffusion can transport momentum in sheared flows over a distance l on a timescale of order l^2/ν. Here, the kinematic molecular viscosity can be estimated as $\nu \sim \lambda_{mfp} c_s$, where c_s is the sound speed and $\lambda_{mfp} \sim (n\sigma)^{-1}$ with $\sigma \sim 10^{-15}$ cm^2. In an example for accretion around compact objects where $T \sim 10^4$ K, $n \sim 10^{16}$ cm^{-3}, and $l \sim 10^{10}$ cm, the calculated viscosity $\nu \sim 10^5$ cm^{2}s^{-1} gives expected timescales of around 3×10^7 years, orders of magnitude too long to explain observed accretion rates [2, 3, 4].

The first hint came in 1973, when Shakura and Sunyaev proposed that turbulent enhanced viscosity could account for the fast momentum transport in accretion disks [5]. The nature of viscosity in turbulent shear flow was first examined nearly a century ago by Boussinesq, Prandtl, and Taylor [6]. In turbulent shear flows, momentum can be carried by turbulent eddies, such that the enhanced "eddy viscosity" would be on the order of the root mean-square value of the fluctuating velocity times a characteristic mixing length scale. Transport through eddy viscosity can be orders of magnitude more efficient than molecular viscosity alone. Without specifying the source of turbulence, Shakura and Sunyaev developed the alpha disk model, where the turbulent disk viscosity can be parameterized as $\nu_t = \alpha c_\mathrm{s} H$, where c_s is the sound speed, H is the disk height (an upper limit for the size of the eddies), and α is a free parameter less than one. The equations of disk structure, including density, temperature, and radiated energy flux, may then be solved in terms of the α parameter.

The question of the underlying cause of turbulence in accretion disks has since been an intense area of debate in astrophysics [4, 7]. Accretion disks are at extremely high Reynold's number

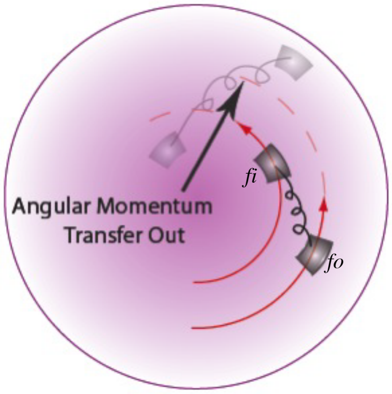

Figure 1.1: A mechanical analogy of the MRI mechanism. B acts like a spring connecting rotating fluid elements, fi and fo, in a disk where $d\Omega/dr < 0$. If fi is perturbed inward, momentum is transferred from fi to fo through B, causing fi to fall to smaller radii while fo moves to larger radii. B is then stretched further, causing runaway instability.

($Re > 10^{14}$), where $Re = VL/\nu$ is a dimensionless number representing the ratio of inertial forces to viscous forces (V is velocity, L a characteristic lengthscale, and ν is the kinematic viscosity). While many high Re shear flows exhibit hydrodynamic turbulence, the Keplerian rotation profile of accretion disks is linearly stable by the Rayleigh criterion. According to Rayleigh (1916) [8], inviscid flow is linearly unstable if the specific angular momentum decreases with radius ($d(r^2\Omega)/dr < 0$), a condition which is not satisfied in accretion disks. It remains unclear if nonlinear hydrodynamic turbulence can arise from nonaxisymmetric perturbations that destabilize the disk, or even if such turbulence would result in enough momentum transport on accretion timescales [9].

Perhaps the most important advancement in accretion disk theory was the realization that the presence of even a very weak magnetic field can dramatically change the stability properties of differentially rotating, conductive fluids or ionized gases (see Fig. 1.1). This powerful instability, the magnetorotational instability (MRI), was first derived by Velikhov in 1959 [10] and later Chandrasekhar [11], but it wasn't until the early 1990's that the MRI was invoked as the possible cause of turbulence in accretion disks [12].

Since then, a number of numerical simulations have confirmed that the MHD-turbulence generated from MRI can transport angular momentum outwards efficiently enough to explain observed accretion rates [13, 14, 15]. Unfortunately, simulations are not perfect. Present-day simulations are far from resolving all of the physics of astrophysical systems, from the smallest, dissipative scales to the largest. Direct numerical simulations of accretion disks are prohibitive, since the number of required floating-point operations grows as Re^3, and Re may be as high as 10^{14} in a protostellar disk. Simulations are limited to either local, shearing box models with periodic boundary conditions which mimic the local properties of accretion disks, or computationally expensive global simulations where local resolution is poor.

Numerical simulations generally have difficulty varying the ratio of viscosity and resistivity, a property described by the magnetic Prandtl number, $Pm = \mu_0 \sigma \nu$. Simulations for anything other than $Pm = 1$ are demanding because both the velocity and magnetic field dissipation scales must be resolved. However, it has been shown in recent MRI simulations that varying $Pm = 0.06 - 4$ can cause the magnitude of the MRI driven turbulent radial momentum transport to vary by two orders of magnitude [16]. These simulations suggest that the MRI may not be efficient at small Prandtl numbers. In nature, Pm varies by many orders of magnitude: for example, $Pm \lesssim 10^{-5}$ in disks around young stellar objects while $Pm \gtrsim 10^5$ around active galactic nuclei. Therefore, verifying and understanding turbulent transport as a function of magnetic Prandtl number is critical to accretion disk theory.

This is precisely why laboratory plasma astrophysics experiments are needed. While the existence of the MRI is widely accepted, experimental confirmation is an important part of the scientific process. A plasma experiment could create the MRI with $Pm = 1$, in which case simulation can resolve all of the critical scales in the parameter range of the experiment. The hope is that if the predictions for global behavior of MRI are observed in an experiment, the validated theory and code might be trusted when extrapolated to astrophysical parameters. From an experimental point of view, the ingredients for MRI seem simple: the classical derivation of the MRI says that a hydrodynamically stable Keplerian-like flow of a conducting fluid should suddenly be destabilized by a vertically applied, weak magnetic seed field. Despite its fundamental importance, the MRI has never been verified in a laboratory plasma.

The experimental observation of the linear growth of the MRI in a plasma would be a significant achievement in itself. Even more interesting is that, in a plasma experiment, it may be possible to generate multiple, non-axisymmetric modes leading to a fully saturated state of MRI turbulence, making it possible to measure the momentum transport through Maxwell and Reynolds stresses. The system could even evolve into a self-consistent state of an MRI dynamo, thus demonstrating the growth of magnetic field due to small-scale MRI turbulence. Along with comparison to simulation and relation to observation, a plasma MRI experiment could lead to an understanding of the fundamental behavior of the MRI and its importance in astrophysical systems, building insight for the generation of large-scale magnetic fields and the launching of large-scale jets in accretion disks.

1.2 Other MRI Experiments

The potential importance of the MRI has led to intense efforts to experimentally investigate astrophysically relevant flows, and substantial progress has been made in liquid metal MRI experiments. These experiments create Keplerian-like flows in liquid gallium or sodium using the Taylor-Couette geometry, where flow is driven between two concentric, differentially rotating cylindrical (or spherical) shells. A seed magnetic field is applied to the flows from external electromagnets, and magnetic probes, ultrasonic velocimetry, and torque measurements are used as diagnostics.

The Princeton MRI Experiment is a modified Taylor-Couette device in which liquid gallium is rotated between an inner and outer cylinder, and an axial magnetic field is applied [17]. Most recently, large-scale, large-amplitude, coherent, nonaxisymmetric velocity fluctuations have been observed when a sufficiently strong magnetic field is applied [18]. The instability appears starting from either hydrodynamically stable or unstable background flow states and creates angular momentum transport which modifies the azimuthal velocity prole. Contrary to the MRI, the instability appears at low rotation rates, and was identified as a free-Shercliff-layer instability caused by the axial magnetic field extending shear layers from the endcap boundaries. Fortunately, the instability is absent in regimes where the magnetorotational instability is expected to be observed. However, in order to reach the threshold parameters for observing the MRI, the experiment must operate with a fluid Reynold's number near $Re \sim 10^6$. An extrapolation of 3D global simulations has shown that the amplitude of MRI mode in the saturated state scales as $A \sim Re^{-1/4}$ [19]. The experiment has pushed to reach the threshold parameters for observing the MRI, but the predicted amplitude of the MRI instability is comparable to the measurement errors, and the MRI remains elusive.

At the PROMISE experiment in Dresden, Germany, liquid gallium is spun between copper cylinders, and a helical magnetic field is applied [20]. By using a helical field, the threshold for the onset of the MRI is dramatically reduced, and the MRI appears in the form of a traveling wave known as the Helical MRI (HMRI). In the experiment, a traveling wave did appear for a certain range of applied magnetic field that was qualitatively consistent with expectations for HMRI, although secondary flows created by boundary layers at the endcaps made it difficult to clearly distinguish between MRI stable and unstable state.

Strong magnetic and velocity fluctuations were also observed in the Maryland Spherical Couette Experiment, where liquid sodium flowed between a fixed spherical stainless steel outer vessel and a rotating inner copper sphere. When a large enough magnetic field was applied to an already hydrodynamically unstable, turbulent flow, additional non-axisymmetric fluctuations were observed and interpreted as signatures of the MRI. However, subsequent simulations have shown that the observed fluctuations are most likely due to instabilities of Shercliff and Stewartson layers at the boundary [21].

One of the major difficulties in liquid metal MRI experiments is that very high speed flows and strong magnetic fields are required to simply observe the instability. These flows are typically very turbulent and the behavior of the saturated state of the MRI can be significantly affected by undesirable secondary flows, e.g. Ekman pumping created by viscous boundary layers. Such high speeds are required because the MRI generally operates in the regime where the kinetic energy density of the flow is much larger than the magnetic energy density. In this limit, magnetic field lines can be stretched by the flow, but only if the conductivity is large enough. The generation of magnetic field relative to the dissipation by electrical resistivity is characterized by the dimensionless magnetic Reynolds number $Rm = \mu_0 \sigma V L$, or the product of the conductivity σ, the flow speed V, and the characteristic size L. In astrophysical plasmas, Rm is usually enormous, but in a laboratory liquid metal experiment, Rm is typically less than ~ 100; this value is barely large enough to reach the critical Rm for excitation of MRI or other flow-driven instabilities, such as the self-generation of magnetic fields through the dynamo.

While liquid metal experiments can be stirred mechanically and confinement of liquid-metal is straightforward, the medium suffers from several limitations. The use of plasma would allow faster flow speeds (km/s instead of m/s), resulting in larger Rm. Plasma has the distinct advantage in which viscosity can be varied independently of the conductivity, allowing the magnetic Prandtl number to vary from the liquid metal or protoplanetary disk regime ($Pm << 1$) to the regime of black hole or neutron star disks ($Pm >> 1$). Experimental control of Pm is important for understanding the nature of plasma turbulence and the dissipation range. Such high Rm and variable Pm of plasma could allow for studies of the MRI in the fully saturated, multimode, turbulent regime that liquid metal experiments are inherently forbidden to dream about. In addition, plasmas allow us to study effects beyond ideal MHD, such as the two-fluid effects involving the Hall term, plasma-neutral interactions, as well as compressibility. The two-fluid Hall effect is especially relevant in some protostellar disks [22, 23].

Thus far, flowing plasma experiments have been strongly magnetized, and the energy in these fields dominates the energy in the flow. The MRI experiment proposed in [24] used a magnetized plasma between two biased coaxial conducting cylinders, where $\mathbf{J} \times \mathbf{B}$ rotation was induced by the radial current and background axial magnetic field. Theoretical analysis shows the MRI can be excited at experimental plasma parameters, but the pulsed nature and complicated plasma equilibrium made analysis of magnetic fluctuations difficult [25].

The challenge, then, is to create a large, steady-state, fast flowing, hot plasma which is weakly magnetized; this combination of parameters is common for astrophysical and space plasmas [26] but has never been studied in a laboratory plasma.

1.3 A New Frontier in Laboratory Plasma Astrophysics

The goal for this experiment is to create a sufficiently hot, steady state, differentially flowing, unmagnetized plasma to study basic flow-driven instabilities especially important in astrophysics. These requirements contrast sharply with typical fusion plasma experiments; although fusion plasmas often exhibit high speed flows created intrinsically or driven through, for example neutral beam injection or biased electrodes, these plasmas are very strongly magnetized in order to reach desired high temperatures and confinement times necessary for fusion reactions. It is not trivial to create weakly magnetized, high-Rm plasmas in the laboratory, because magnetic fields are generally needed for confinement in order to make the plasma hot (σ) and dense (ρ). Secondly, one needs a clever way to drive flow in an unmagnetized plasma.

This thesis presents the creation of an experimental plasma device that can now be used to study flow driven instabilities, such as the MRI, for the first time in a plasma. The concept relies upon a highly localized magnetic field provided by axisymmetric rings of permanent magnets on the plasma boundary. The high-order multipolar magnetic field provides confinement, but drops off quickly with distance from the wall so that the core of the plasma is unmagnetized. The confinement scheme is a variant on the multipole confinement geometry first investigated by MacKenzie, Leung, Hershkowitz and others [28, 29, 30, 31], but differs in that it is axisymmetric.

The edge of the plasma is then stirred by applying $\mathbf{J} \times \mathbf{B}$ torques with current driven by electrostatically biased electrodes in the magnetized edge region. In part, the stirring scheme was motivated by electrode biasing experiments that have been used to control rotation in many magnetized plasma configurations, including mirrors [32], tokamaks [33], reversed field pinches [34, 35], plasma centrifuges [36] and other devices [37].

It has been successfully demonstrated that viscosity couples the azimuthal flow inward to the unmagnetized region. Measurements of the flow profiles match the profiles predicted by a model that includes Braginskii viscosity and momentum loss through ion-neutral charge exchange collisions. The flow is optimized at low density (where viscosity is largest) and a low neutral pressure

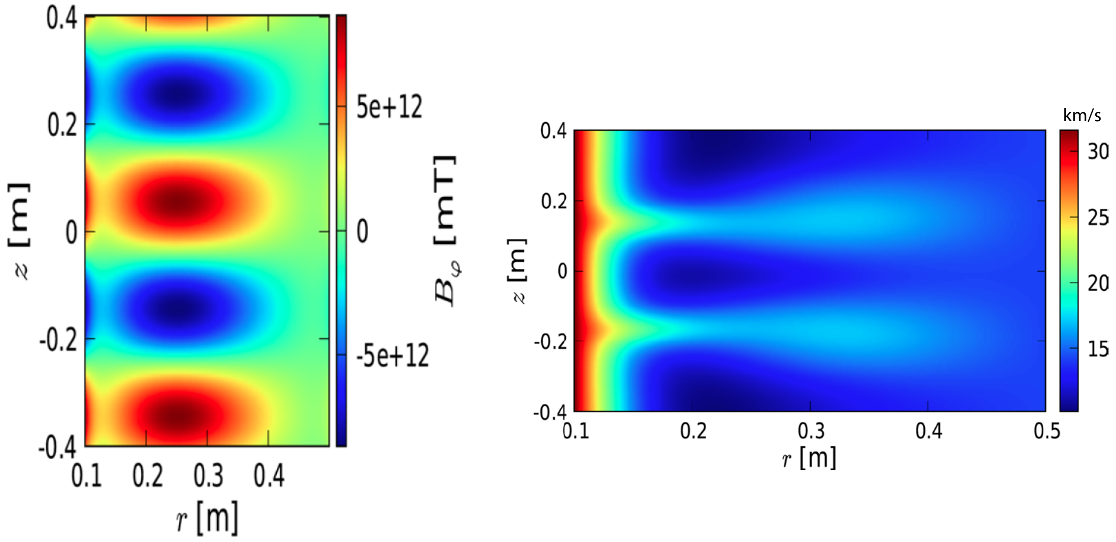

(a) (b)

Figure 1.2: What would the MRI look like in PCX? a) Global magnetic mode structures (for example, in B_ϕ) should appear during the linear growth stage of the Hall-MRI b) A modified azimuthal flow profile should appear during saturation of the Hall-MRI (here, $Pm = 0.5$, $B = -20$ Gauss). Figures taken from [27].

(where neutral drag is minimized). This work was published in a Physical Review Letter, [38], and a description of the experiment has been published in [39].

This experiment has already achieved $Rm \sim 65$ and $Pm \sim 0.2 - 10$, which is approaching regimes shown to excite the magnetorotational instability in local linear analysis and global Hall-MHD numerical simulations [27]. These simulations predict that the MRI should appear through global mode structures and modifications to the velocity profile, as shown in Fig. 1.2. The instability has not yet been measured in the experiment; the next stage will require further parameter optimization and additional probe arrays to carefully characterize the onset of MRI.

The demonstration of sheared flow of plasma in the unmagnetized core region, driven by biased electrodes in the magnetized plasma edge, is a major advance for carrying out future flow-driven MHD experiments to model astrophysical plasmas. The flow drive technique is now being implemented in a much larger, spherical geometry in the Madison Plasma Dynamo Experiment [40], which is well-posed to study magnetic field generation through both small and large scale dynamo action.

1.4 Thesis Overview

This thesis work involved the construction of an entire experiment which has culminated in the successfully demonstration of the first ever Couette flow of unmagnetized plasma. This work began with a completely empty room and required the design and implementation of everything from the vacuum system and machine control, to robotic probes and associated circuitry, to data acquisition and software analysis routines. A new method of data acquisition using MDSPlus long-pulse extensions was developed with the assistance of Mr. Jonathan Jara-Almonte. A hot filament, electrostatic stirring system was invented with the help of Dr. Noam Katz, and several novel optical diagnostics were also developed, namely Optical Emission Spectroscopy (with Mr. Blair Seidlitz and Dr. John Boffard) and a Laser-Induced Fluorescence system (with Dr. Chris Cooper and Prof. Fred Skiff). The analytic theory, which seems to very accurately describe the plasma behavior, has also been developed here. The thesis is organized as follows:

Chapter 2 describes the important components of the experiment apparatus, including the magnets, electrodes, vacuum system, microwave heating, data acquisition, and diagnostics. In order to create the sheared flow necessary to excite the MRI, rotation must also be induced at the inner boundary, which required construction of a removable centerpost assembly of magnets and stirring electrodes. Plasma parameters such as velocity, T_e, n_e, V_{float} were mainly measured with probe-based diagnostics, but non-perturbative methods of Optical Emission Spectroscopy and Laser-Induced Fluorescence were also explored. Basic characteristics of the microwave heated plasmas are also presented.

Chapter 3 discusses the development of the rotation drive technique. A long series of experiments revealed that biased, hot cathodes work best for flow drive, and efficient rotation was obtained by optimizing electrode position and plasma discharge characteristics. Unmagnetized and magnetized viscosity, based on Braginskii's 1965 derivations, is discussed, which is important for understanding the viscous coupling of momentum from the edge to the unmagnetized bulk plasma. Much effort was made to maximize induced flow, and apparent maximum velocity limits are reported.

Chapter 4 presents a model for understanding the plasma equilibrium in the unmagnetized bulk, based on the momentum equation which includes unmagnetized Braginskii viscosity and momentum loss through ion-neutral charge-exchange collisions. Velocity fits are in good agreement with the velocity measurements, and Braginskii viscosity is verified up to a factor of T_i (which is difficult to accurately measure in the experiment). When the rotation drive system was extended to include all four cathodes at the outer boundary, uniform, solid-body rotation spanning the entire height of the plasma was obtained. Measurements of an expected radial electric field due to plasma rotation are also presented.

Chapter 5 explores the possibility of generating either hydrodynamic or magnetohydrodynamic instability. It is known that Couette flow, with rotation driven exclusively at the inner boundary, can become hydrodynamically unstable and exhibit large-scale, secondary flows in the form of axisymmetric vortices. The MRI could be reached by spinning at both the inner and outer boundaries, creating a flow which is hydrodynamically stable but then destabilized by an applied vertical seed field. Stability analysis includes resistive and viscous dissipation, the Hall term, and the drag due to ion-neutral charge exchange collisions. It is pointed out that the current regime in which the experiment is operating may be close to MRI unstable, but slight changes in parameters (n_e, T_i, or neutral pressure) can dramatically alter the viscosity and flow profiles, making it more difficult to reach the MRI unstable regime. Prospects for future MRI experiments are discussed.

Finally, Chapter 6 presents a summary of the most significant accomplishments of this work, along with suggestions for future work. Additional details concerning data acquisition, diagnostics, and measurements of the magnetized cups region can be found in the Appendices.

Chapter 2

Experiment Apparatus

The concept for the Plasma Couette Experiment (PCX) described in this thesis is to confine plasma by a cylindrical bucket assembly of permanent magnets, arranged in rings of alternating polarity, to form an axisymmetric cusp magnetic field. The field quickly vanishes away from the boundaries, leaving a large, unmagnetized plasma in the bulk. The novelty is to stir plasma using $\mathbf{J} \times \mathbf{B}$ torques, where current is driven by electrostatically biased electrodes in the magnetized edge region, and allow plasma viscosity to couple the momentum inward to the unmagnetized bulk.

This chapter presents the construction of the entire experiment from scratch. The major components of the experiment (pictured in Fig. 2.1) are described, including the vacuum vessel, magnet assembly, electrode stirring assembly, and microwave heating. Many of the advanced plasma diagnostics and data acquisition techniques developed in the fusion community have been applied here, and several optical diagnostics have also been developed.

2.1 Cusp Confinement

The idea of using multicusp, or multipole, magnetic fields of permanent magnets to confine a plasma has existed for at least 40 years [41]. Cusp confinement limits plasma losses by effectively reducing the loss area through magnetic mirroring. It has been shown that the confinement time of primary (ionizing) electrons is significantly increased, along with improved confinement of bulk plasma [29]. Density and temperature gradients are restricted to regions of strong magnetic fields at the boundaries, leaving a large, quiescent, uniform plasma in the unmagnetized bulk. The actual

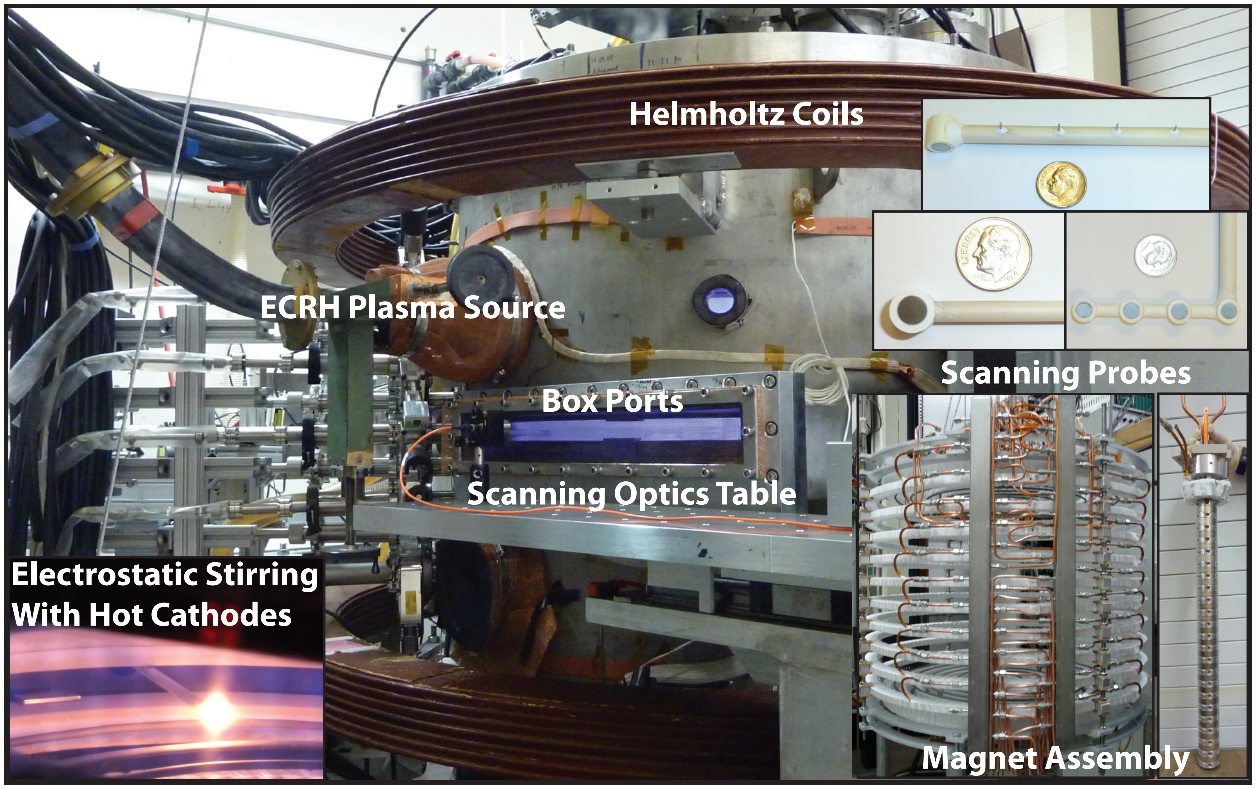

Figure 2.1: Major components of the Plasma Couette Experiment.

cusp loss area is not well understood, but experiments and the best available theory have previously suggested that the loss width is $w \approx 4\sqrt{\rho_e \rho_i}$, where ρ_e and ρ_i are the electron and ion gyroradii at the magnet face. Assuming $B_r = 1$ kG at the face, $T_i = 0.1$ eV and $T_e = 8$ eV, the total loss area to the magnets in PCX is only 0.079 m^2 for argon and 0.045 m^2 for helium plasmas.

Unlike many other multicusp experiments where the magnets are arranged in non-axisymmetric grids or vertical lines, the PCX magnetic bucket has *axisymmetric* magnet rings providing a purely poloidal field. A schematic of the magnetic field geometry is shown in Fig. 2.2. In this axisymmetric arrangement, the ∇B, curvature, and $E \times B$ drifts are all toroidal and serve to equilibrate the potential in this direction. This allows us to use toroidally localized electrodes to induce $\mathbf{J} \times \mathbf{B}$ toroidal rotation, as discussed in Chapter 3.

2.1.1 Magnet Assembly

Confinement is provided by a cylindrical assembly of permanent magnets, arranged in rings of alternating polarity, to form an axisymmetric cusp magnetic field. The entire water-cooled magnet assembly is installed inside the vacuum vessel, and cooling must be sufficient to keep the magnets below the approximate 150°C Curie temperature, which ultimately limits the plasma pulse length. The “magnetic bucket” creates a large, mostly unmagnetized cylindrical plasma volume that is approximately 40 cm in radius and 60 cm long, as shown in Fig. 2.2. The top, bottom, and outer rings of permanent magnets consist of 1.5 kG, 7/8” diameter ceramic grade C8 magnets fastened with epoxy to water-cooled aluminum rings (see Fig. 2.4b).

A central column of magnets (pictured in Fig. 2.3, with more details in Fig. 2.9), which defines the inner plasma boundary, is used to achieve Couette rotation (sheared flow between two cylinders). The center post assembly consists of 22 radially magnetized, 5.5 cm o.d. NeBFe magnet rings, stacked in alternating polarity and separated by aluminum clamps. The aluminum center rod is water cooled to prevent magnets from overheating. The center post magnets were initially covered by a clear, 6.02 cm o.d. quartz tube. It was found that even though the center post magnets were water cooled, magnet surfaces still reached high temperatures ($\sim$ 120°C during plasma discharge) due to the high radiant heat flux from the nearby center post filaments. Therefore, the

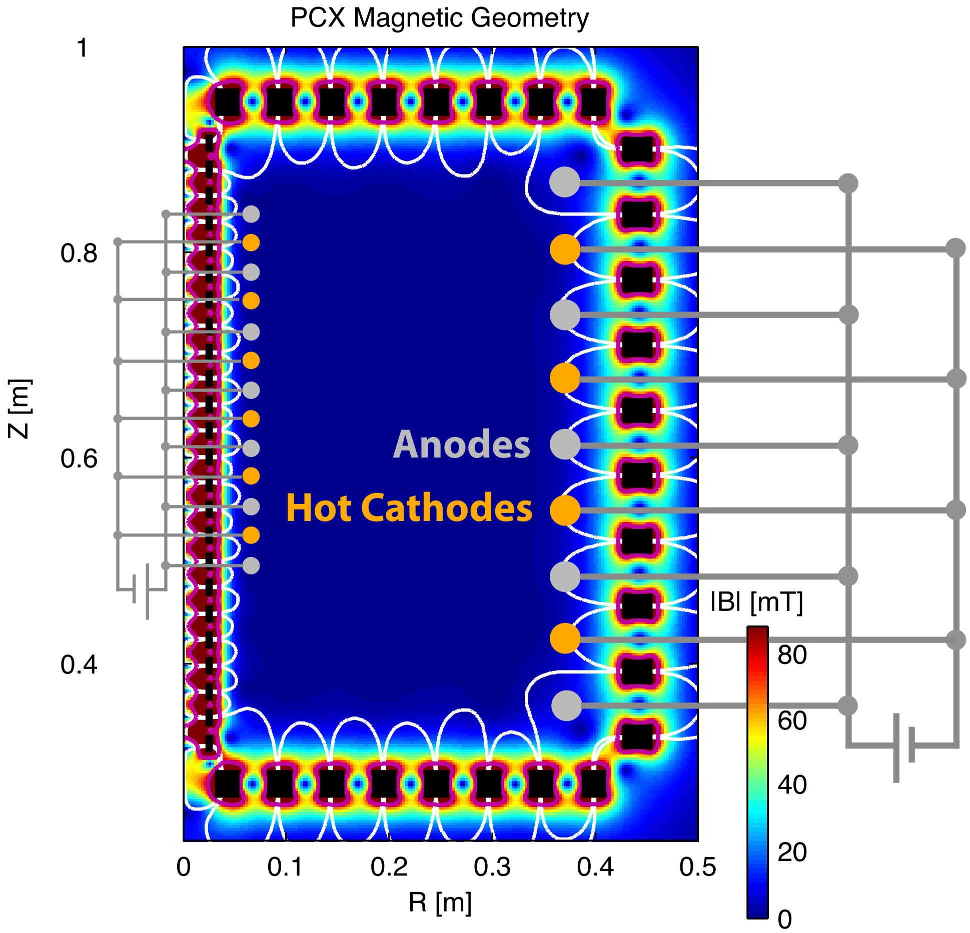

Figure 2.2: Cross section of the PCX magnet and flow drive geometry, showing strong magnetic fields at the boundaries, large unmagnetized bulk, and the toroidally localized electrodes for flow drive.

inside of the clear quartz tube was coated with silver to reflect thermal radiation and act as a heat shield. The heat shield has resulted in acceptable magnet temperatures of $< 60°\mathrm{C}$ during operation.

The 10 outer magnet rings are spaced vertically 6.17 cm, the 22 center stack magnets are spaced vertically 2.77 cm, and the 8 concentric endcap magnet rings are spaced radially 5.08 cm. The magnet ring spacing was chosen to minimize the simulated magnetic field at the center of the device yet still allow for maximal alignment to ports for insertion of probes between the rings. The magnetic field in Fig. 2.2 was simulated using Ansoft Maxwell SV software, which uses finite element analysis to solve for the 2D magnetostatic field. The simulated field seems to overestimate the magnitude of the magnetic field when compared to measurements with a handheld gaussmeter, but agrees within 10%. A fit of the Maxwell simulated vertical magnetic field at the midplane is

$$B_z(r) = 0.0452e^{((r-R_o)/0.0259)} + 0.099e^{(-(r-R_i)/0.0084)} \;\; [\mathrm{T}] \tag{2.1}$$

where the inner and outer magnet boundaries are $R_i = 0.032$ m and $R_o = 0.423$ m.

It is important to maintain an electrically insulating boundary condition at the magnet faces. Otherwise, the $\mathbf{E} \times \mathbf{B}$ rotation would not work, as the electric field applied across the magnetic field would short out. Initially, each magnet ring was electrically isolated from the plasma with a silica-based insulating cloth wrap. This quartz tape seemed to be a limitation on the vacuum conditions since the fabric represents a large, hydrophilic surface area that requires extensive baking to pump down, but also outgases when plasma is formed. A second generation of insulating limiters, which are made of aluminum coated with alumina (plasma sprayed by Thermal Spray Technologies, Inc), appear to have much better vacuum properties. Over time, the insulating boundaries can become coated with a conductor, e.g. tungsten evaporating from hot filaments. Cleaning is a tedious process which requires an entire deconstruction of the machine to remove the main magnet cage assembly. The outer limiters can be cleaned with Alconex detergent and Scotch-Brite pads. Deposits on the center post quartz tube can be buffed using the Dremel tool with an abrasive pad and plastic polish.

Finally, an external set of Helmholtz coils has been installed to apply a uniform, vertical magnetic field to the entire plasma volume (pictured in Figs. 2.1 and 2.3).

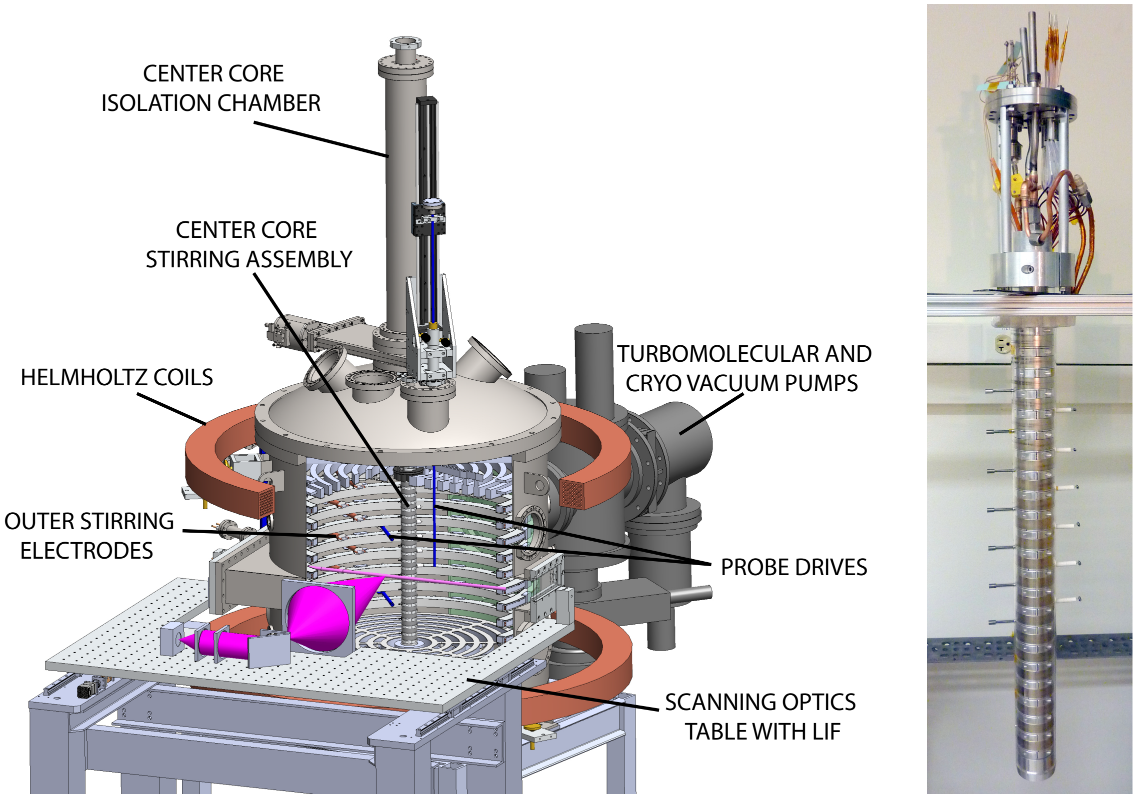

Figure 2.3: Left) Schematic showing the major hardware components and cut-away view of the vacuum chamber. Right) Photo of the center post assembly of magnets and stirring electrodes.

2.2 Vacuum System

The internal, water-cooled permanent magnet assembly is housed in a 1 meter diameter, 1 meter tall cylindrical stainless steel vacuum vessel. Various sized ports are available for diagnostics, plasma sources, electrical, water, and gas feedthroughs. Large boxports are available for optical diagnostics, and the boxport windows are made of Technical Glass Products, Inc. commercial grade fused quartz, which has $> 90\%$ transmittance from 280-2500 nm. The high vacuum is provided by a cryopump (CTI-Cryogenics Cryo-Torr 8) and a turbomolecular pump (Varian Macro-Torr 1000HT Turbo-V), and an automated vacuum control system is in place for emergency valve control.

A 20 kW deionized water cooling system has been installed for the internal permanent magnets and microwave plasma source. The intricate magnet assembly manifold has been leak-checked through both vacuum testing and pressure testing with 40 psi helium. Water conductivity is monitored by an electronic meter to prevent water conductivity from becoming too high (which could introduce ground loops) or too low (to prevent corrosion). To assist with pump-down, heat tape is used to bake the the outer vessel to about 50°C. The internal magnets can also be heated to about 40°C by circulating initially-room-temperature water through the cooling lines and allowing the pump to heat the water.

The base pressure is usually around 1×10^{-6} Torr but has reached 2×10^{-7} Torr in the past. To create plasma, gases such as helium and argon are back-filled through a needle valve to pressures of $10^{-6} - 10^{-4}$ Torr. Gas can also be puffed into the chamber through a computer controlled piezoelectric puff valve. Pressure is measured by a Penning cold-cathode gauge and converted by gas multiplication factors (He × 5.56, Ne × 3.3, Ar × .775, Xe × 0.348). Pressure is converted to neutral density by assuming the neutrals are at room temperature:

$$n_0[\mathrm{m}^{-3}] = 3.3 \times 10^{22} \times P[\mathrm{Torr}] \tag{2.2}$$

A residual gas analyzer is also available to track partial pressures of contaminant gas, which is usually dominated by water vapor.

The center post assembly of magnets and stirring electrodes requires regular cleaning and filament replacement. In order to facilitate efficient center post maintenance, a clever system has been installed to isolate the center core from the main chamber (see Fig. 2.3). A pulley mounted on the ceiling is used to raise the center post into a separate chamber via a sliding vacuum o-ring seal. A gate valve is then closed, so that the high vacuum in the main chamber is preserved while the isolation chamber is brought to atmospheric pressure. The entire center post and "garage" can be removed, lowered to floor level for repair, reinstalled, and returned to vacuum.

2.3 Data Management

PCX machine control, measurement, data acquisition, and analysis is achieved through a sophisticated integration of multiple devices running multiple software tools, including MDSPlus, LabVIEW, and Matlab. The MDSplus software is widely used for data management in magnetic fusion energy research. In MDSplus, data is stored into a hierarchical "tree" structure, and remote MDSplus clients can efficiently read or write data to the MDSplus server without file transfers. PCX is one of the first experiments to implement long-pulse extensions in which multiple segments of data are stored under a single shot file, allowing us to continuously read, write, and analyze data for very long periods of time (typically hours).

The PCX data acquisition system is based on a combination of a National Instruments CompactRIO Real-Time system with a variety of input/output modules, and a DTACQ system capable of up to 96 channels of simultaneously sampled analog input. An illustration of the various components of the PCX data acquisition system can be found in Appendix A. The CompactRIO data is stored in the "pdp" MDSplus tree at 100 samples/sec with 1 second per segment, while the DTACQ data is stored in "pcxdata" MDSplus tree at 10,000 samples/sec with 8 seconds per segment.

Revision management is provided by Perforce software, allowing users to store all changes in the revision history log, and files can be reverted to an earlier state if needed. The PCX Control computer is backed-up weekly to a mounted external hard drive. MDSplus data is backed up nightly to a 7 TB, RAID 5 array ("PCX Data") and can be accessed on the local campus network for analysis with Matlab or IDL.

A detailed guide to the PCX data acquisition system, which includes a complete description of the MDSplus tree hierarchy, configuration codes, descriptions of LabVIEW VIs, and guides for machine operation and program modification, can be found online at the UW Plasma Physics PCX Wiki (http://hackserver.physics.wisc.edu/wiki/index.php/PCX).

2.4 Plasma Heating

2.4.1 LaB$_6$ Plasma Source

Initially, a large area, coaxial Lanthanum Hexaboride (LaB$_6$) cathode was developed to produce fast primary electrons which ionize and heat the plasma (see Fig.2.4a). A summary of the measured plasma parameters for various values of cathode bias and neutral fill pressures is shown in Fig. 2.5. LaB$_6$ cathodes have previously been used to produce high densities (10^{12}cm^{-3}) and temperatures (T_e ∼10 eV) in other devices [42, 43]. In PCX, heating the coaxial LaB$_6$ plasma source to the optimal operating temperature for thermionic emission was not trivial. The graphite heater filament was short-lived (due to evaporation), which prevented operation at the desired temperatures of 1700°C. Radiative heating caused some magnet temperatures to reach 150°C, and outgassing from the silica tape covering the magnets caused neutral pressures to rise, resulting in undesirably low ionization fractions of $< 1\%$. A considerable fraction of neutral gas was water vapor, as noted by the residual gas analyzer. It was also found that the plasma potential was set by the bias applied to the LaB$_6$ cathode, which complicated the system by coupling the plasma source to the stirring electrodes. While the large area LaB$_6$ cathode as a plasma source was abandoned on PCX, the technology continued to be developed, and coaxial LaB$_6$ stirring cathodes are now being used successfully on the Madison Plasma Dynamo Experiment.

2.4.2 Microwave Heating

Plasmas generated by microwaves are especially useful in industrial plasma sources, particularly in materials processing or plasma etching applications where reactive gases would otherwise quickly degrade biased filaments in hot-filament powered discharges. Microwaves have been applied to various other multicusp magnetic field configurations, where low pressure, high density

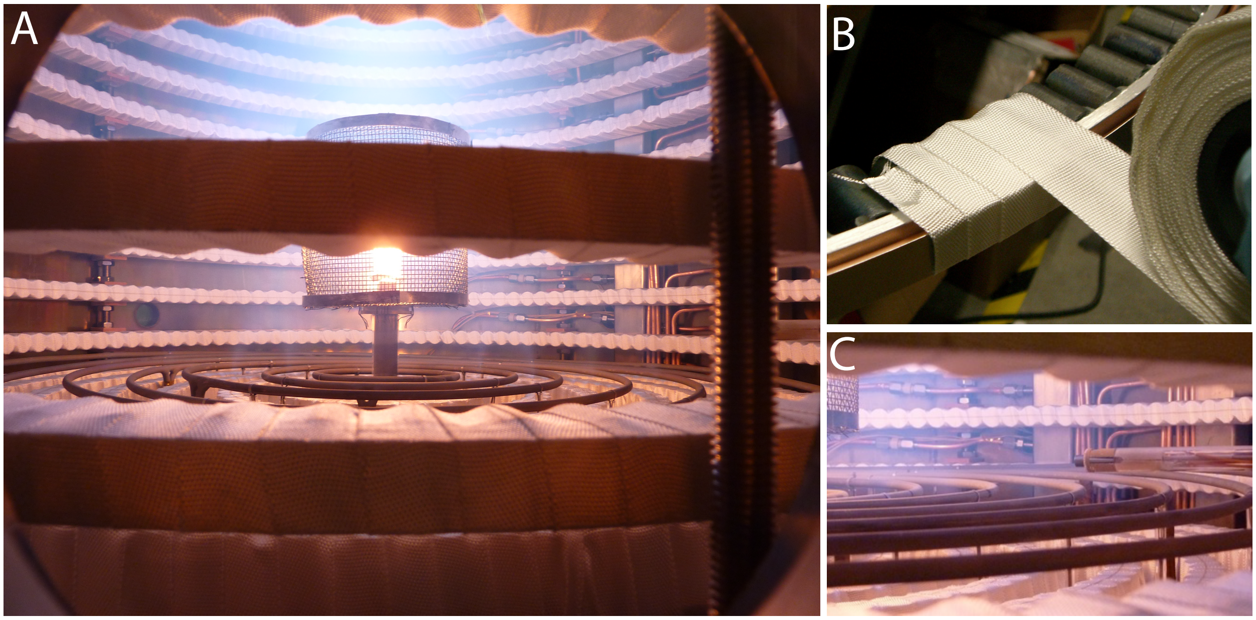

Figure 2.4: a) Argon plasma produced by LaB_6 source. b) Individual ceramic magnets epoxied to an aluminum ring with copper cooling lines held by a stainless steel band. Silica cloth has since been replaced by alumina-coated aluminum limiters. c) Early version of a radially scanned Mach probe during initial rotation drive experiments with cold electrodes.

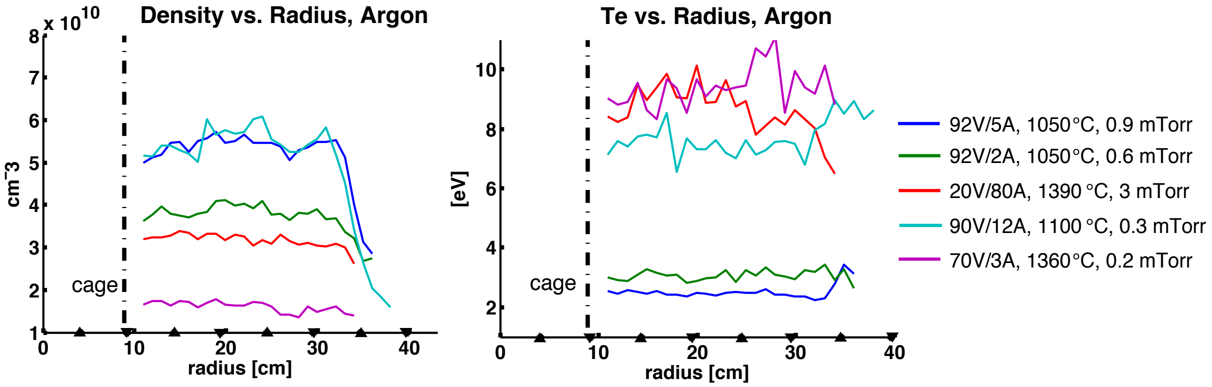

Figure 2.5: LaB_6 plasma density and temperature vs. radius for various cathode temperatures and bias voltages, as measured by a single tip swept Langmuir probe.

plasmas are produced through electron cyclotron resonance heating (ECH) [44, 45] or surface waves [46]. Microwaves cannot penetrate the plasma if it is overdense, because the wave is reflected at the plasma surface due to the skin effect and becomes an evanescent wave. This implies an O-mode cutoff density limit at $n_e = 7.4 \times 10^{10}$ cm^{-3} for 2.45 GHz microwaves. In practice, microwave plasmas can reach densities higher than the cut-off value. One alternative is to launch X-mode waves, which can sustain the discharge through absorption of power at the upper hybrid resonance layers. Overdense plasmas can also be produced in surface wave discharges, where the boundary between a column of plasma and a surrounding dielectric surface can act as a waveguide to support electromagnetic surface wave. Energy is transferred from the electromagnetic field to the plasma electrons, which then transfers power to the plasma through ionization and excitation collisions.

In PCX, the most effective technique for creating plasma suitable for flow-driven experiments has been microwave heating. The plasma is created and sustained with microwaves using a 6 kW, 2.45 GHz Cober Electronics magnetron. Microwaves in TE_{10} mode are guided by a rectangular waveguide to the chamber, and forward and reflected power are monitored by transducers mounted on the waveguide. An electrical isolation (DC) break in the waveguide connection between the microwave power supply and the chamber was made with a thin piece of insulating paper and plastic screws. Microwaves enter the multicusp magnetic cage through a WR-284 waveguide vacuum window, cut off to be flush with the plasma-facing surfaces of the side magnet rings. Because the horn is less than a microwave wavelength away from the plasma, an E-H tuner is necessary to match the impedance of the plasma and reduce the reflected power. The tuning depends on neutral pressure, plasma density, plasma temperature and vacuum condition, and has to be optimized as these quantities change. The face of the microwave horn is covered by a corrugated boron-nitride plate to prevent the plasma from expanding into the waveguide. It was found that the boron-nitride plate was essential, because without it the plasma ‘flickered’ with many sharp fluctuations in density.

At the microwave frequency of 2.45 GHz, electrons are resonant at 875 Gauss. Since the bulk of the chamber is unmagnetized, the resonance location occurs very close to the magnet rings. The

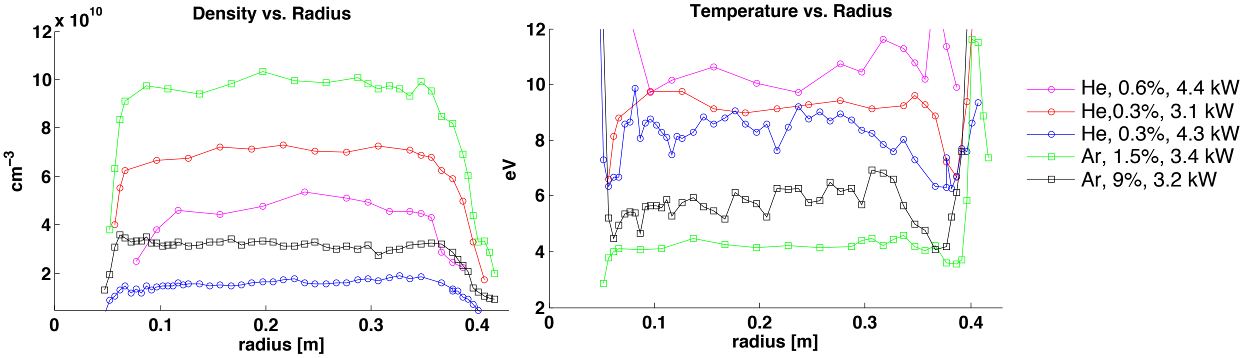

Figure 2.6: Typical radial profiles of density and temperature (measured with a single tip swept Langmuir probe) with ECH heating in helium or argon for various ionization fractions and microwave power.

location of the resonance is indicated by a white line in Fig. 2.2. As shown in the figure, the stronger magnets of the center column have a continuous resonance surface—in contrast with the endcap and outer boundary ceramic magnets—and this surface is farther away from the inner boundary. The actual excited wave mode structure is complicated by geometry. The waveguide launches mostly O-mode, with k$\perp$ B and E $//$ B, though there may be a small component of E $\perp$ B due to the curvature of the magnetic field. Reflections in the chamber can generate interference of waves that can significantly affect absorption. There are also radial density gradients, and electron gyromotion is complicated by magnetic field gradients. The degree of microwave power absorption, especially at the outer magnet cage surfaces, is unclear since the scale length of the resonance surface is smaller than the microwave wavelength.

Nonetheless, the heating and confinement is effective enough to create plasmas with temperatures up to 10 eV and densities ranging from $1 \times 10^{10} - 2 \times 10^{11}$ cm^{-3}, well about the cutoff density limit. Examples of typical radial profiles of temperature and density are shown in Fig. 2.6. Parameters are relatively flat throughout the bulk, unmagnetized region. Density and temperature gradients occur in regions of strong magnetic fields at the boundaries, where the magnetic field is $>$ 30 Gauss for $r < 0.08$ m and $r > 0.35$ m.

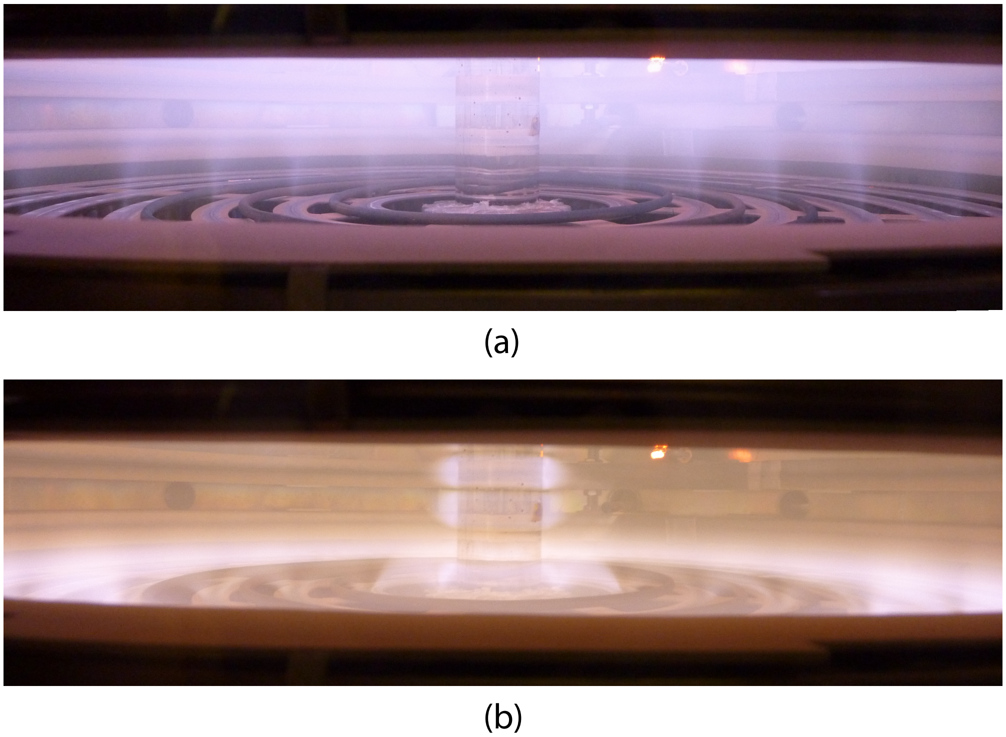

Figure 2.7: Significantly different emission properties are observed in an (a) overdense vs. (b) underdense plasma.

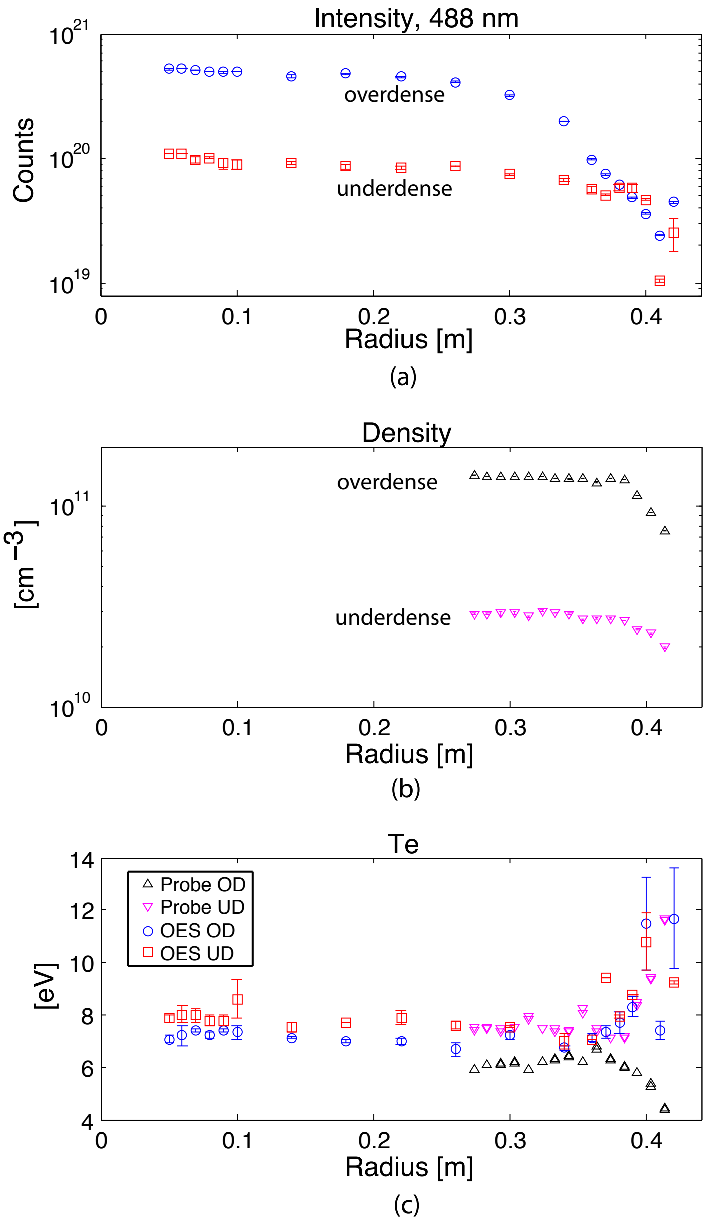

Figure 2.8: Comparison of overdense and underdense midplane profiles at different times during a puffed argon plasma (Shot #644). a) 488 nm emission intensity measured by spectrometer. b) Triple probe density. c) T_e measured by triple probe and Optical Emission Spectroscopy. In the underdense state, both diagnostics agree that T_e increases at the magnetized edge. In the overdense state, it is not clear if T_e increases or decreases at the edge.

The plasma appears to have two distinct states in which the spatial distribution of plasma emission changes significantly (see Fig. 2.7 for photos). The state strongly depends on the neutral gas pressure and input power (which control plasma density), and a sharp transition between states occurs when the electron plasma density falls below the microwave cutoff density limit. In the overdense state, the plasma exhibits bright emission from the central, field-free region of the plasma, and cusp losses can clearly be seen. When the plasma is underdense, bright rings of emission are observed, especially around the center stack magnets near the ECH zone (and perhaps also near the upper hybrid resonance regions), indicating resonant electron heating and trapping. This phenomenon is very likely a transition from an overdense plasma produced by surface waves to an underdense, electron cyclotron resonance heated plasma, as reported in similar microwave powered multicusp plasmas [47]. Light emissions characteristics, as measured with a spectrometer, along with plasma density (as measured by an internal triple Langmuir probe) and temperature (as measured by both Optical Emission Spectroscopy and the triple probe), are shown in Fig. 2.8.

It would be interesting to measure the microwave field in the plasma with, for example, a simple monopole antenna. The probe could consist of a coaxial cable housed inside of a closed ceramic tube, with perhaps a centimeter of stripped central conductor at the end. The signal could be down converted and measured with a spectrum analyzer or oscilloscope, or perhaps even measured with an inexpensive microwave diode detector. These measurements have not yet been performed on PCX, but might be useful in understanding the transition from overdense to underdense states. As shown in Fig. 2.8c, in the underdense state, both diagnostics agree that T_e increases at the magnetized edge. In the overdense state, it is not clear if T_e increases or decreases at the edge. Perhaps the probe measurement is somehow compromised by an edge-localized microwave field in the overdense state.

2.5 Electrostatic Stirring Assembly

2.5.1 Hot Cathode Construction

Each outer cathode consists of two filaments, where each filament is formed from 0.015" thoriated tungsten wire, wound into 12 loops by wrapping around 1/4"-20 threaded rod. This wire

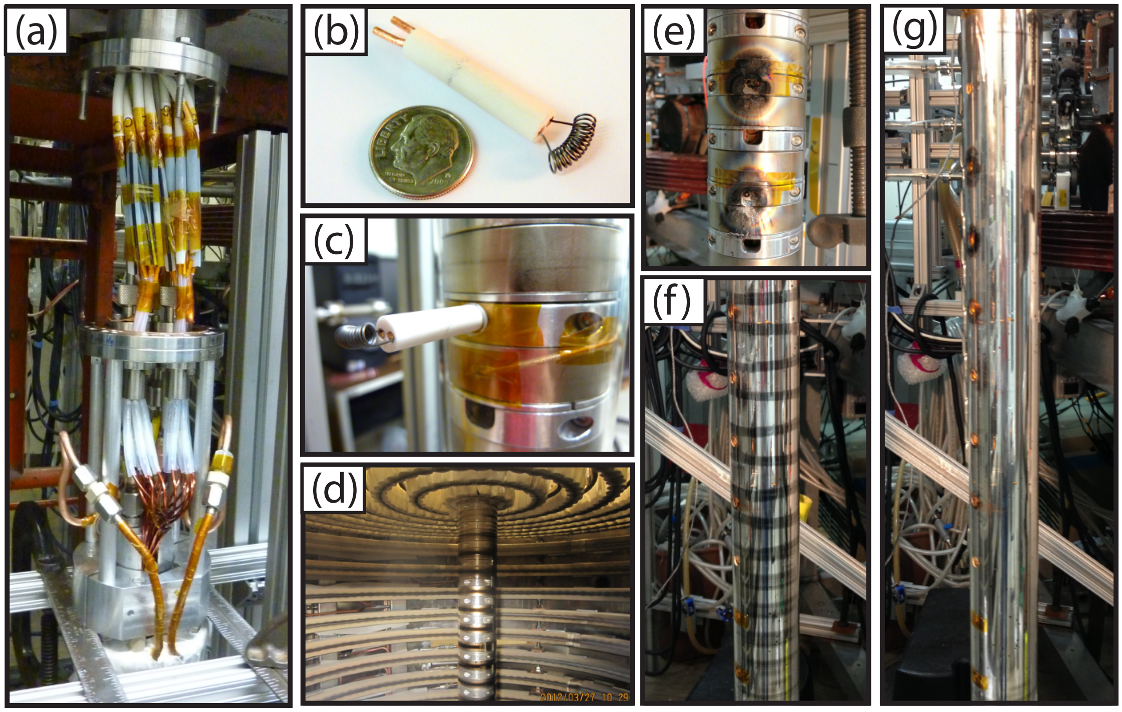

Figure 2.9: Details of center stack construction and maintenance. a) Water cooling, electrical feedthroughs, and wiring for anodes and individually heated/biased cathodes. b) Center stack cathode. c) Installed cathode and thermocouple measuring magnet surface temperature. d) Installed center stack assembly. e) (Repairable) damage from overheated cathodes. f) Rings of undesirable metallic deposits form on quartz tube. g) Quartz tube was successfully cleaned.

diameter was (empirically) found to be ideal, since thinner wires fail too quickly, while thicker wires require too much heating current to be practical. Each filament leg is mounted by press-fit connections to a copper conductor and additional tungsten wires inside of an alumina tube. Each outer cathode has a total surface area of approximately $5.7\ \mathrm{cm}^2$.

Inner cathodes are constructed in a similar manner using 0.015" thoriated tungsten wire, with 13 loops formed using 1/8" threaded rod (see Fig. 2.9 for photos). The smaller filament dimensions are needed to fit between the smaller, stronger magnets at the inner boundary. Filaments are housed in double bore alumina tube with copper leads, and each cathode plugs in to a receptacle mounted on an aluminum clamp. Wiring was gauged to ensure that the filaments are the most resistive part of the circuit. Six out of the possible ten cathodes are installed; additional cathodes would require modification to both the center post and electrical vacuum feedthroughs. Each inner cathode has a total surface area of approximately $1.6\ \mathrm{cm}^2$.

Finally, the anodes are made of cold molybdenum rods. The outer anodes are constructed from 1"-long cylinders of 1/2"-diameter molybdenum, mounted on stainless steel conductors surrounded by alumina tubes. The inner anodes are ≈ 0.75" -long cylinders of 1/4"-diameter molybdenum, mounted on molybdenum threaded rod insulated by quartz tubes. All inner anodes are mounted to a copper bus bar and biased together.

Filaments are ohmically heated to temperatures around 1700°C using variable-voltage AC power supplies and isolation transformers. Temperatures are measured by an uncalibrated Mikron infrared pyrometer, model M90-V. The inner and outer electrode assemblies are biased with separate DC power supplies. The cathodes are negatively biased (maximum 600 V) with respect to the cold anodes, and the entire electrode assembly is floating relative to ground (the chamber wall). Current and voltage transducers are used to measure each electrode, and emission currents can be adjusted by varying filament temperatures or bias voltages.

The filament lifetime is presumably limited by evaporation of the filament material, but likely dominated by sputtering through ion bombardment from exposure to plasma. The sputtering rate can be estimated by

$$\text{Sputtering Rate} = \frac{MSj}{\rho N_A e} \tag{2.3}$$

where M [g/mol] is the molar weight , S [atom/ion] is the sputtering yield , j [A/cm^2] is the ion current density , ρ [g/cm^3] is the material density , $N_A = 6.02 \times 10^{23}$ mol^{-1}, and $e = 1.6 \times 10^{-19}$ C is the charge of an electron. For tungsten, $M = 184$ g/mol, $\rho = 19.26$ g/cm^3, and $S = 0.3$ for Argon ions at 600 V [48]. Using a current density for a filament operated at j =0.2 A/cm^2, then Eq. 2.3 would estimate that the sputtering rate is $\approx 6 \times 10^{-6}$ cm/sec. Assuming a monolayer is twice the atomic radius (radius=1.37 $\mathring{A}$) and that there are 10^{15} atoms/cm^2 per monolayer, this sputtering rate is equivalent to about 2×10^{17} atoms/cm^2/sec. In comparison, the rate of vaporization of thoriated tungsten at 1700°C is on the order of 10^{11} atoms/cm^2/sec [49]. Even if the cathodes are biased and exposed to plasma only 10% of the total operating time, it seems that sputtering is the dominant mechanism for filament wear.

Filament lifetimes have typically been less that 50 hours on PCX. Replacement was needed after an accidental vacuum break exposed the hot filaments to air, which caused thick oxide layers to form and reduced emission. In general, filaments most often fail during high density plasma discharges. During the overdense state of the plasma discharge, large spikes in currents between biased cathodes and adjacent anodes are often observed. It is not clear if this is due to shorting across the face of the magnets due to contamination by deposition of conducting material, or if it is a property of the cathodes themselves. One possibility is that higher plasma density could cause increased and possibly non-uniform heating through ion bombardment, leading to localized hot spots and sudden bursts of emission current. Similar effects might occur because the coil shaped filaments could pick-up strong E-fields from microwaves in the edge region. Other causes could be non-uniform wire diameter, creating areas of increased resistance, or by complicated plasma-surface interactions which could influence the continual diffusion of thorium atoms along grain boundaries to the surface, which is ultimately responsible for the lowered work function and increased emission properties of the tungsten wire.

2.5.2 Cathode Current Limits

The electrode current—and presumably the plasma rotation—may be limited by several factors. First, the cathode may not be hot enough to emit sufficient electrons. In this temperature limited

Thermionic Emitter	Work Function (eV)	Richardson Constant (A cm^{-2} K^{-2})	Emission Current Density (A cm^{-2})	Rate of Vaporization (g cm^{-2} sec^{-1})
W	4.5	60	7.5×10^{-4}	8×10^{-13}
Th-W	2.6	3	2.7	7×10^{-11}
LaB$_6$	2.7	40	20	1×10^{-7}

Table 2.1: Comparison of various thermionic cathode materials, with emission current density (based on Eq. 2.4) and rate of vaporization at 1700°C. [50, 51, 49]

regime, the emitted current is independent of applied voltage, and the saturated current density depends only on the temperature of the heated metal. In this regime, the thermionic cathodes are described by the Richardson-Dushman equation,

$$J = AT^2 e^{-W/T} \tag{2.4}$$

where A is the Richardson constant, W is the work function, and T is the cathode temperature. Reasonably high thermionic current densities can be obtained with thoriated tungsten (see Table 2.1.) At 1700°C, the maximum emission current for cathodes in PCX is expected to be around 4 A from inner cathodes and 15 A from outer cathodes.

Temperature limited emission occurs at sufficiently high negative bias voltage. At lower voltages, cathode emission current is limited by space-charge effects. In the presence of a plasma, a double sheath can form around the hot filament, in which excess electrons form a potential dip near the edge of the sheath and acts to limit any further electron emission. The space-charge limited current density from hot cathodes is fairly well studied and is generally found to be consistent with the Child-Langmuir law [52], given in one dimension as,

$$J = \frac{4\epsilon_0}{9D^2}\sqrt{\frac{2e}{m_e}}V^{3/2} \tag{2.5}$$

Here, V is the potential between the plasma potential and the minimum found outside of the cathode, and D is the sheath thickness. The sheath thickness can depend on both the applied voltage and the Debye length, $\lambda_{De} = 743\sqrt{\frac{T_e+T_i}{n_e}}$ cm. Hence, the space charge limited current density can vary with plasma parameters. In the context of using hot cathodes to drive current and induce rotation, it is therefore desirable to operate in the temperature limited regime to achieve constant emission current and eliminate variation in current due to changing plasma parameters.

2.6 Diagnostics

2.6.1 Mach Probe

Flow is measured using a Mach probe, in which two oppositely-facing conductors are separated by an insulator and biased (-70 V) to draw ion saturation current. In a flowing plasma, the upstream side of the probe should collect more ion current than the downstream side. Although the validity of the original theoretical model has been questioned[53, 54], various fluid, particle, and kinetic models agree [55] that the drift velocity can be deduced from the ratio of upstream to downstream current in the form,

$$\frac{j_{isat}^{+}}{j_{isat}^{-}} = \exp(K v_{drift}/C_s), \tag{2.6}$$

where C_s is the ion sound speed and K is a calibration factor which depends on the particular assumptions of the model. It seems that the most agreed upon value for K for a drifting, unmagnetized plasma is $K = 1.3$ for $T_i < 3T_e$ [56], and therefore will be the value used for the analysis in this thesis. Ideally, the Mach probe should be calibrated through comparison to a separate ion velocity measurement, for example Laser Induced Fluorescence (which turns out to be non-trivial, as discussed in Section 2.6.6).

It has been shown both numerically and experimentally that under certain conditions, Mach probes in unmagnetized plasmas can be unreliable and exhibit an unexpected reversal of ion flux [57, 58]. This non-intuitive behavior can occur in situations where drift velocities are slow compared to sound speed, Debye length is comparable to probe size, probe bias much larger than T_e/e, and ion temperature is small compared to electron temperature. However, experiments with plasmas similar to PCX have shown that unmagnetized Mach probes can be reliable when

$\lambda_{De} \leq .05R_p$, where R_p is the probe radius [58]. The PCX Mach probes have therefore been designed to have a large collecting area, so that $\lambda_{De} \leq .03R_p$, which gives confidence in the accuracy of Mach probe measurements.

In PCX, radially scanned Mach probes are constructed from two oppositely-facing 6.35 mm diameter molybdenum disks, separated by boron nitride insulator and mounted on a 6.35 mm o.d. alumina shaft. A vertically scanned array of four pairs of radially spaced Mach probes has also been installed. The molybdenum conductors are spot welded to the center conductor of kapton insulated, coaxial vacuum wire, with the outer conductor grounded for shielding. The ion saturation current to each probe tip is measured using a 50 Ω resistor between the negative bias and probe tip. The voltage drop across the shunt resistor is measured with an AD215BY isolation amplifier circuit. This amplifier circuit, designed by Mikhail Reifman, has a maximum gain of 200, a bandwidth of 120 kHz, and is widely used in the UW Plasma Physics Group. For reference, a circuit diagram of the isolation amplifier can be found in Appendix B. Measurements from each Mach probe tip are digitized simultaneously at 200 kSamples/sec with the DTACQ system. The position of the probe is changed between plasma pulses to measure profiles, and the probe is frequently rotated 180° to repeat the flow measurement and verify that each tip area and circuitry is identical. Probes must be cleaned frequently because the boron nitride insulator becomes coated with a conducting material (likely tungsten), which can effectively increase the probe collection area and eventually short the two probes.

2.6.2 Single Tip Swept Langmuir Probe

The Langmuir probe is perhaps the oldest and most widely used low temperature plasma diagnostic. Simple in design, the probe consists of a bare wire or metal disk, which is biased with respect to a reference potential (i.e. the grounded chamber wall) to collect electron and ion currents. Langmuir probes can be used over a wide range of parameters to measure electron temperature, density, plasma potential, and can sometimes even reveal the presence of electron or ion beams.

In PCX, the single tip swept probe is a 6.35 mm diameter molybdenum disk (usually one side of a Mach probe). The probe is biased with a 100 Hz triangle wave swept from -90 V to 20 V with respect to ground, and the voltage and current signals are recorded by the DTACQ system throughout the plasma pulse. The analysis routine begins by finding the peaks of the applied bias. If the probe is dirty, hysteresis in the IV characteristics is often observed, so the routine can separately analyze the sweeps from negative to positive voltage, or from positive to negative voltage. Of course, it is preferable to use a clean probe so that hysteresis is not an issue. Individual sweeps can be noisy and difficult to fit, so data is smoothed by combining a number of sweeps over a time window (usually 200 ms). The data is then sorted and smoothed using a simple moving average filtering method ('smooth' function in Matlab). After subtracting the offset current of the circuit when the plasma is off, the resulting I-V curve is analyzed using a somewhat standard method [59]:

1. A straight line is fit to the ion saturation region and extended to the electron saturation region, and the electron current is found from $I_e = I - I_{sat}$.
2. The bulk electron temperature, T_e, is calculated as the inverse of the slope of $\ln(I_e)$ in a subset of the region $V_f < V < V_p$.
3. The plasma density is found by assuming the ion saturation current is given by the Bohm current, $I_{sat} = 0.6en_0\frac{T_e}{M_i}$, or

$$n_0[\mathrm{cm}^{-3}] = 1.068 \times 10^{13}\frac{I_{sat}[\mathrm{A}]}{A[\mathrm{cm}^2]}\sqrt{\frac{\mu}{T_e[\mathrm{eV}]}} \tag{2.7}$$

This Langmuir analysis assumes unmagnetized, nondrifting, Maxwellian electrons. In reality, primary electrons (due to biased filaments and ECH resonance heating) are likely present, leading to a population of higher energy electrons in the tail of the distribution function. A monoenergetic population of primary electrons would be evident as an additional knee at large negative voltage. While this high energy electron feature has not yet been found in the Langmuir data produced by the particular hardware setup in this experiment, a correct analysis would involve subtracting the straight-line fit of the current due to energetic electrons before calculating the bulk electron temperature. Collection of high energy electrons can also lead to secondary electrons produced at the probe surface, resulting in an apparent increase in ion current and an underestimate of bulk electron temperature.

Uncertainty in the density measurement occurs when the probe is biased at large values, where sheath expansion effectively increases collection area, and ion (or electron) saturation current becomes a function of applied bias. Secondly, probes scanned in the cusp region of the plasma encounter a range of magnetic field values (up to ~ 1 kG) that can be either parallel or perpendicular to the collecting surface depending on probe orientation, and probe characteristics can depend on how particles populate the flux tubes intersecting the probe. Finally, in a flowing plasma, the orientation of the probe with respect to the flow can affect the amount of ion saturation current collected, making it difficult to interpret the meaning of density measurement. Nonetheless, the density measurements seem to agree within 20% when cross-checked with the sharp transition that occurs at the known 2.45 GHz microwave cutoff density of 7.4×10^{10} cm^{-3}.

2.6.3 Triple Tip Langmuir Probe

The single tip swept Langmuir probe analysis routine is complicated, and the data must be processed post-run to ensure accuracy of fits. An alternative is to use a triple Langmuir probe, which can instantaneously measure electron temperature, density, and plasma floating potential without the use of a voltage sweep and detailed data analysis. The triple probe essentially samples three points of the exponential region in the characteristic IV curve of a swept probe. A bias potential is applied between Tip 1 (positive) and Tip 2 (negative), while Tip 3 is floating. The negatively biased tip draws mainly ion saturation current, while the positive tip draws electron saturation current. Assuming a Maxwellian electron energy distribution, the electron temperature can be found from the relation [60]

$$\frac{1}{2} = \frac{1 - e^{-e(V_1 - V_3)/kT_e}}{1 - e^{-e(V_1 - V_2)/kTe}} \tag{2.8}$$

When the applied bias voltage is sufficiently large, so that $eV_b > 3kT_e$, the electron temperature is simply $T_e \cong e(V_1 - V_3)/\ln 2$. Thus, the electron temperature is found by measuring the floating potential of Tip 3 and the positive potential of Tip 1, and the ion saturation current drawn by Tip 2 is used to find the plasma density.

This analysis assumes that the ion saturation current is independent of the applied voltage to the probe, and that the plasma is not flowing. As mentioned in Section 2.6.2, ion saturation current is not necessarily constant with voltage and can be a complicated by sheath expansion, high energy electrons, or plasma flow. This can lead to an overestimate in the electron temperature calculation and an overestimate in the density. In previous studies, sheath expansion alone can cause up to 25 $\%$ error for $T_e < 10$ eV, and the percentage error increases with increasing T_e [60], although corrections can be made to T_e and n_e based on assumptions about the behavior of ion saturation current, applied probe bias, and an arbitrary probe geometry factor (see Eqs. 27 & 32 in [60]).

The PCX triple probe consists of three identical tungsten wires, 1 mm diameter and approximately 7.5 mm long. The tips are separated by boron nitride insulator and spaced 2 mm apart in an equilateral triangle. Tip spacing was chosen to be much greater than the Debye length to avoid interference between tips. The probe geometry is designed to minimize probe shadowing by the poloidal field lines at the magnetized edge or by the induced azimuthal flow velocity. The triple probe is located on the same plane as a radially scanned Mach probe, so the triple probe is usually located at a fixed radius of $r = 0.35$ m to avoid interfering with the Mach probe. The triple probe can, however, be manually scanned to a minimum radius of $r = 0.26$ m. Raw data taken with the DTACQ system is stored in MDSplus, and an automated data analysis routine displays T_e, n_e, and V_f for control-room guidance during operation.

2.6.4 Rake Probe

The radial electric field is measured with a rake probe consisting of a single Mach probe, as described in Section 2.6.1, along with multiple radially-spaced tips to measure floating potential. A total of five floating potential tips are equally spaced by 2 cm along the alumina probe shaft, and each tungsten wire tip is 1 mm diameter and several mm long. The floating potential of each probe tip is measured with a voltage divider and an AD215BY isolation amplier circuit, digitized by the

DTACQ system, and stored in MDSplus. Each floating potential probe circuit has been calibrated for offsets and gain by applying known voltages to the probe tips using a DC power supply.

One of the difficulties with floating potential measurements in PCX is that large fluctuations of 60 Hz (and harmonics) are often present when the plasma is on, presumably due to the ECH microwave source (the magnetron employs a filament heated with 60 Hz). The biased filaments in the experiment may also contribute, which are also heated at 60 Hz. Usually, $|Vf| < 10$ V, with ± 2 V fluctuations. In addition, 'arcs' are often encountered in plasmas with biased cathodes, which show up as large spikes in the floating potential measurements. In order to extract the meaningful potential data (which is DC in character), a Savitzky-Golay smoothing routine (based on sgolayfilt in Matlab) has been applied to reduce the magnitude of the time-varying fluctuations and remove large voltage spikes from the data.

2.6.5 Optical Emission Spectroscopy

Optical Emission Spectroscopy is non-invasive diagnostic which uses plasma light emission to determine the electron temperature and (possibly) density. This method has previously been developed by collaborators on an inductively coupled argon plasma used in processing with temperatures, in practice, in the $1 < T_e < 6$ eV range [61], but this is the first application to plasma with both higher electron temperature (up to 15 eV) and ionization fraction (30%).

One of the major advantages of this technique is that it requires a spectrometer with only modest resolution ($\sim$ 1 nm). This allows the use of a relatively inexpensive Ocean Optics USB2000+ spectrometer. The measured plasma emission spectra, along with neutral pressure measurement, can be used to first determine the number density of ArI atoms in the metastable and resonance levels. The metastable atoms significantly contribute to emissions lines, and the population of a radiating level and its emission intensity are governed by (a) electron excitation from the ground level by high-energy electrons (>13 eV), and (b) electron excitation from the metastable level by electrons with low and medium energy (>1.4 eV). Since the optical emission cross sections are energy dependent, the effective electron temperature can be found through a χ^2 minimization routine comparing an emission model (which predicts line ratios using optical emissions cross

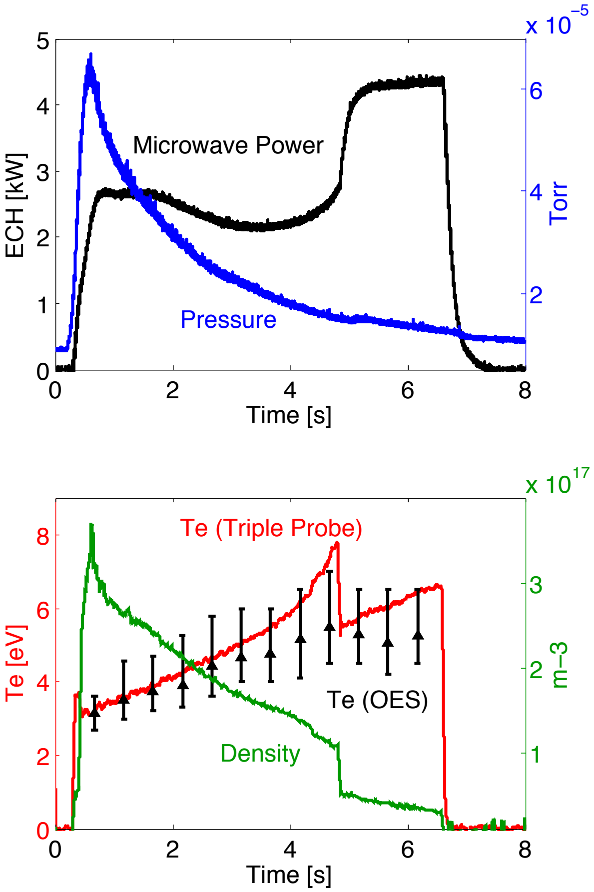

Figure 2.10: Top) OES data was taken during a puffed argon discharge (Shot #622), where a transition from over- to under-dense occurred at around t=5 s. Bottom) Triple probe density and electron temperature measurements vs. time, along with the line-integrated temperature obtained with Optical Emission Spectroscopy.

sections and an assumed electron energy density function) to the measured line ratios of a select group of lines emanating from different upper levels.

So far, the OES electron temperature measurements have been in impressive agreement with probe measurements, as shown in Fig. 2.10. The Optical Emission Spectroscopy project has primarily been headed by undergraduate Blair Seidlitz, who has converted analysis code written by John Boffard in LabVIEW to Matlab. One goal is to fully automate the data analysis for use during routine operation. The diagnostic will be further developed to measure spatially resolved emission along chords using a radially-scanned optics table, making it possible to fully characterize radial temperature and density profiles.

2.6.6 Development of Laser Induced Fluorescence

Laser induced fluorescence (LIF) is a technique that can be used to measure ion temperature and ion flow velocity, quantities which are especially important in PCX for confirming Braginskii's formulas for viscosity and for verification of the internal Mach probe flow profile measurements. For this reason, an LIF diagnostic has been developed on PCX through collaboration with Prof. Fred Skiff from the University of Iowa. In this system, a Toptica DLpro tunable diode laser centered at $\lambda_0 =$1047.00475 nm is used to optically pump a metastable argon ion (in the $3d^2F_{7/2}$ state) up to the $4p^2D_{5/2}$ state. The excited state subsequently decays to the $4s^2P_{3/2}$ level, emitting light at 488.1226 nm which is collected with a series of lenses, a filter, and a photomultiplier tube (PMT). To measure profiles, an optics table can be scanned to observe fluorescence at different radii, as shown in Fig. 2.11. To our knowledge, this is the first time LIF has been performed at this laser wavelength.

LIF schemes typically target ions which are in an excited, metastable state, which is often long-lived since selection rules forbid electric dipole radiation. If the metastable ion is moving towards the laser, the incident laser light in the particle frame will be Doppler shifted to higher frequency. Thus, the laser frequency must be lowered (wavelength increased) in order to excite the ion. In this way the ion velocity distribution, and thus the ion temperature, can be found from Doppler broadening of the measured intensity of the fluorescence radiation as a function of laser

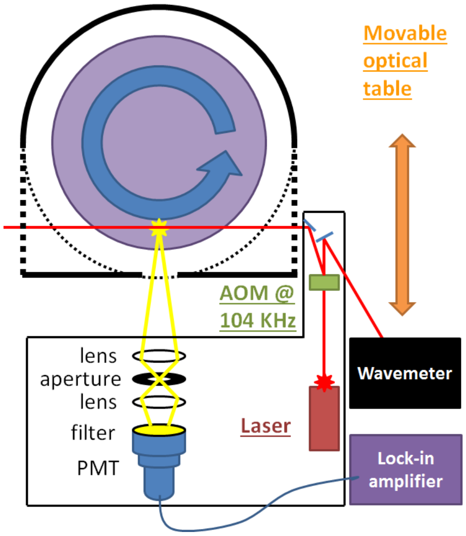

Figure 2.11: Laser Induced Fluorescence setup to measure localized T_i and plasma flow.

wavelength. In addition, the bulk ion flow velocity can be obtained from the Doppler shift of the central peak of the fluorescence spectrum. The equations used in these calculations are;

$$V\ [\text{ km/s }] = 3 \times 10^5 \left(\frac{\lambda}{\Delta\lambda} - 1 \right) \tag{2.9}$$

and

$$T_i\ [\text{ eV }] = \mu \left(\frac{2\sigma}{7.7 \times 10^{-5}\lambda} \right)^2 \tag{2.10}$$

where $\Delta\lambda = \lambda - \lambda_0$ is the shift in the peak, σ is the standard deviation of a fitted Gaussian, and μ is the atomic mass.

The initial setup used an optical chopper blade to modulate the laser beam at 809 Hz, and the photomultiplier and chopper reference signals were monitored using a Stanford Research Systems SR530 lock-in amplifier. The signal-to-noise ratio was greatly improved by replacing the chopper blade with an Isomet acousto-optic modulator (model M1135-T80L-3) and RF driver (model (522C-7). The driver was modulated by a 104.7 kHz square wave from a function generator. Prior to each plasma pulse, the wavelength of the primary, undeflected laser passing through the modulator is measured by a Burleigh WA-1500 wavemeter. When modulated RF power is applied, the secondary, diffracted beam passes through the PCX box port window to the plasma for the LIF measurement. The PMT voltage was adjusted to prevent saturation of the lock-in amplifier input.

Measurements in an argon plasma with flow driven by the outer boundary cathodes are shown in Fig. 2.12. The Mach probe measurements clearly indicate flow, and the probe measurements agreed when the probe was rotated 180°. The ion temperature predicted by the model described in Section 4.1 (which was used to fit the Mach probe measurements in Fig. 2.12b) is $T_i = 0.11$ eV. Curiously, the LIF measurements do not agree with Mach probe measurements, with the lack of Doppler-shifted peaks indicating zero flow across the radius of the plasma. The LIF measurements in Fig. 2.12a also indicated that $T_i \sim 0.035$ eV.

Since LIF is seemingly used successfully in other experiments, an effort was made to investigate the cause of discrepancy in PCX. LIF at 1047 nm has not been well established in the literature, so the first step was to switch to a more traditional scheme, using a laser centered at λ_0 =668.6138 nm to excite the $3d^4F_{7/2}$ metastable argon ion to the $4p^4D_{5/2}$ state, which promptly decays to $4s^4P_{3/2}$ and emits light at 442.7244 nm. The results of the LIF radial flow profiles for both lasers are compared to the Mach probe measurements in Fig. 2.12b. The 668 nm laser also indicated flat velocity profile. A suspected error in the wavemeter calibration settings may have led to artificial net offset of $\sim$ 600 m/s, as measurements were repeated on a different day and indicated zero flow.

As is made clear in this thesis, considerable evidence supports the Mach probe measurements, which suggests that the metastable ion state being probed by LIF is not representative of the bulk, flowing ion species. This problem is actively being investigated, largely in part by current post-doctoral scholar, Dr. Chris Cooper, and progress to-date is presented here. To gain a better understanding of factors which determine the metastable state density, LIF was performed in discharges at various neutral pressures, in both overdense and underdense plasmas (see Fig. 2.13). The laser wavelength was fixed at the central peak wavelength λ_0 using either the 1047 nm laser or the 668 nm laser, and the magnitude of the LIF signal was recorded at radius ($r = 25$ cm). The plasma parameters T_e and n_e were measured by the triple probe at $r = 37$ cm.

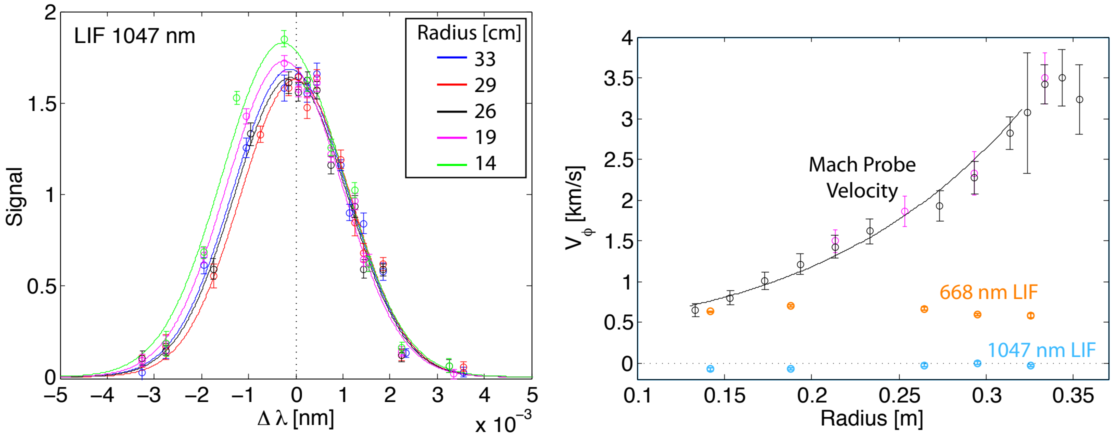

(a) (b)

Figure 2.12: a) LIF measurements using the 1047 nm laser at different radial positions, which unexpectedly showed no Doppler shift. b) Expected velocity (as measured by the Mach probe) vs. velocity measured by LIF at 668 nm (red) and 1047 nm (blue). A suspected error in the wavemeter calibration settings may have led to artificial net offset in the 668 nm flow measurement. Neither measurement agrees with Mach probe data.

In order to initiate and maintain the discharge, it was necessary to heat and bias the four outer cathodes -50 V ($\sim$ 0.4 A each). Even with biasing at -50 V, it was generally not possible to reach underdense plasmas ($< 7.4 \times 10^{10}$ cm^{-3}). Thus it was only possible to use this low -50 V bias overdense plasmas. To explore the effects of the high energy electrons that originate from the stirring assembly cathodes, all four outer cathodes were biased at -400 V ($\sim$ 0.9 A each). However, it was not possible to operate with -400 V biased cathodes when the plasma was overdense ($> 7.4 \times 10^{10}$ cm^{-3}) due to cathode arcing.

The experiments in Fig. 2.13 reveal important trends in the metastable density signal. First, there is good agreement between the two lasers. Second, the regime of most interest is the one in which the plasma is underdense, and the cathodes are biased -400 V, since these are the conditions under which the Mach probe indicates bulk plasma flow (as shown in Fig. 2.12b). In this regime, the metastable signal scales with argon neutral density ($S \sim n_n^1$), as indicated by the blue markers in Figs. 2.13a-b. This suggests that the metastable states are formed by electron impact excitation, where the production rate for a volume, V, would be expected to follow

$$S_{iz,ex} =< \sigma_{iz,ex} \mathrm{v}_b > n_b n_n \mathrm{V} \tag{2.11}$$

Here, the bracketed quantity represents a rate constant, which should be found by integrating the velocity-dependent cross section over the velocity distribution function of the incident electron beam. Note that the cross section $\sigma_{iz,ex}$ is only appreciable for electron beam energies $>$ 50 eV. On the other hand, if the metastable ions were populated by collisional excitation, then $ST_e^{1/2} \sim n_e^2$;

$$S_{col,ex} =< \sigma_{ex} \mathrm{v}_e > n_e n_i \mathrm{V} \tag{2.12}$$

which does not seem to be the case, as shown in Figs. 2.13c-d.

The important point is that in the PCX operating regime for spinning plasma, the metastable argon ions measured by LIF are primarily populated through electron-impact excitation of *stationary* neutrals. The newly formed, stationary metastable ions can be subsequently lost to nearby electronic states through collisions with either electrons or ions, a process referred to as quenching. In PCX, ions in the bulk unmagnetized region acquire momentum through collisional viscosity, which occurs on ion-ion collision timescales of around 10 μsec. Furthermore, according to [62], the lifetimes for metastable state ions produced by electron impact of neutral atoms is $>$10 μsec (for both the $3d^2F_{7/2}$ and $3d^4F_{7/2}$ states.) It may be that the metastable ions are not able to acquire momentum before exiting the state due to collisional quenching or even lifetime decay. Therefore, it would be impossible to measure flowing ions with LIF in PCX.

The measurements made in PCX highlight the fact that LIF is a non-trivial diagnostic which, despite excellent precision, does not appear to be well-suited for accurate ion flow measurements in PCX. The measurements presented in this section were made in the bulk, unmagnetized region of the plasma, but data was also taken in the strongly magnetized, edge region in an effort to understand ion diamagnetic, $\mathbf{E} \times \mathbf{B}$, ∇B, and curvature drifts. The LIF measurements did indicate flow, but in the direction opposite of the flow measured by the Mach probe. These results are still work in progress, and a summary is presented in Appendix C.

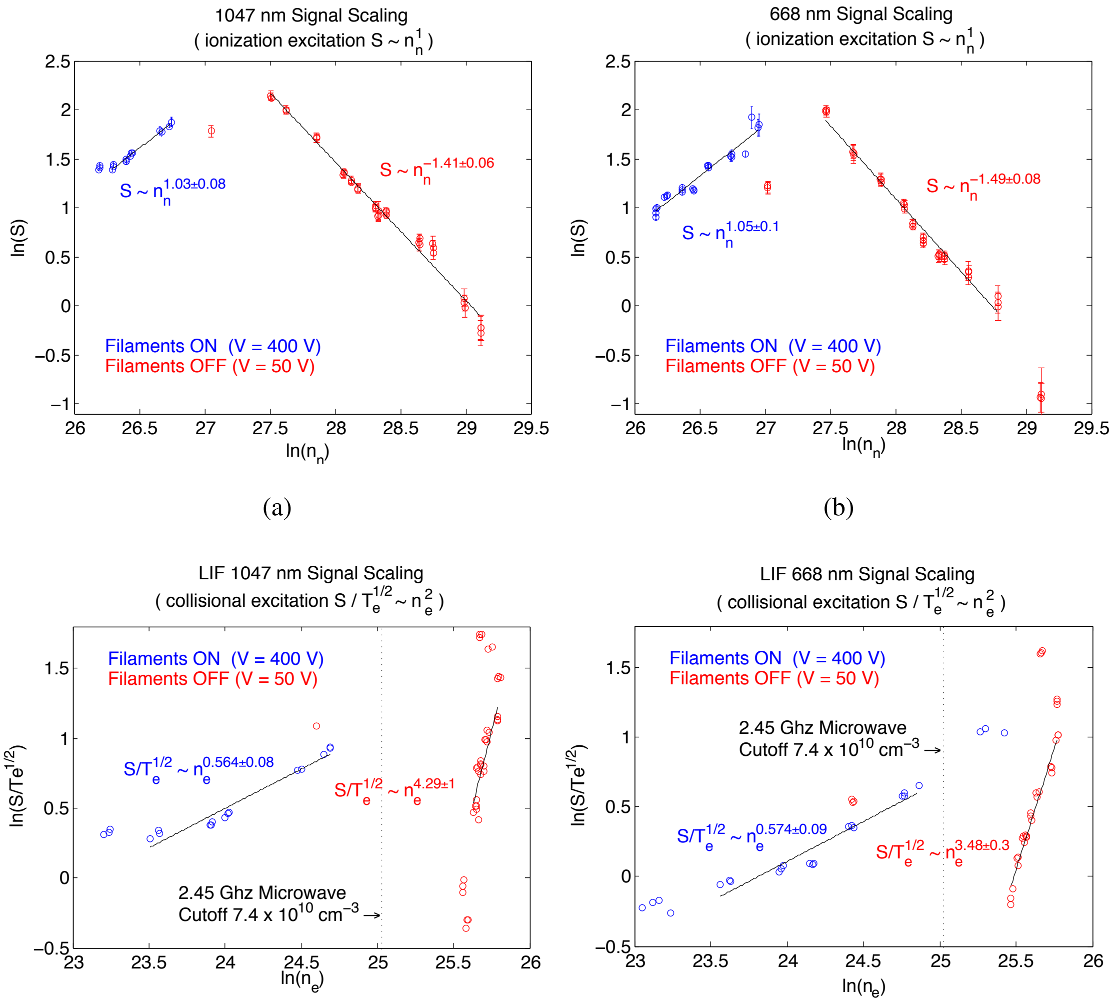

(a) (b)

(c) (d)

Figure 2.13: Comparison of LIF signal, S, from 1047 nm and 668 nm vs. neutral density (a-b) or $S/\sqrt{T_e}$ vs. density (c-d), where T_e and n_e were measured by the fixed triple probe.

Chapter 3

Demonstration of Flow Drive

In the presence of perpendicular and static electric and magnetic fields, both ions and electrons undergo one of the most basic forms of drift motion in a plasma. As the particle gyrates around the magnetic field, it is accelerated in the direction of the electric field, leading to a non-circular orbit and net drift motion in the direction perpendicular to both E and B. The resulting guiding center drift velocity, $\mathbf{v} = \mathbf{E} \times \mathbf{B}/B^2$, is independent of charge and mass.

In the Plasma Couette Experiment, electrostatic potentials, introduced through biased electrodes placed in the magnetized edge region, are used to induce $\mathbf{E} \times \mathbf{B}$ drift (see Fig. 3.1). Outside of sheath effects, the magnetic field lines are assumed to be equipotential, because the high mobility of electrons along field lines would prevent any parallel electric field from forming. Since the surface of the magnets is electrically insulated, the cross-field current is driven through the plasma. Plasma rotation is thus induced by $\mathbf{J} \times \mathbf{B}$ torque in the magnetized edge region, which can then couple into the bulk plasma by collisional viscosity.

This chapter presents the long series of experiments which revealed that in order for the flow drive technique to be effective, the current has to be large enough, the electrode position must be optimized, and the neutral pressure must be low enough for ion viscosity to dominate the momentum transport to the bulk plasma.

3.1 Initial Flow Drive Experiments With Cold Electrodes

The first attempts of rotation experiments used toroidally continuous rings of water-cooled, molybdenum-coated copper tubes (see Fig. 2.4 for photos). Rings were placed between the top

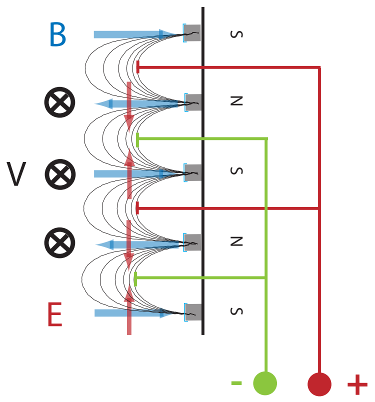

Figure 3.1: Concept for driving $\mathbf{E}\times\mathbf{B}$ flow with biased electrodes in the magnetized edge. Alternating positive and negative electrostatic bias is applied to electrodes between the cusp rings. The resulting torque causes the plasma to rotate about the symmetry axis and can be used for generating a variety of velocity fields.

and bottom endcap magnets, were biased with alternating polarity, and could be moved vertically to explore stronger or weaker regions of magnetic field strength. To create plasma, a steady flow of helium gas was introduced through a needle valve, and microwave power was applied. A Mach probe (pictured in Fig. 2.4c) was scanned radially approximately 2 cm above the bottom electrode rings, as shown in Fig. 3.2. Flow measurements were made shortly after the microwave system had been installed, and these early plasmas had fairly high neutral pressures ($P\sim$ 0.4 mTorr) which resulted in a low ionization fraction (0.1 %), with $n\sim 2\times10^{10}$ cm^{-3} and $T_e\sim$ 2.5 eV.

Even without optimized plasma parameters, two important discoveries were made. First, modulation in the azimuthal velocity profile near the magnets was observed, indicating magnetic drift effects due to the cusp field, which are likely a combination of the diamagnetic, ∇B, curvature, and $\mathbf{E}\times\mathbf{B}$ drifts:

$$\mathbf{V_{di}} = -\frac{\nabla P\times\mathbf{B}}{enB^2} \tag{3.1}$$

$$\mathbf{V_{\nabla B}}+\mathbf{V_{curv}} = \frac{1}{2}v_\perp r_L\frac{\mathbf{B}\times\nabla B}{B^2}+\frac{M_i v_{||}^2}{eB^2}\frac{\mathbf{R_c}\times\mathbf{B}}{R_c^2} \tag{3.2}$$

$$\mathbf{V_{ExB}} = \frac{\mathbf{E}\times\mathbf{B}}{B^2} \tag{3.3}$$

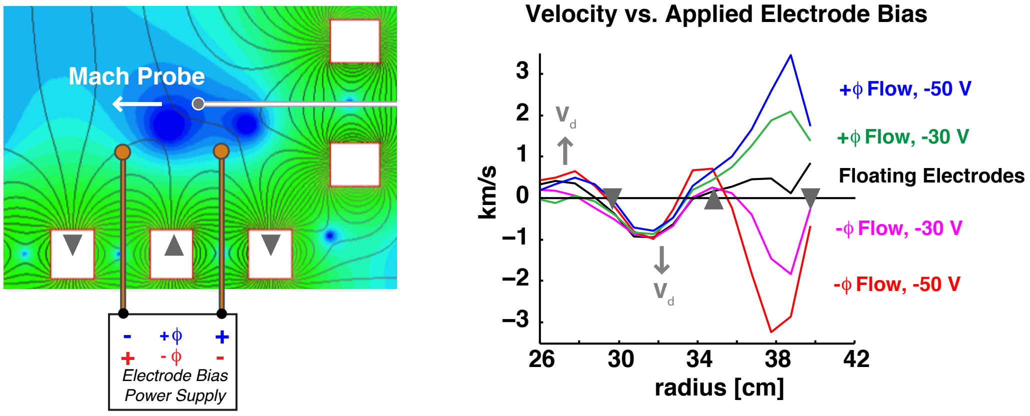

Figure 3.2: Demonstration of flow drive with cold electrodes. Mach probe measurements above biased, cold electrodes showed flow that scaled with applied bias and changed direction with reversed E-field. Velocity modulations due to the cusp field at the boundary were also observed.

Secondly, and most importantly, the measurements were the first observation of induced flow. Rotation velocities up to 3 km/s were observed in a narrow region at the corner of the experiment; the rotation scaled with applied bias, and the rotation direction could be reversed by changing the polarity of the applied electric field, as expected.

3.2 Maximizing Current Drive with Hot Cathodes

Significant improvement in the rotation drive was achieved with a second set of electrodes, which consists of thermionic (electron-emitting) tungsten filaments and cold anodes at a fixed toroidal location (see “Stirring Electrodes” in Fig. 2.3). Tungsten filaments have been widely used in incandescent light bulbs and as a source of energetic electrons for electron beam or plasma devices. Tungsten has a high melting point (3400°C), and filaments can be directly heated through ohmic dissipation, which simplifies cathode design. They are also relatively inexpensive and easily replaceable. In PCX, the thermionic emission from hot cathodes allows for 10 times more current than the cold electrodes, which were limited to ion saturation currents of several hundred milliamps. Furthermore, the hot cathodes have 10^5 smaller surface area, which significantly reduces the particle and energy fluxes escaping the plasma.

Although the hot cathode rotation drive assembly is toroidally localized, Mach probes successfully measure rotation on the opposite toroidal side of the chamber, suggesting that flow is axisymmetric within the accuracy of the measurements. Since the magnetic field assembly is axisymmetric, the single particle drifts (∇B and curvature) and the $\mathbf{E} \times \mathbf{B}$ flows themselves are in the toroidal direction and apparently serve to symmetrize the potential. Thus, even though the current is only injected at one toroidal position, the electric field at the edge becomes axisymmetric.

3.2.1 Empirical Studies of Optimal Electrode Placement

The plasma rotation depends strongly on the electrode placement. As electrodes are moved towards the unmagnetized core, the $\mathbf{J} \times \mathbf{B}$ force falls quickly to zero, and this change occurs over only a few centimeters. However, as the electrodes are pulled into the magnetized region, B increases, plasma density decreases, and the cross-field current J decreases. Therefore, the first consideration is to find the intermediate position which maximizes this $\mathbf{J} \times \mathbf{B}$ force.

A series of experiments were conducted with several gas species (argon or helium) in order to find the optimal outer electrode positions. First, the radial position of single cathode (biased 250 V) was varied in argon plasma while adjacent anodes were fixed. As the cathode was moved to smaller radii, the cathode current continually increased from 0.5 - 2 Amps. A Mach probe, located approximately 120° from the electrodes, was used to measure the velocity at $r = 0.33$ m. A peak in the velocity measurement occurred when the filament was located at $r = 0.376$ m. In a later experiment with helium plasma, two cathodes were biased 350 V and moved (together) radially, with anodes fixed at $r = 0.36$ m. A fixed Mach probe at $r = 0.33$ m measured peak velocity when cathodes were at $r = 0.37$ m. A summary of the data is shown if Fig. 3.3. Vertical error bars represent the standard deviation in fluctuations of measured velocity over time, and horizontal error bars represent the distance the filaments span in radius. At optimal locations, the hot cathodes are placed at a field strength of $Bz \approx 60 - 90$ Gauss. At these field strengths, ion gyroradii with

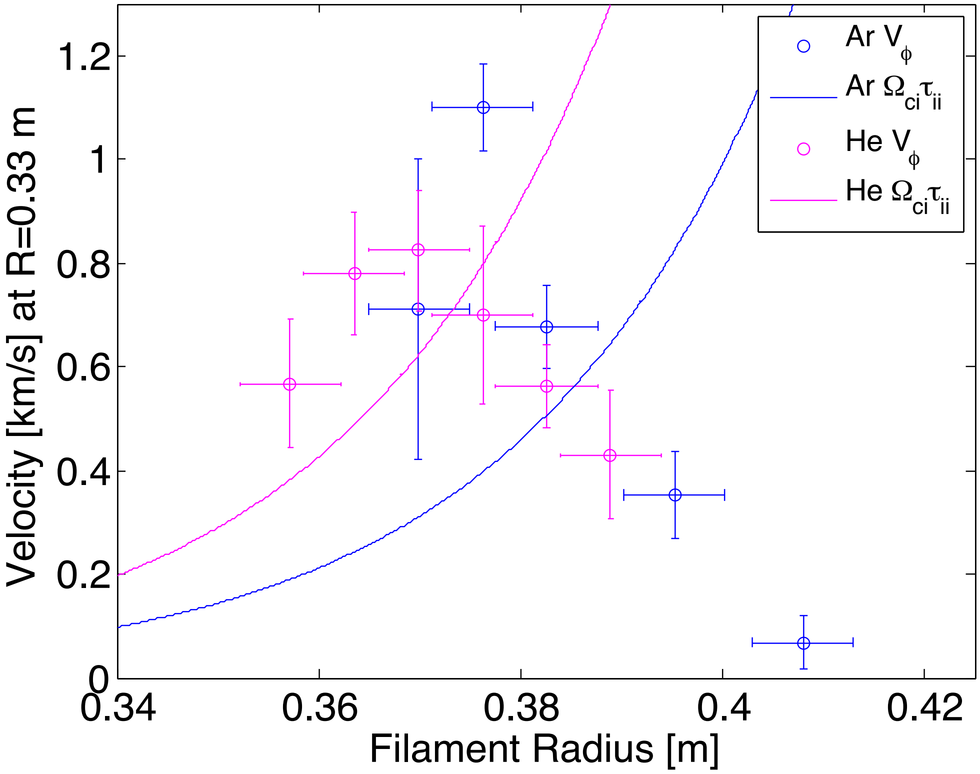

Figure 3.3: To find the best location for flow drive, the outer cathodes were moved radially and azimuthal velocity was measured at $r = 0.33$ m. The optimal location, which seems to work for both species, is $r = 0.376$ m. Overplotted is the magnetization, $\Omega_{ci}\tau_{ii}$ for each species.

$T_i = 0.1$ eV are 7-10 mm for helium and 22-34 mm for argon, while the electron gyroradius for a typical bulk electron at 5-10 eV ranges from 0.5-1 mm. For reference, a representation of magnetization, $\Omega_{ci}\tau_{ii}$, is overplotted in Fig. 3.3. Ions are magnetized when $\Omega_{ci}\tau_{ii} > 1$. The calculated magnetization is based on the simulated magnetic field Bz (Eq. 2.1) and assumes that the plasma density in the edge is 50$\%$ of the bulk and $T_i = 0.1$ eV. The blue line is for argon with $T_e = 10$ eV, $n = 1.3\times10^{10}$ cm^{-3}, and the magenta line is for helium with $T_e = 5$ eV, $n = 2.2\times10^{10}$ cm^{-3}. Parameters in the edge region are assumed constant, though in reality, gradients do exist in the magnetized edge region (as discussed in Appendix C).

These experiments led to the conclusion that the optimal location for outer cathodes is $r = 0.376$ m, with filament thickness spanning radially ± 0.005 m. Similarly, the anodes were varied radially while the cathodes were fixed, and the optimal location for anodes was found to be centered at $r = 0.357$ m, with the geometric dimensions of the anodes spanning ± 0.013 m in radius. It was found that the plasma potential remained closer to ground with floating anodes. If the anodes were grounded, the plasma potential becomes quite negative, making it difficult to use probes which are operated with biasing with respect to ground (e.g., Mach probes which are biased -70 V with respect to ground when $V_p = -60$ V are no longer collecting purely ion saturation current).

The position of the stirring electrodes on the center post assembly of magnets could not be varied as easily as the outer cathodes. A series of trial-and-error experiments involved removal of the center stack to test cathodes of various lengths. Based on the knowledge that the magnetic field strength at the optimal outer cathode position was around $Bz = 60 - 90$ Gauss, the inner cathodes were tested at three different locations: 60 Gauss, 40 Gauss, and 20 Gauss. The largest measured rotation rates were in helium when the cathodes were near 20 Gauss, and the cathodes that were closer to the magnets both drew less current and adversely heated the center post magnets. Rotation from the inner boundary in argon plasma was less successful and resulted in frequent destruction of inner boundary filaments due to arcing. Therefore, all six inner cathodes are centered at $r = 0.064$ m (spanning ± 0.003 m in radius) near $Bz = 20$ Gauss. The anode locations were not rigorously optimized, but exposed conductor lies between $r = 0.046 - 0.066$ m.

3.3 Optimizing Plasma Discharge Characteristics

Presumably, the dominant mechanism acting to slow the rotating ions is charge exchange collisions with neutrals. The obvious approach, then, is to create a plasma with low neutral pressure and high ionization fraction. It has been found that at low pressures, microwave power alone is not enough to initiate the discharge. Therefore, several techniques have been developed to to create consistent breakdown. One method is to introduce a steady flow of gas (10^{-4} Torr for helium and 10^{-5} Torr for argon) and then simultaneously switch-on the microwave power and biased cathodes. This creates a steady-state discharge with unchanging plasma density and temperature. A second method is to simultaneously apply microwaves with a strong puff of gas with a piezoelectric puff valve, creating a high neutral pressure at the beginning of each pulse. The neutral gas is then pumped out over the course of the discharge, and a wide range of plasma parameters can be studied in a single plasma pulse. In a puffed plasma pulse, the bias for the stirring electrodes can be applied at a later time to specifically study changes in the plasma parameters due to rotation. An excellent example which demonstrates much of the phenomenon observed in PCX is shown in Fig.3.4, in which plasma is created by a puff of gas, and stirring electrodes are biased at a later time in the shot. The plasma (measured by a triple probe) is initially overdense, and an increase in density is observed when the stirring electrodes are biased due to increased ionization. During the overdense phase, the cathodes tend to arc and the rotation is null (rotation is measured by a Mach probe near the peak rotation drive at $r = 0.36$ m). As the neutrals are pumped out, the density decreases, and an abrupt transition from overdense to underdense is observed. The plasma is heated throughout the discharge, not only by the microwaves, but also by the ohmic heating associated with the rotation electrodes. Consequently, as the density decreases, the electron temperature increases during the discharge. Rotation increases as the plasma density and neutral pressure fall and temperature increases. The plasma stops spinning when the bias is turned off, and the discharge is ended when the microwave power is turned off.

The plasma pulse length is limited to about 10 seconds in order to protect the permanent magnets from over-heating and becoming demagnetized. In addition, as the temperature of the magnets

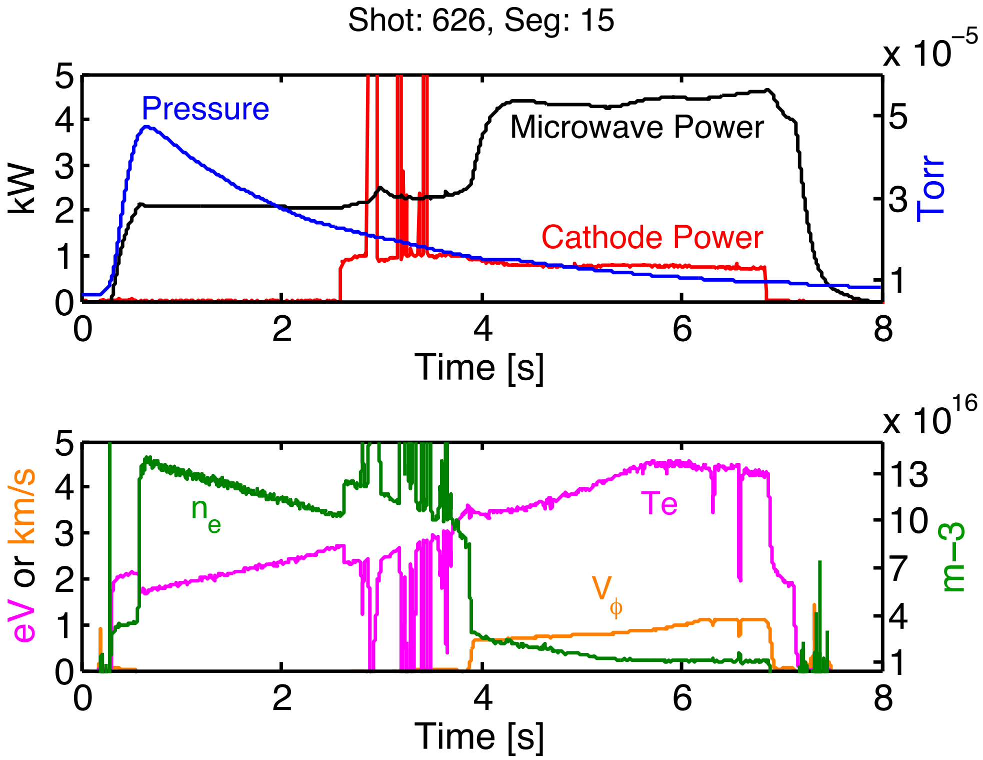

Figure 3.4: Plasma parameters vs. time showing a transition from overdense to underdense plasma around 4 sec. Maximum flow is reached at low density and low neutral pressure. Top) Plasma is created by simultaneously applying microwave and a large pressure puff. Bias (450 V) is later applied to induce rotation, drawing a total of 2 Amps of current from 4 outer cathodes. Bottom) Triple probe measurements of density and electron, and Mach probe flow measured in the edge region.

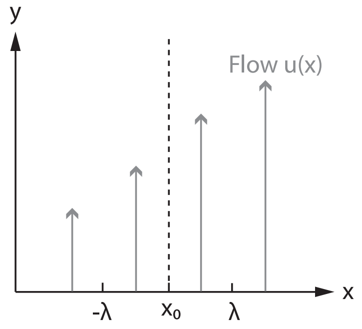

Figure 3.5: A simple example of viscosity in linear shear flow.

increases (up to 30-40°C), the residual gas analyzer indicates that impurity outgassing increases, and the discharge no longer consists of a pure noble gas.

3.4 Momentum Coupling Through Collisional Viscosity

Momentum transport through the action of viscosity is an ubiquitous phenomena in fluid systems. In the simplest sense, viscosity can be thought of as the ability of a fluid to transfer momentum through collisions as particles move, due to thermal motion, between layers that are flowing at different speeds. The viscosity of an (unmagnetized) plasma can be understood by considering a linear shear flow (see Fig. 3.5) with velocity directed in the y-direction, which can be written as $\mathbf{u}(\mathbf{x}) = \left[u_0 + (x - x_0)\frac{du}{dx}\right]\hat{y}$.

The fluid to the left of the plane at $x = x_0$ exerts a stress, or force per unit area P_{xy}, on the fluid to the right of $x = x_0$. At the microscopic level, momentum in the y-direction is lost on the right of $x = x_0$ as particles with less momentum arrive from the left, and vice versa. If most of the momentum is carried by particles with density n and thermal velocity v_t, one might expect that at any given time, $n/3$ have momentum in the x-direction. If the particles which cross the plane at $x = x_0$ are at most a mean free path, λ, away, then the flux of particles crossing the $x = x_0$ plane from $x_0 \pm \lambda$ is $\Gamma = 1/2\,(n/3)\,v_t$ [m^{-2} s]. Thus, the net change in momentum per unit area at $x = x_0$ is:

$$P_{xy} = P^- - P^+ = \frac{1}{6} n v_t m \left(u_0 - \lambda \frac{du}{dx} \right) - \frac{1}{6} n v_t m \left(u_0 + \lambda \frac{du}{dx} \right) \tag{3.4}$$

or

$$P_{xy} = -\frac{1}{3} \rho v_t \lambda \frac{du}{dx} \tag{3.5}$$

In this case, the dynamic viscosity coefficient is $\eta = \frac{1}{3}\rho v_t \lambda [\mathrm{kgs}^{-1}\mathrm{m}^{-1}]$, which can be divided by ρ to obtain the kinematic viscosity, $\nu[\mathrm{m}^2\mathrm{s}^{-1}]$. Since the viscosity coefficient depends on particle mass, the bulk viscosity is determined mainly by the ions, and the contribution of momentum transfer by electrons can be neglected entirely due to their small mass. Thus, the mean free path is determined by the ion-ion collision time, $\lambda_{mfp} = v_{ti}\tau_{ii}$. Therefore, the plasma kinematic viscosity coefficient can be estimated in this simple example as $\nu \propto v_{ti}^2 \tau_{ii}$.

3.4.1 Braginskii Viscosity

In general, viscosity is a tensor which can be highly anisotropic, especially for plasma in the presence of strong magnetic fields. In a strongly magnetized plasma, the viscous stress becomes predominantly aligned parallel to the magnetic field, and the parallel viscosity takes on the same value as in an unmagnetized plasma based on mean free path between ion-ion collisions. The perpendicular viscosity, however, is much smaller because the mean free path is effectively replaced by the ion gyroradius. Consequently, momentum transport across magnetic field lines is strongly suppressed.

An elegant summary of the ion viscosity coefficients can be found in Braginskii (1965) [63], where the viscous stress tensor is derived by computing the viscous stress moment of the kinetic equation for the particle distribution function. This rigorous derivation gives expressions for viscosity which vary continuously from unmagnetized to magnetized regions. According to Braginskii, the magnetized perpendicular viscosity is

$$\nu_1 = \frac{v_{ti}^2 \tau_{ii}}{\Delta} \left(\frac{6}{5} (2\chi)^2 + 2.23 \right) \quad [\mathrm{m}^2/\mathrm{s}] \tag{3.6}$$

where $\Delta = (2\chi)^4 + 4.03(2\chi)^2 + 2.33$, $\chi = \Omega_{ci}\tau_{ii}$ is the magnetization parameter, Ω_{ci} is the ion cyclotron frequency multiplied by 2π, v_{ti} is the ion thermal speed. The ion-ion collision time τ_{ii} is defined by Braginskii as

$$\tau_{ii} = \frac{3 \times 10^6}{\Lambda/10} \frac{T_i^{3/2}}{Z^3 n} \sqrt{\mu/2} \tag{3.7}$$

where the Coulomb logarithm for $T_e < 50$ eV is $\Lambda = 23.4 - 1.15\log(n) + 3.45\log(T_e)$. Here, density n is in cm^{-3}, T_e, T_i are electron and ion temperatures in eV, and μ is ion atomic mass.

In the magnetized limit, where $\Omega_{ci}\tau_{ii} >> 1$, the viscosity becomes $\nu_1 = \frac{3}{10} v_{ti}^2 \tau_i / \chi^2$. In the unmagnetized limit, where $\Omega_{ci}\tau_{ii} << 1$, the viscosity is simply

$$\nu_0 = 0.96 v_{ti}^2 \tau_{ii} \ \ [\mathrm{m}^2/\mathrm{s}]. \tag{3.8}$$

3.4.2 Viscosity Profiles in PCX

In multicusp plasmas, the viscosity changes dramatically over the plasma profile: in the edge where the plasma is magnetized, the cross-field kinematic viscosity is $\nu_1 \propto \frac{n\sqrt{mu}}{B_0^2\sqrt{T_i}}$. However, in the core, the plasma is unmagnetized (given by Eq. 3.8) and the viscosity increases dramatically to $\nu_0 \propto \frac{T_i^{5/2}}{n\sqrt{mu}}$.

It becomes apparent that a final consideration for cathode placement involves the perpendicular ion viscosity. In Fig. 3.6, the magnetized viscosity and magnetization factor are plotted for both argon and helium, given by Eq. 3.6, for identical plasma parameters of $T_e = 6$ eV, $T_i = 0.1$ eV, and $n = 2 \times 10^{10}$ cm^{-3} which are assumed to be constant throughout the magnetized boundary in this calculation. In order for the momentum to couple from the magnetized edge into the bulk plasma, the electrodes must be in a region with sufficiently low magnetic field so that the viscosity is large enough. Note that Braginskii's viscosity only applies when the ion-ion collision time is more frequent than the ion-neutral collision time: $\tau_{ii} < \tau_{i0}$.

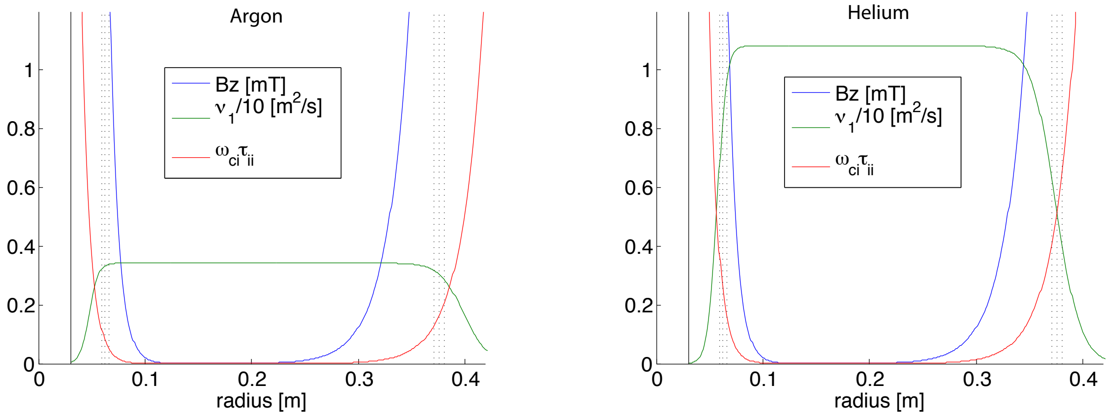

(A)

(B)

Figure 3.6: Comparison of argon and helium viscosity and magnetization with identical parameters of $T_e = 6$ eV, $T_i = 0.1$ eV, and $n = 2 \times 10^{10}$ cm^{-3}. In the calculation, plasma parameters are assumed constant across the radius, and magnetic field B_z is based on Eq. 2.1. Dashed lines represent the location of inner and outer flow-drive cathodes.

3.5 Velocity Limits

3.5.1 Critical Ionization Velocity

The velocities measured in the PCX experiment have increased through the optimization of electrode locations and realization that plasma conditions are optimized at low density (where viscosity is largest) and a low neutral pressure (where neutral drag is minimized). It seems, however, that as long as the plasma remains partially ionized, velocity limits do exist and are consistent with the species-dependent critical ionization velocity first proposed by Alfvén in 1954. Alfvén hypothesized that if the ion flow kinetic energy exceeds the ionization potential of the neutrals, the ionization rate of a neutral gas should strongly increase. The critical ionization velocity (CIV) is reached when the relative velocity between the plasma ions and neutral gas reaches the value

$$V_{crit} = \sqrt{\frac{2eU_i}{m_n}} \tag{3.9}$$

where U_i is the ionization potential and m_n is the mass of the neutral atom.

Alfvén originally proposed that the CIV mechanism may have played a role in ionizing gas during the formation of the solar system: Neutral gas gained energy as it fell towards the Sun through gravity and eventually reached the critical velocity V_{crit}, resulting in ionized gas that could be trapped by magnetic field and lead to mass concentrations and eventual planet formation. Since then, hundreds of papers and several extensive review articles [64, 65] have been written about the CIV effect. Rather remarkably, the simple velocity limit set by Eq. 3.9 has been confirmed in numerous experiments with a variety of geometries, spanning orders of magnitude in various neutral gas, plasma, and magnetic field conditions. The CIV mechanism may also be occurring in several situations in space, such as the solar wind interaction with comet tails, the Io-Jupiter torus system in which Jupiter's rapidly rotating magnetosphere interacts with neutral gas emitted from Io's volcanoes, the ionization of gas in space shuttle exhaust, and could potentially place velocity limits in plasma thruster powered spacecraft.

The laboratory experiments that have been designed especially to study CIV generally create flowing plasma with either homopolar-type devices that implement cross-field discharges, or with coaxial plasma guns to create a plasma beam colliding with neutral gas. Investigations of many gas species found that the maximum E/B velocity was typically within 50% of V_{crit} (as long as the plasma remained partially ionized), where the magnitude of the velocity was inferred by E/B or by the Doppler shift of spectral lines.

While CIV has been well documented in experiment, the underlying physics is not well understood. When an ion collides with a neutral, the probability of ionizing the atom is low unless the velocity of the ion *exceeds* that of Eq. 3.9 (by at least a factor of 10). This suggests that it is probably not direct ion-neutral collisions creating the enhanced ionization. The literature also states that the CIV apparently requires a minimum magnetic field to occur. It has been suggested that the CIV mechanism is driven by some type of magnetized two-stream instability or possibly by a nonlinear wave-particle acceleration involving turbulence. In the end, Landau damping processes cause ions to lose kinetic energy to plasma waves, and wave-particle interactions in turn energize electrons in the tail, which can go on to ionize the neutrals through electron impact ionization.

3.5.2 Peak Velocities Measured in PCX

The peak velocities measured in PCX for four different gas species (helium, neon, argon, xenon) are listed in Table 3.1. The velocities were measured with a Mach probe at the midplane near the outer edge of the unmagnetized region, around $r = 0.34$ m. Density and electron temperature were measured with both the single swept Langmuir probe and triple probe. In all cases, the peak speeds were always less than the calculated V_{crit} for each species. While $V_{max} < V_{crit}$, it is conceivable that peak velocities reached higher speeds in regions of the plasma that were not measured by the Mach probe, for example directly in front of the permanent magnets where $\mathbf{J} \times \mathbf{B}$ forces are large. Attempts were made to further increase the velocity by increasing $\mathbf{J}$ (by increasing the filament temperature and bias). This resulted in increased density and undesirable filament arcing (as described in Section 2.5.1) and often caused the plasma to switch from the underdense to overdense state in microwave discharges. Interestingly, the ratio of $V_{max}/V_{crit} \sim 0.3$ for all gases tested. Thus, it seems that a velocity limit which depends on the species mass and ionization potential (consistent with CIV phenomenon) is observed in PCX.

Gas	$\mathbf{U_i}$ (eV)	$\mathbf{M_i}$ (a.m.u)	$\mathbf{V_{crit}}$ (km/s)	$\mathbf{V_{max}}$ (km/s)	$\mathbf{V_{max}/V_{crit}}$	**Ref. Shot** $\#$	$\mathbf{n \times 10^{10}}$ (cm^{-3})	$\mathbf{f_{ion}}$ (%)	**Te** (eV)	$\mathbf{Ti_{fit}}$ (eV)
He	24.6	4	34	12	0.35	609	2.3	0.7	6.9	0.21
Ne	21.6	20.2	14	4	0.29	684	3.4	1.2	7.7	0.3
Ar	15.8	40	8.7	3.2	0.37	656	3	9.5	5.9	0.135
Xe	12.1	131.3	4.2	1.35	0.3	668	6	32	3.6	0.15

Table 3.1: Summary of ionization energy, mass, critical ionization velocity, maximum induced velocities for different gas species in PCX as measured by the Mach probe. Also listed for reference are the corresponding n, T_e, and the ionization fraction $f_{ion} \equiv n/n_o$. Note that V_{max} is always less than V_{crit}, with $V_{max}/V_{crit} \sim 0.3$ in all cases.

Chapter 4

Equilibrium Properties of Unmagnetized Couette Flow of Plasma

The PCX plasma is unique in that it is a steady state discharge with axisymmetric, flowing, unmagnetized plasma. In contrast to homopolar-type devices, the rotation drive scheme does not require any radial currents throughout the bulk of the plasma, simplifying the plasma equilibrium properties. The magnetized edge region is complicated by magnetic field, density, and temperature gradients and will not be treated here. Instead we focus on the unmagnetized bulk region of the plasma, assuming that the edge-applied torque simply sets the boundary condition for the velocity at the edge.

4.1 Toroidal Equilibrium

The dominant momentum loss mechanism for the ions is assumed to be ion-neutral charge exchange collisions, in which a positive ion can collide with a neutral atom and capture a valence electron, leaving a fast moving, unconfined neutral and a stationary, newly formed ion. In order for toroidal velocity to couple inward from the edge and stir the unmagnetized core plasma, the viscous momentum diffusion must be greater than the drag due to ion collisions with neutrals. This requirement can be deduced from the toroidal momentum equation

$$mn\frac{dv_\phi}{dt} = (\mathbf{J}\times\mathbf{B})_\phi - \frac{mnv_\phi}{\tau_{i0}} + mn\nu[\nabla^2\mathbf{v}]_\phi, \tag{4.1}$$

where m is the ion mass, $\tau_{i0} \approx (n_0\langle\sigma_{cx}v\rangle)^{-1}$ is the ion-neutral collision time, σ_{cx} is the charge-exchange cross-section, and ν is the viscosity due to ion-ion collisions.

The first term on the right-hand side is the electromagnetic force on the plasma from the injected current in the magnetized region. This term vanishes in the core of the plasma where the magnetic field is essentially zero. The second term is the momentum loss due to charge-exchange collisions with neutrals. Since the ionization mean-free path for neutrals is longer than the experiment size, neutrals are not strongly coupled to ions and we can assume a uniform background of stationary neutrals. The final term couples momentum inward through viscosity.

We turn now to the flow in the unmagnetized region. In steady state, the left-hand side of Eq. 4.1 is zero. Also, in the unmagnetized region, we have $\mathbf{J} \times \mathbf{B} = 0$. If we further assume that the system is uniform in the vertical direction, the velocity in the bulk is determined by

$$\frac{\partial^2 v_\phi}{\partial r^2} + \frac{1}{r}\frac{\partial v_\phi}{\partial r} - \left(\frac{1}{L_v^2} + \frac{1}{r^2}\right) v_\phi = 0 \tag{4.2}$$

where $L_v^2 \equiv \tau_{i0}\nu$. The solution involves modified Bessel functions

$$v_\phi(r) = A\mathrm{I}_1(r/L_v) + B\mathrm{K}_1(r/L_v), \tag{4.3}$$

where the constants A and B depend on the velocity applied at the inner and outer boundaries of the unmagnetized region:

$$\begin{aligned} A &= \frac{K_1(R_2/L_v)V_1 - K_1(R_1/L_v)V_2}{I_1(R_1/L_v)K_1(R_2/L_v) - I_1(R_2/L_v)K_1(R_1/L_v)} \\ B &= \frac{I_1(R_1/L_v)V_2 - I_1(R_2/L_v)V_1}{I_1(R_1/L_v)K_1(R_2/L_v) - I_1(R_2/L_v)K_1(R_1/L_v)} \end{aligned} \tag{4.4}$$

with R_1 and V_1 defining the inner radius and velocity, while R_2 and V_2 define the outer radius and velocity. Note that in the absence of ion-neutral collisions, the solution is simply Taylor-Couette flow with $v_\phi(r) = Cr + D/r$ (where C and D are again constants which depend on the boundary conditions).

In order for the unmagnetized plasma to spin, the characteristic momentum diffusion length scale, L_v, should be comparable to the experiment size or larger. When L_v is small, the rotation (Eq. 4.3) remains confined near the edge region. We may write out the dependence of L_v on plasma parameters by using Braginskii's unmagnetized viscosity Eq. 3.8:

$$L_v \equiv \sqrt{\tau_{i0}\nu} = 21 \text{ cm} \frac{\sqrt{f_{i,1\%}} T_{i,eV}}{n_{11}}, \tag{4.5}$$

where $f_{i,1\%}$ is the ionization fraction in percent ($f_i \equiv n/n_0$), $T_{i,eV}$ is the ion temperature in eV and n_{11} is the electron density in units of 10^{11} cm^{-3}. Therefore, velocity couples into the core for low density, high ion temperature and high ionization fraction, or in other words, when the viscous momentum diffusion is large compared to the ion-neutral drag. Note that Braginskii's viscosity only applies when the ion-ion collision time satisfies $\tau_{ii} \ll \tau_{i0}$.

From the measured velocity profiles and Eq. 4.3 we may find L_v and thereby measure the ion temperature in the unmagnetized region. For this measurement we use the measured plasma and neutral densities and the charge-exchange cross-section, and the only fit parameter is the ion temperature. Since the fitted region is restricted to the unmagnetized bulk, the density and temperature profiles are constant and can be take as single values in the the calculation. The charge exchange cross section values used in this thesis are:

$$\sigma_{cx} \quad = \begin{cases} 3 \times 10^{-19} T_i^{-.106}, & \text{He} \\ 4.5 \times 10^{-19}, & \text{Ne} \\ 6 \times 10^{-19} T_i^{-.093}, & \text{Ar} \\ 1 \times 10^{-18}, & \text{Xe} \end{cases} \tag{4.6}$$

as given by [66, 67, 68, 69]. The velocity value in $\langle \sigma_{cx} v \rangle$ should be taken as the largest velocity with respect to the neutrals. Since it is not always true that $v_{ti} > v_\phi$ for all radii in the plasma, a comparison is made with an 'average' measured flow velocity, $v_{avg} = 0.5(V_1 + V_2)$, and the larger of the two velocities is used to approximate $\langle \sigma_{cx} v \rangle$.

4.1.1 Applying the Azimuthal Velocity Model to Measurements

The velocity fits demonstrate excellent agreement with the Mach probe velocity data, and the ion temperatures predicted by the fits are typical of plasmas confined in multicusps [70]. Fitted velocity profile measurements for argon are shown in Fig. 4.1b for three different times, and therefore three different neutral pressures. Note that although the plasma flow is changing throughout the shot, we have quasi-steady state because the viscous time, $L^2/\nu = 10^{-4}$ s, is short.The measured plasma parameters are listed in Table 4.1. As the neutral gas puff is pumped out, the density decreases (increased viscosity), ionization fraction increases (less drag), and the rotation velocity increases everywhere with time.

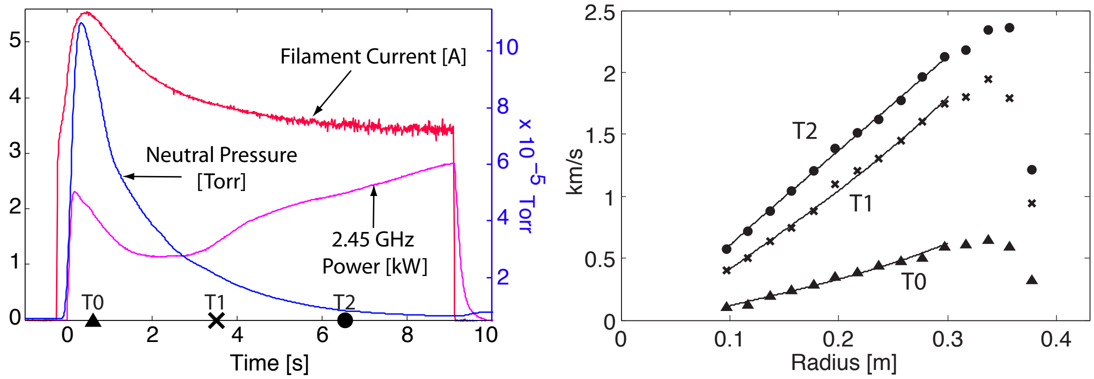

(a) (b)

Figure 4.1: a) Typical plasma discharge: plasma density decreases and electron temperature increases as the puff of neutral gas is pumped out. b) Velocity profiles in argon at times labeled in (a) for two outer cathodes biased to 400 V. Rotation increases at low density and high ionization fraction. Solid lines represent a model incorporating unmagnetized Braginskii viscosity and neutral drag (due to charge exchange), using parameters from Table 4.1.

Case	**n x 10^{11}** (cm^{-3})	f_{ion} %	**Te** (eV)	**Ti**$_{fit}$ (eV)	**V**$_{max}$ (km/s)	**Rm**	**Re**	**Pm**
Ar400VT0	4.2	12	2.6	1.2	0.6	0.8	2	0.5
Ar400VT1	1.1	15	5.9	0.42	1.8	7	23	0.3
Ar400VT2	.77	27	7	0.6	2.2	11	8	1.3
He400VT1	.45	0.6	11	0.4	2.4	22	5	4.5

Table 4.1: Summary of induced velocities for different gas species (helium, argon), with 400 V biased cathodes, at various times throughout a plasma pulse (T0,T1,T2 as in Fig. 4.1); these times are characterized by varying plasma densities, ionization fractions, and temperatures.

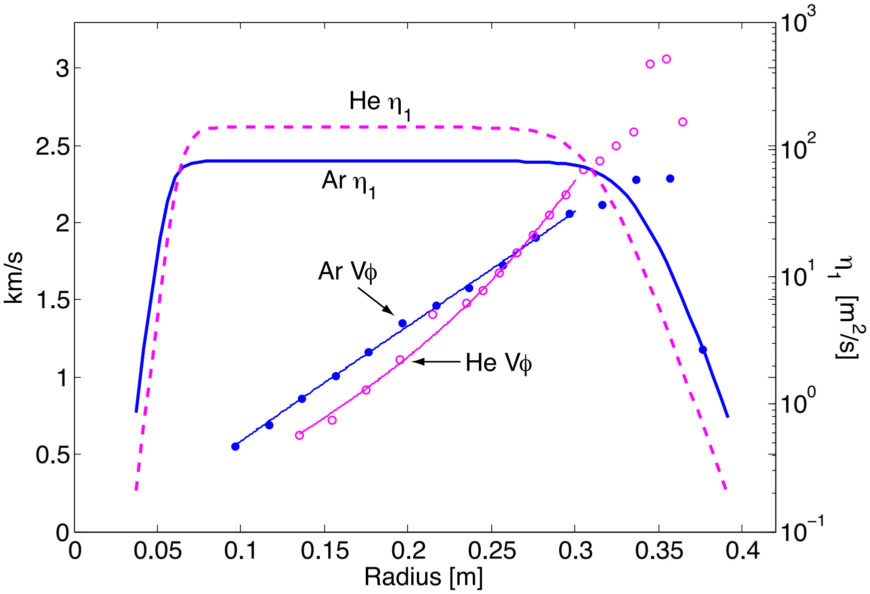

Figure 4.2: Braginskii viscosity (ν_1, see Eq. 3.6) varies continuously from unmagnetized to magnetized regions; torque is applied at $r \approx 0.36$ m to induce rotation at the outer boundary. The calculated viscosity assumes constant density and temperature values as listed under “He400VT1” and “Ar400VT2” in Table 4.1.

For the plasma parameters in Fig. 4.1, the velocity is approximately linear with radius, implying solid-body rotation with minimal momentum loss through charge-exchange collisions. More significant charge-exchange effects on the velocity profile can be clearly seen in Fig. 4.2. In comparing the argon and helium profiles, two important features can be noted. First, the viscosity of helium is smaller, resulting in larger peak at the edge. Next, the ionization fraction of helium is smaller, causing a 'dipped' rotation profile in the bulk as ions lose momentum to neutrals.

It would be interesting to observe the viscous "spin-up" , or diffusion time. This experiment has not yet been performed, but one idea to measure the left had side of Eq. 4.1 is to modulate the bias voltage on the outer cathodes with a high frequency square wave while radially scanning the Mach probe. The diffusion time could be found by measuring the delay in propagation (which should increase as the probe moves away from the outer cathodes). This *might* be accomplished very simply with an AC power supply inline with the anodes, which float near ground, to prevent the power supply from being biased at large negative cathode bias voltages. In order to take time-resolved date, the DTACQ data acquisition rate would need to be increased, as it currently only takes data at a rate of 10 kSamples/sec (its maximum is 500 kSamples/sec). The bandwidth on the current Mach probe isolation amplifier board circuits would also need to be increased.

One of the highest speed flows generated from flow drive at the outer boundary is shown in Fig. 4.3. In this case, two outer cathodes were biased 550 V to draw 2 Amps each in a helium plasma. Plasma was created using simultaneous gas puff and microwaves, and cathode bias was applied later in the shot. A significant increase in ionization occurs due to cathode biasing, with f_{ion} approaching 1% towards the end of the shot. The azimuthal velocity profile, measured with the radially scanned midplane Mach probe, indicated a peak flow speed of 5.5 km/s. The azimuthal velocity profile is plotted for the time indicated by the vertical dashed lines in Fig. 4.3a-b, where $P = 2 \times 10^{-4}$ Torr, $n = 6.2 \times 10^{10}$ cm^{-3}, $T_e = 9.1$ eV, and $T_i = 0.7$ eV (found from the fitted velocity profile), resulting in $Pm = 10.7$ and $Rm = 50$.

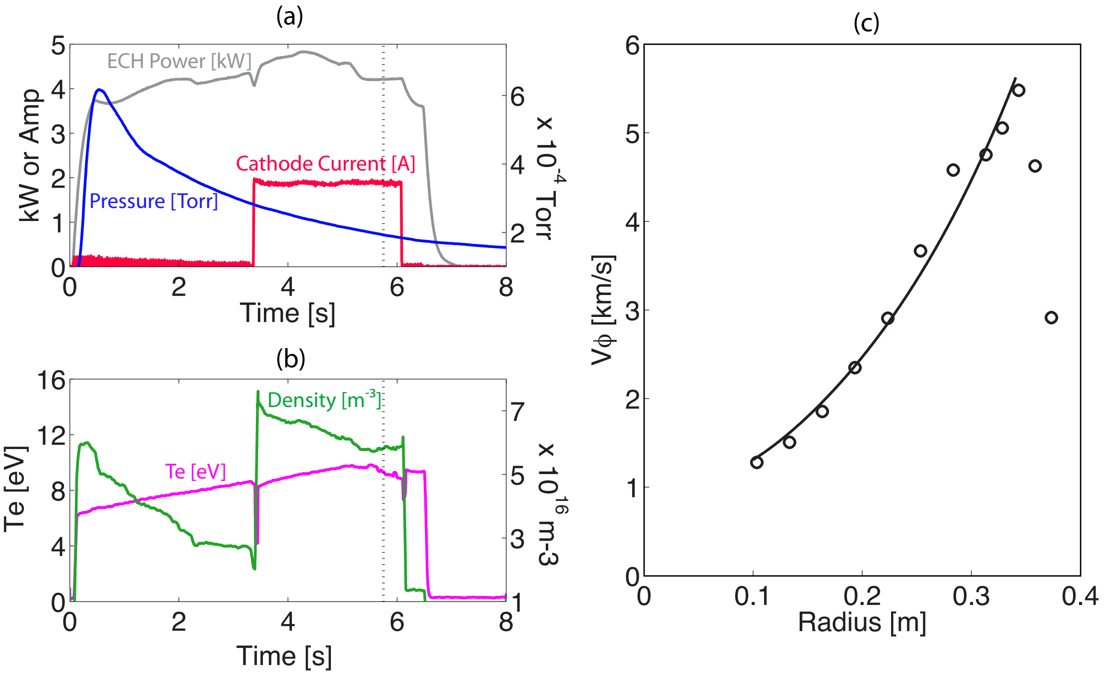

Figure 4.3: High speed helium solid body rotation. a) Plasma was created with a puff and ECH heating. At a later time, two outer cathodes were biased 550 V and drew $\sim$ 2 Amps each. b) Plasma density and electron temperature vs. time, measured with the triple probe. c) Azimuthal velocity profile late in the plasma discharge (time marked by dashed line in (a) and (b)). Here, $P = 2 \times 10^{-4}$ Torr, $n = 6.2 \times 10^{10}$ cm^{-3}, $T_e = 9.1$ eV, and $T_i = 0.7$ eV, resulting in $Pm = 10.7$ and $Rm = 50$.

4.1.2 Estimating the Torque Required to Spin the Plasma

If the main momentum loss mechanism for the spinning plasma is ion-neutral charge exchange, the torque required to spin an annulus of plasma is

$$\mathcal{T}_{CX} = \int_0^h \mathrm{d}z \int_{r_i}^{r_o} (\mathbf{r} \times mnn_o\sigma_{cx}v_{ti}\mathrm{V}_\phi\hat{\phi})(2\pi r\,\mathrm{d}r) \tag{4.7}$$

$$= 2\pi hmnn_o\sigma_{cx}v_{ti}\Omega_0\frac{(r_o^4 - r_i^4)}{4} \tag{4.8}$$

assuming $\mathrm{V}_\phi = r\Omega_0$. Here, $h \sim 0.1$ m is the vertical span of the plasma annulus spun by a single cathode and anode pair, $r_i = 0.065$ m, $r_o = 0.375$ m.

The edge-localized electromagnetic torque input can be crudely estimated using

$$\mathcal{T}_{EM} = \int_0^h \mathrm{d}z \int_0^{\Delta\phi} \mathrm{d}\phi \int_{r_{o-}}^{r_{o+}} r^2 J_\perp B_0\,\mathrm{d}r \tag{4.9}$$

$$= h\Delta\phi J_\perp B_0\frac{(r_{o+}^3 - r_{o-}^3)}{3} \tag{4.10}$$

The cathodes apply torque between $r_{o-} = 0.37$ m and $r_{o+} = 0.38$ m, where the magnetic field is approximately $B_0 = 0.007$ T. The azimuthal extent of the applied torque is taken to be $\Delta\phi \sim 0.07$ radians. The required current density can by found by equating Eq. 4.10 and 4.8;

$$J_\perp = \frac{3}{2}\frac{\pi}{\Delta\phi B_0}mnn_o\sigma_{cx}v_{ti}\Omega_0\frac{(r_o^4 - r_i^4)}{(r_{o+}^3 - r_{o-}^3)} \tag{4.11}$$

Using the parameters for helium shown in Fig. 4.3 ($P = 2 \times 10^{-4}$ Torr, $n = 6.2 \times 10^{10}$ cm^{-3} $T_i = 0.7$ eV, and $\mathrm{V}_\phi = 5.5$ km/s at $r = 0.33$ m) we find that the required cathode current density is $J_\perp = 0.48$ A/cm^2, or approximately 2.7 A, which is within reasonable comparison to the measured current of 2 A. The argon velocity profile in Fig. 4.6 was generated with an order of magnitude lower in neutral pressure ($P = 1 \times 10^{-5}$ Torr, $n = 1.5 \times 10^{10}$ cm^{-3} $T_i = 0.1$ eV, and $\mathrm{V}_\phi = 3.2$ km/s at $r = 0.33$ m) and required ~ 1 A per cathode. In that case, $\mathcal{T}_{CX}/\mathcal{T}_{EM} = 4\%$, which seems to indicate that charge-exchange loss alone cannot account for the total applied torque. Certainly a better understanding of current paths is required. One cause of discrepancy could be shorting of current across the face of the magnets, for example, if the surface becomes coated with conducting material. To monitor this, it would be useful to measure the voltage of each individual magnet ring in future machine upgrades.

4.2 Vertical Equilibrium

If the applied torque is a function of vertical height, z, then the azimuthal equation of motion (Eq. 4.2) should include an extra z-dependent term:

$$\frac{\partial^2 v_\phi}{\partial z^2} + \frac{\partial^2 v_\phi}{\partial r^2} + \frac{1}{r}\frac{\partial v_\phi}{\partial r} - \left(\frac{1}{L_v^2} + \frac{1}{r^2}\right) v_\phi = 0 \tag{4.12}$$

With $v_\phi = R(r)Z(z)$, the vertical solution must satisfy

$$\frac{\partial^2 v_\phi}{\partial z^2} + \lambda^2 Z(z) = 0 \tag{4.13}$$

resulting in

$$v_\phi(r,z) = \left(\hat{A} I_1(\alpha r) + \hat{B} K_1(\alpha r)\right) e^{-\lambda z} \tag{4.14}$$

where $\alpha = \sqrt{\lambda^2 + 1/L_v^2}$. The constants $\hat{A}(\alpha)$, $\hat{B}(\alpha)$ are similar in form to Eq. 4.5, and λ can be found by using the boundary conditions $V_1 = v_\phi(R1, z = 0)$, $V_2 = v_\phi(R2, z = 0)$, $V_{z0} = v_\phi(R_3, z = Z_0)$, and a transcendental equation for λ.

Azimuthal velocity measurements were made with a vertically scanned, 4-tipped Mach probe (pictured in Fig. 2.1). The probe tips were spaced 1.5 cm radially. Regular cleaning of the vertical probe array is prohibitive, as it does not have a gate valve and requires a machine vent to remove the flange. As the probe becomes dirty over time, it seems to result in an increase in collection area, resulting in a net velocity offset. The vertical probe array can be rotated 180° to check the accuracy of the velocity measurement, but this process can only check the single probe on axis. Therefore, the vertical probe array was also checked against a radially scanned Mach probe at $z = 0.5$ m (which is regularly cleaned to maintain accuracy), and measured velocities of the vertical probe array were adjusted to match those measured by the radially scanned probe through additive offsets.

The main effect of four cathodes vs. two cathodes is just what is expected: with four biased cathodes, the entire column of plasma rotates. This can be clearly seen in the vertical probe array scan, shown in Fig. 4.4. When only the midplane is spinning (with two cathodes), the azimuthal velocity $v_\phi(r,z)$ seems to follow the expected profiles given by Eq. 4.14 (see Fig. 4.5a). When a Mach probe is scanned radially at the height of $z = 0.5$ m (Fig. 4.5b), the velocity increases as the

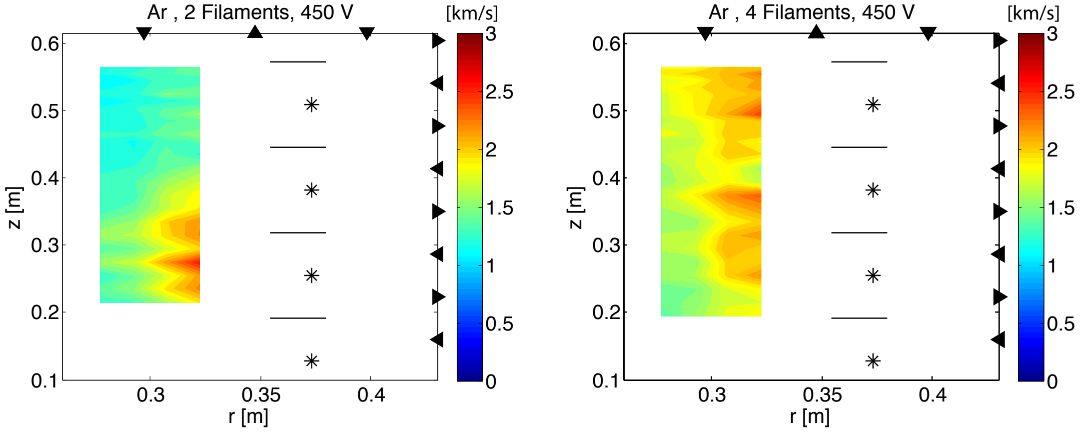

(a) (b)

Figure 4.4: Argon azimuthal velocity measured with vertically scanned, 4-tipped Mach probe, with 450 V for ~ 1 Amp from each biased cathode with a) two biased cathodes vs. b) four biased cathodes. Triangles mark the location of magnets, anodes (solid lines) and cathodes (stars) are located around $r = 0.37$ m.

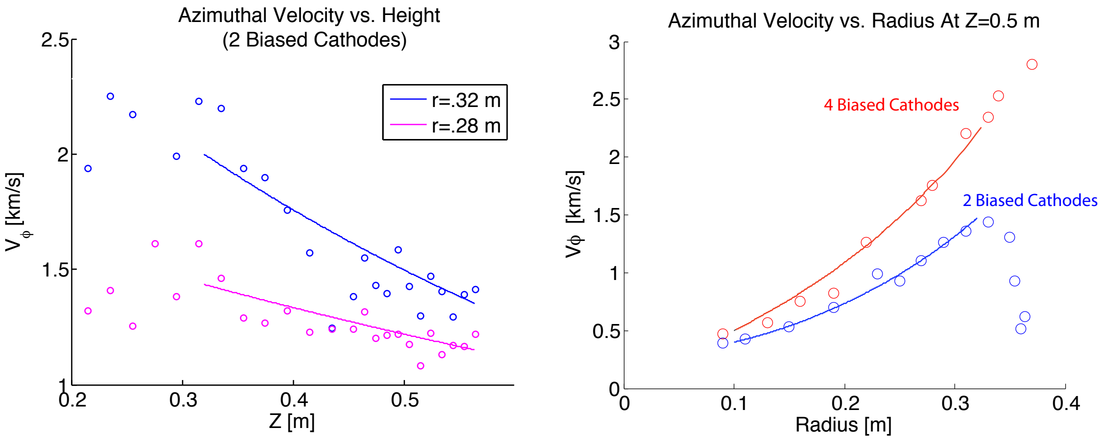

(a) (b)

Figure 4.5: a) Azimuthal velocity vs. height with two biased cathodes at the midplane. Solid lines are fits based on Eq. 4.14. b) Azimuthal velocity vs. radius for two vs. four biased cathodes, measured with a radially scanned Mach probe at $z = 0.5$ m. Solid lines are fits based on Eq. 4.3.

additional cathode is biased at the same height of $z = 0.5$ m. The plasma parameters (measured by the triple probe) were similar for each case. With two cathodes biased, $n = 3.2 \times 10^{10}$ cm$^{-}3$, $f_{ion} = 9.9\%$, $T_e = 6.3$ eV, and $T_i = 0.12$ eV (from fitting the velocity profile). When four cathodes were biased, $n = 2.2 \times 10^{10}$ cm^{-3}, $f_{ion} = 7.6\%$, $T_e = 7.2$ eV, and $T_i = 0.1$ eV.

4.3 Radial Equilibrium

In a strongly rotating plasma, where the magnitude of the toroidal velocity of the plasma is comparable to the thermal velocity, the centrifugal force begins to influence plasma motion, causing ions to move to larger radii. In astrophysical systems such as accretion disks or the Sun, the ions are held in orbit by gravity. What, then, keeps the unmagnetized, spinning plasma confined in a laboratory experiment?

As with any gas centrifuge, the outward displacement of spinning plasma creates a pressure gradient, resulting in an inward force to balance the outward centrifugal acceleration. In a plasma, however, the centrifugal force on the electrons is small due to their low mass. Since the electron density must match the ion density to maintain quasineutrality, there must be a radial electric field which arises to move electrons radially outward. In the case of and unmagnetized flow with uniform temperature, the radial force balance equation for ions can be written:

$$-n_i M_i \frac{V_\phi(r)^2}{r} = -Zen_i \frac{d\Phi}{dr} - T_i \frac{dn_i}{dr} \tag{4.15}$$

where Φ is the electrostatic potential. Neglecting the small centrifugal force on the electrons, the electron momentum balance equation becomes:

$$0 = en_e \frac{d\Phi}{dr} - T_e \frac{dn_e}{dr} \tag{4.16}$$

Thus, the electrons simply obey the Boltzmann relation, responding to changes in the potential by varying their density:

$$n_e = n_0 \exp(e\Phi/T_e) \tag{4.17}$$

So, the ions are ultimately held in orbit by both the ion pressure gradient force and the electric field determined by the electron pressure. With the quasineutrality condition ($n_e \approx Zn_i$), Eq. 4.17

can be substituted into Eq. 4.15. This results in a radial potential profile which depends on the ion mass and the rotation profile:

$$\frac{d\Phi}{dr} = \frac{1}{e(Z+\frac{T_i}{T_e})}\frac{M_i V_\phi(r)^2}{r} \tag{4.18}$$

or,

$$\Phi(r) = \frac{1}{e(Z+\frac{T_i}{T_e})} M_i \int_{R_1}^{R_2} \frac{V_\phi(r)^2}{r} dr \tag{4.19}$$

This argument has been presented in the context of tokamaks, where strong toroidal rotation causes mass separation of heavy impurity ions, and large enhancement of impurities have been observed on the outboard side of tokamak plasmas [71]. In PCX, measurements of the radial electric field are an important tool for verifying the Mach probe velocity measurements.

4.3.1 Measurements of the Predicted Radial Electric Field

The PCX plasma provides a unique environment to measure the rotation-induced radial electric field. In particular, the PCX rotation drive scheme does not require radial electric fields applied to the bulk, in contrast to most homopolar-type devices which create $E \times B$ flow. It would therefore be expected that a radial electric field appearing in the PCX plasma would be self-generated.

Estimates show that the magnitude of the expected rotation-induced radial electric field should be measurable in the experiment. For example, in an argon plasma with $V_\phi = 2$ km/s at r =0.3 m, it is estimated that $E = \frac{M_i V_\phi^2}{eR} = 0.06$ V/cm. With rigid rotation profiles where $V_\phi(r) = \Omega_0 r$, the potential difference across the spinning, unmagnetized region of the PCX plasma would be $\Delta\Phi = \frac{M_i}{2e}\Omega_0^2(R_2^2 - R_1^2) \approx 0.7$ V.

Several approaches have been made to measure the radial plasma potential profiles. The first was to use an emissive probe, which consisted of a single strand of thoriated tungsten wire heated ohmically to thermionically emit electrons. Emissive probes can be understood by considering the I-V characteristics. If the probe is biased more positive than the local plasma potential, electrons emitted from the probe are reflected back to the probe. When the probe is biased more negative than the local plasma potential, electrons can escape to the plasma and appear as an effective ion current. The I-V characteristics tend to separate near V_p, and V_f moves toward more positive voltages (near V_p) as probe is heated. The simplest approach is to measure the floating potential of the probe and assume that, for a strongly emitting probe, $V_f \approx V_p$. Emissive probe measurements are unfortunately not without error. Any drift in the probe temperature can cause changes in the measured floating potential. If DC heating is used, the measured floating potential will include the voltage drop across the filament. A more advanced method was attempted, which involved using AC heating with a diode, and restricting measurements of the floating potential to the off cycle when the applied heating voltage was zero. It was found that measuring the floating potential 'half' of the time is not necessarily the best approach to use in plasmas with a lot of low frequency noise, especially in the PCX which exhibits plasma fluctuations at 60 Hz and harmonics.

The successful method has been to simply measure the floating potential of cold probes and assume that the floating potential is proportional to the plasma potential, according to the relation $\Phi_p = \Phi_{fl} - \frac{T_e}{2}(\ln(2\pi m_e/m_i) - 1)$ [72]. As long as T_e is constant in radius, then $\Phi_{fl} \sim \Phi_p$. The radial electric field was measured with a combination Mach/rake probe consisting of a single Mach probe along with multiple radially-spaced tips to measure floating potential, as described in Section 2.6.4. The rake probe measurements could be used to derive the radial electric field, however, the measurements tended to be very noisy and better results were obtained by simply measuring the potential profile and comparing to Eq. 4.19.

To measure the potential profiles, the probe was moved to a different position for each plasma pulse. Over the course of many plasma pulses, a number of measurements were recorded at each radial location, and the floating potential was then taken as the mean value of between multiple shots. Efforts were made to maintain consistent plasma conditions, but the bulk plasma potential still varied slightly from shot-to-shot. To adjust for these shot-to-shot differences, the floating potential was simultaneously measured by the fixed triple probe and subtracted from the rake probe floating potential measurements. Of course, Eq. 4.19 only applies if there are no temperature gradients across the bulk, which seems to be a valid assumption, especially for multicusp confinement. Since we are considering the bulk, unmagnetized region away from any possible sources of electron heating (ECH resonance, joule heating due to biased cathodes), the electron mean free paths are quite long, resulting in uniform distribution in the bulk. For example, at $T_e = 5$ eV, $v_{te} = 940$ km/s and $\nu_{ee} = 1 \times 10^5$ s^{-1}, so $\lambda_{mfp} \sim 9.4$ m. (Arguably, the electrons are slightly magnetized

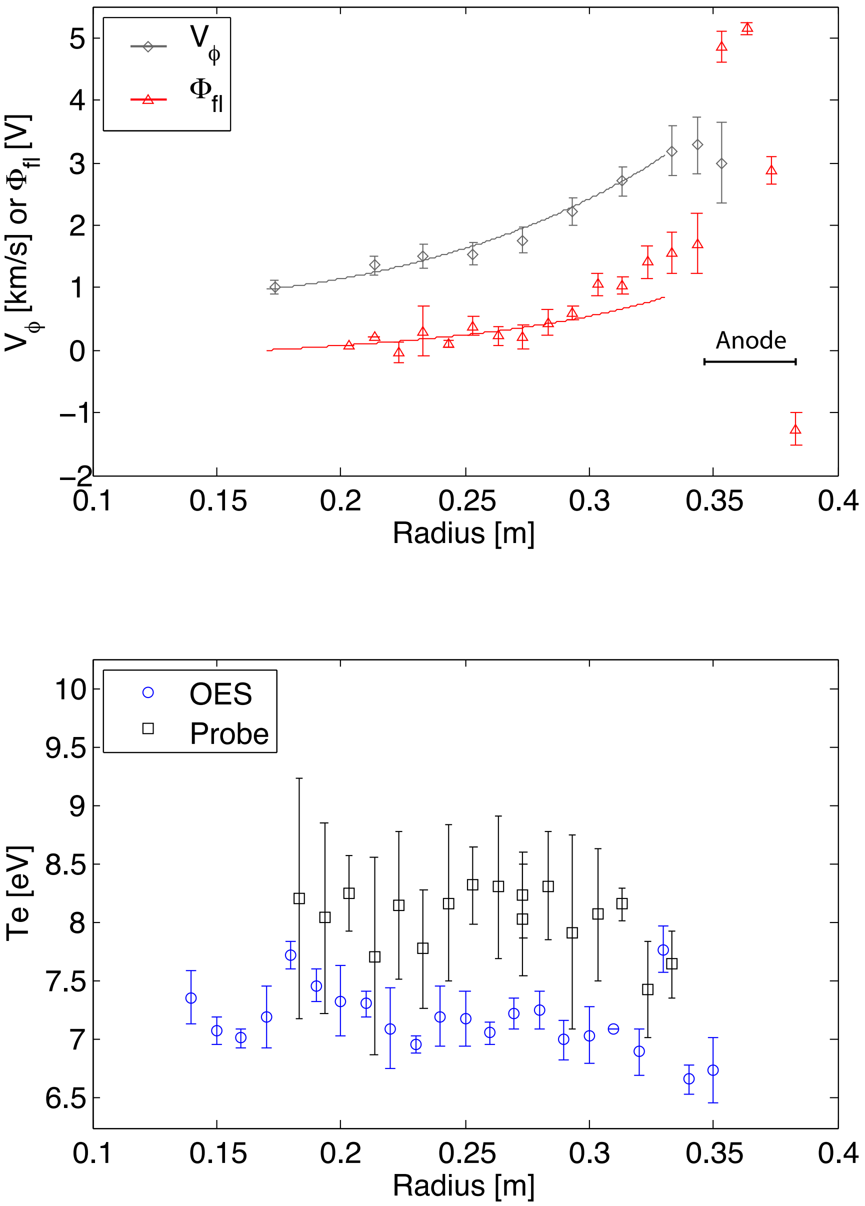

Figure 4.6: Top) Fitted flow and floating potential measurements in argon plasma ($T_e = 8.5$ eV, $T_i = 0.1$ eV, $n = 1.5 \times 10^{10}$ cm^{-3}). The midplane anode is located in the magnetized edge region, $r = 0.36$ m. Bottom) Temperature profiles measured by the swept Langmuir probe and Optical Emission Spectroscopy suggest uniform temperature in the bulk, unmagnetized region. OES profiles have not been Abel inverted.

by Earth's magnetic field, where $\rho_e \sim 0.1$ m for 0.5 Gauss.) While mean free paths are long, charged particles do not immediately escape and instead undergo multiple bounces, or reflections by the mirror force at the cusps. The confinement time is long enough to allow collisions to occur, therefore the bulk particle distribution can be expected to reach a Maxwellian distribution, further justifying the use of Eq. 4.17.

Radial temperature profile measurements do indicate uniform electron temperatures in the bulk, unmagnetized region in both rotating and non-rotating plasmas. In Fig. 4.7, electron temperature was measured in a flowing argon plasma with both a radially scanned, swept Langmuir probe (Section 2.6.2) and Optical Emission Spectroscopy (Section 2.6.5). In this data, a steady flow of neutral gas was applied so that plasma parameters and flow were constant in time throughout the plasma pulse. Each Langmuir probe data point is a time average of multiple measurements throughout the plasma pulse, and error bars are standard error of the mean. The fixed triple probe was also used to monitor shot to shot variation and indicated that plasma parameters were constant as the probe was scanned (i.e. the probe did not perturb the plasma).

To obtain OES data, the optical table was scanned in a random pattern to acquire multiple plasma pulses at each radial position. Spectra was taken with 200 ms integration time every 0.35 sec. Each OES data point was time averaged for each plasma pulse, and then ensemble averaged over the multiple pulses. Error bars are standard error of the ensemble average. The OES temperature analysis may have been affected by an anomaly in the emission intensity which was observed at the radial positions between $r = 17$ cm and $r = 20$ cm, probably due to reflections inside the chamber. Furthermore, an Abel inversion routine should be implemented in order to obtain the local emission profile from the line-integrated emission. Nonetheless, it seems that the the OES temperature measurements are in agreement with the Langmuir probe temperature measurements (within 15%), which is important for determining the magnitude of the Mach probe velocity and accompanying rotation-induced rise in radial potential.

Measurements of the radial floating potential indeed show the presence of an outward rising potential (or inward pointing radial electric field) which only arises when the plasma is flowing. The velocity and corresponding floating potential measurements in helium, neon, and argon are shown in Fig. 4.7. The Mach probe velocity measurements are fitted with the Bessel function model (Eq.4.3) based on the the measured plasma parameters for each dataset, some of which are listed in Table 3.1. The floating potential measurements are fitted with the predicted potential according to Eq. 4.19, where the velocity profile is the Bessel function fit of the Mach probe velocity data.

The evolution of the floating potential profiles was studied in various gases. In the neon and argon experiments, flow was induced exclusively by the outer cathodes. In the helium experiment, flow was created at both the inner and outer boundaries.The helium and neon discharges used a neutral gas puff, so that the flow velocity increased as the neutral gas was pumped out. Measurements shown in Fig. 4.7 are for two different times during the same plasma pulse. The argon profiles were created with a steady flow of neutral gas and were measured on separate days with different applied bias to the stirring electrodes (in Shot 656, each outer cathode was 500 V, 3 A and in Shot 650 each cathode was 350 V, 1.1 A). In all cases, as the flow velocity increases, the radial floating potential increases as expected.

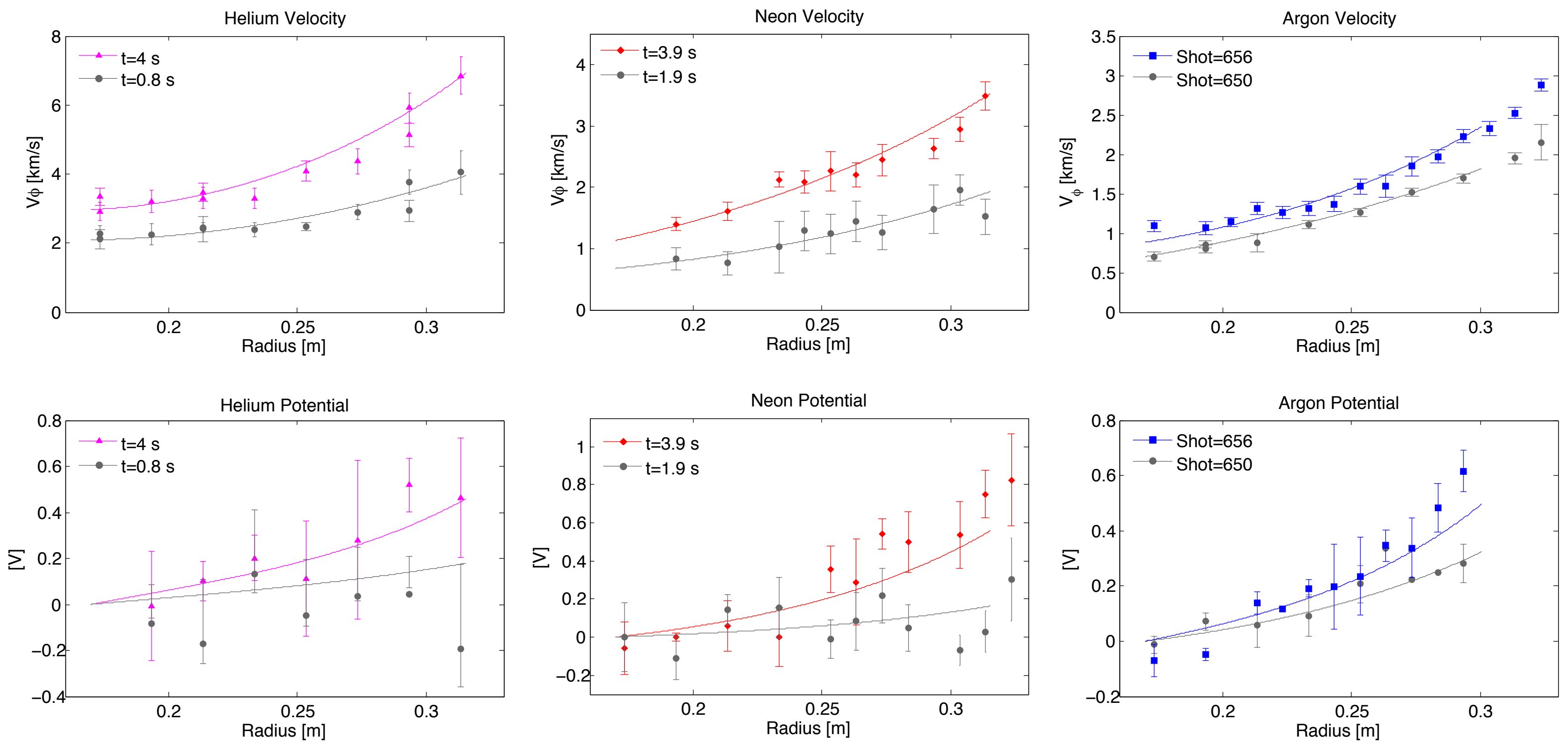

Figure 4.7: Floating potential profiles are measured for various flow profiles generated in helium, neon, and argon. As the flow velocity increases, the radial floating potential increases as predicted by Eq. 4.19.

4.3.2 Density Stratification

Rapidly rotating plasmas with density stratification could be used to study the Parker instability, a magnetic buoyancy instability which may play a role in certain astrophysical situations, such as in the rise of magnetic flux tubes through the Sun's surface. An analysis of the Parker instability in the PCX device has been done [73]. It was found that although a relatively small equilibrium magnetic field is needed for the onset of the instability, large Mach numbers ($M = V_0/C_s > 5$) are required to overcome the stabilizing effect of the Coriolis force. This likely won't be achievable unless fully ionized plasmas can be created in order to exceed the critical ionization velocity limit imposed in partially ionized plasmas (Section 3.5.1).

According to Fig. 4.7, the measured radial increase in potential is not much more than 0.8 V, so the density displacement would be expected to be within $10-20\%$ of the core density, according to $n_e/n_o = \exp(e\Phi/T_e)$. Clear indications of density variation have not yet been observed, because the interpretation of probe measurements based on collection of ion saturation current in a rotating plasma were unclear, and shot-to-shot variation in the measurement also tends to be on the order of $10 - 20\%$.

4.3.3 Mass Dependence

A spinning plasma device has other interesting applications, for example, as a plasma centrifuge to separate ions (even nuclear isotopes) by mass. Plasma centrifuges have been proposed and built by a number of authors before [36, 37, 74, 75, 76], but confinement has always relied on large magnetic fields throughout the plasma volume. One particular advantage of a device like PCX is that the magnetic field only needs to be large at the edge. The magnetic field can be provided by permanent magnets, potentially offering significant cost reduction since no power is required to maintain the field.

Centrifuge experiments were attempted in PCX, where discharges of spinning plasma were created using a combination of a puff of helium gas and a steady flow of argon gas, or vice versa. Spectra was obtained at various radial positions with the scanning the optics table, and preliminary analysis involved examining the ratio of helium to argon ion line intensities as a function of radius.

The analysis was ill-posed because the weak helium ion line at 468.5 nm poorly resolved and near a strong helium neutral line at 471.3 nm. Evidence of mass separation in a helium-argon plasma remains elusive.

The best evidence for mass-dependent, outward displacement of spinning plasma in PCX is found by comparing the profiles for flow and potential of various gases. One can solve for the ion mass using the measured potential and fitted velocity profiles:

$$M_i = \frac{e\Phi(r)(Z + \frac{T_i}{T_e})}{\int_{R_1}^{R_2} \frac{V_\phi(r)^2}{r} dr} \tag{4.20}$$

In Fig. 4.8, four different gases (helium, neon, argon, and xenon) were rotated. Since the centrifugal force is stronger on heavier ions, lower rotation speeds are required to obtain radial potentials which are equivalent to the faster rotating, lighter species. Furthermore, the measured values of potentials and velocity result in derived ion masses which are close to the expected values.

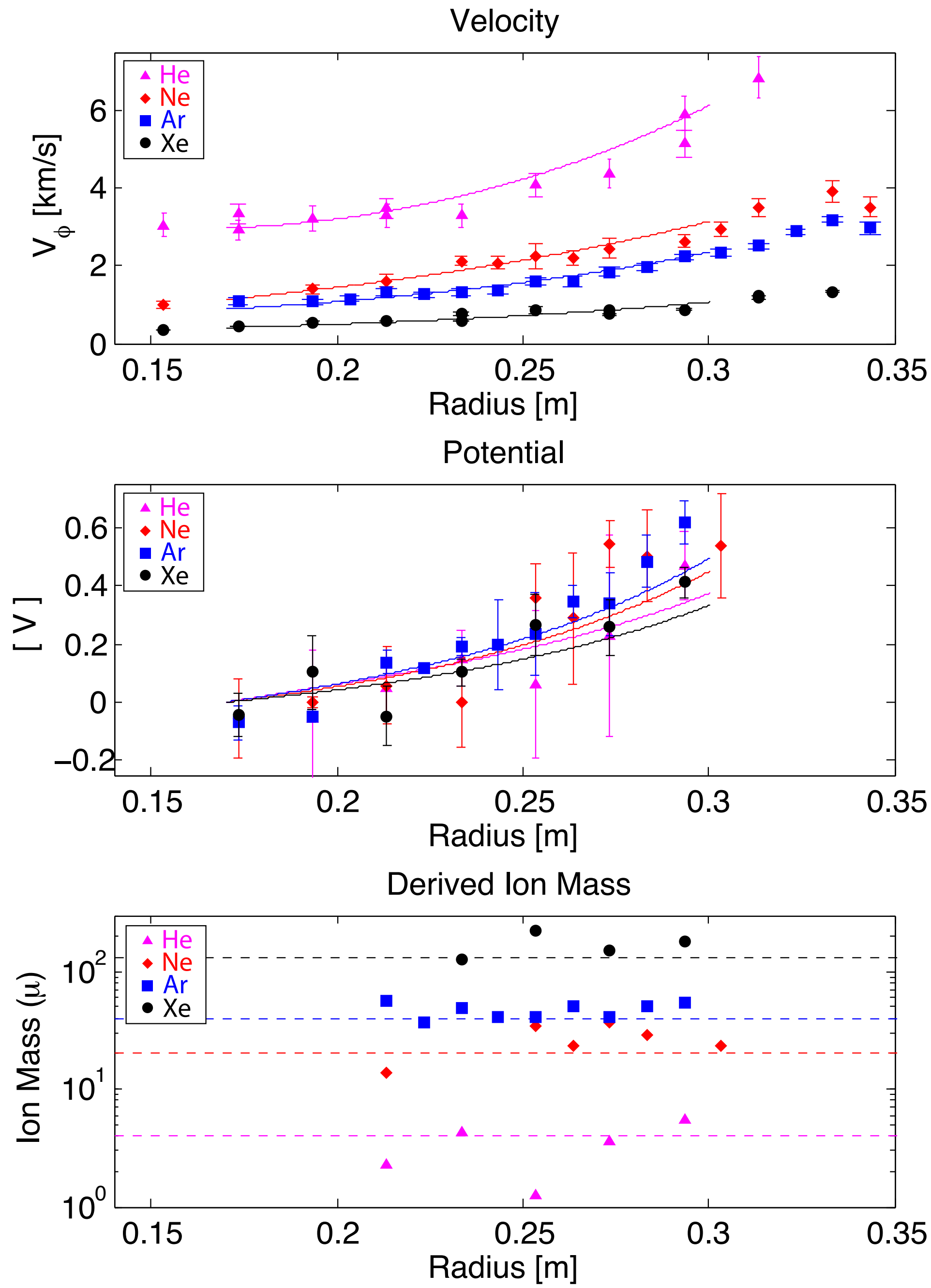

Figure 4.8: The measured values of velocity and potentials in four different gases (helium, neon, argon, and xenon) result in derived ion masses (based on Eq. 4.20 with Z=1) which are close to the expected values (dashed lines).

Chapter 5

Stability of a Couette Flow of Plasma

The primary success of this thesis work has been the demonstration of a new concept for spinning unmagnetized plasma in the laboratory. The ability to produce a hot, fast flowing, magnetic field-free plasma is a major advance towards creating the conditions necessary to study a wide variety of flow-driven instability phenomenon relevant to plasma astrophysics.

In PCX, plasma flow can be driven by electrostatic stirring assemblies at both the inner and outer boundaries. This type of circular fluid flow between two concentric cylinders is well-known in fluid dynamics as Couette flow (or Taylor-Couette flow). Couette flow has been studied in extraordinary detail, both experimentally and theoretically, beginning with Couette himself in 1890, who calculated the viscosity of water by rotating an outer cylinder and measuring the torque induced on an inner, stationary cylinder. In the last several decades, Couette flow has received much attention from the astrophysics community, because Couette flow profiles $(\Omega(r) = C + D/r^2)$ can be adjusted so that the angular velocity decreases with radius and the angular momentum increases with radius, and thus mimic the Keplerian-like flows of accretion disks (where $\Omega(r) = \sqrt{GM/r^3}$). Keplerian flows of conducting fluids are considered hydrodynamically stable because they satisfy the Rayleigh stability criterion, but these flows can be destabilized by a magnetic field through the action of the magnetorotational instability (MRI) [12].

The PCX device is the first ever steady-state, Couette flow of weakly magnetized plasma. The goal of the experiment is to study the MRI in a plasma, ideally by first creating a hydrodynamically stable, Keplerian-like flow of plasma, and then destabilizing the MRI by applying a vertical seed field. Interestingly, there may also be an opportunity to explore a "Taylor-Couette dynamo". It is known that Couette flow, with rotation driven exclusively at the inner boundary, can become hydrodynamically unstable and exhibit large scale, secondary flows in the form of axisymmetric vortices. It has been suggested that the Taylor vortex velocity field, in combination with a small magnetic seed field, could generate magnetic energy through dynamo action [77].

The next step is to explore the stability analysis in the context of the experimental geometry and achievable parameters. This chapter begins by considering the hydrodynamic stability of the unmagnetized Couette flow of plasma, including the drag due to ion-neutral charge exchange collisions. A marginal stability analysis of the linearized system is used to estimate the conditions required for onset of Taylor vortex flow. Exploring this threshold is important, since Taylor vortices are secondary flows that transport momentum between the inner and outer cylinders and are similar to the expected velocity structures expected to appear in the saturated state of the MRI. Next, the system is examined with the addition of an axial magnetic field using a local perturbation analysis of the linearized, dissipative, incompressible magnetohydrodynamics equations, including the Hall and ion-neutral drag effects.

5.1 Hydrodynamic Stability

5.1.1 The Centrifugal Instability

Most of the flow profiles studied in Chapter 4 were driven exclusively at the outer cylinder boundary, essentially creating solid body rotation which resembles a centrifuge. Such profiles are hydrodynamically stable because the angular momentum increases with radius, and the outward centrifugal force is balanced by the inward pressure gradient force. If instead only the inner cylinder is rotating and the outer cylinder is kept fixed, the system can become centrifugally unstable in accordance with Rayleighs criterion, which states that instability occurs in inviscid, axisymmetric flows if $\frac{d}{dr}(r^2\Omega) < 0$. In this state, if a fluid element is perturbed outward, it carries along its initial angular momentum, but the local pressure gradient force at the larger radius is less than the centrifugal force on the fluid element, so the fluid element continues to move radially outward.

In the resulting centrifugally unstable Couette equilibrium, the eigenmodes appear as a column of axisymmetric "Taylor" vortices, first studied in detail by G.I. Taylor in 1923 (see Fig. 5.1).

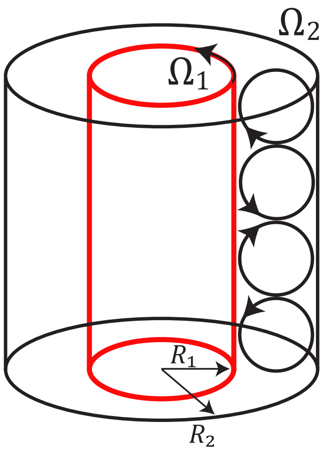

Figure 5.1: In this sketch, the inner and outer radii are denoted by R_1 and R_2. Likewise, the inner and outer angular frequencies are Ω_1 and Ω_2. If only the inner cylinder is rotating, an inviscid fluid is centrifugally unstable, forming steady, axisymmetric Taylor vortices periodic in z.

Taylor's numerical computations were in excellent agreement with his own experimental measurements, which showed that the speed of the inner cylinder must exceed a certain critical value before the secondary vortex flow appeared, and this threshold depends on the viscosity of the fluid (see Fig. D.1 for his original stability diagram). If the rotation rate of the inner cylinder is further increased, the Taylor-vortex flow becomes unstable to non-axisymmetric perturbations, eventually reaching a state of turbulence. Since Taylor's groundbreaking study, a large number of distinct flow states, which depend on the rotation rates of the inner and outer cylinders, have been documented in many experiments and have acquired a standard naming convention, which has rather famously been indexed by Andereck et al. in [78].

5.1.2 The Influence of Boundary Conditions

It is well known that in Taylor-Couette experiments, the top and bottom endcaps can significantly influence the bulk behavior of the flow. When the endcaps are either fixed or rotating at angular velocities different than the bulk flow, an imbalance in the pressure gradient and centrifugal forces creates radial boundary layer flow that can drive large-scale Ekman vortices. Ekman circulation can affect the onset of global instabilities, and this can depend on whether the endwalls are fixed, rotating, or stress-free [79]. In practice, the effects of the endcaps can be minimized by using large aspect ratios, where the height is large compared to the gap between the cylinders. Computations often assume infinitely long cylinders and use periodic boundary conditions.

In the Princeton MRI experiment where $\Gamma = h/(R_2 - R_1) = 2.1$, Ekman effects are minimized using differentially rotating split ring endcaps. The aspect ratio of PCX is also small, with $\Gamma \sim< 3$ (which arguably depends on the number of rotation electrodes used on the inner boundary). However, the PCX endcap boundary conditions are complicated by the alternating cusp magnetic field and corresponding field dependent flows. A no-slip boundary condition most likely does not hold, and flows associated with Ekman circulation could very well be minimal.

5.1.3 Hydrodynamic Stability Analysis

We begin by formulating the classic fluid stability problem of Taylor-Couette flow using the variational methods as outlined in Chapter 7 of Chandrasekhar (1961) [80], except with the inclusion of the plasma-specific ion-neutral drag term. In the unmagnetized bulk region, the toroidal force balance is given by

$$\frac{\partial \mathbf{V}}{\partial t} + (\mathbf{V} \cdot \nabla)\mathbf{V} = -\frac{\nabla P}{\rho} - \frac{\mathbf{V}}{\tau_{i0}} + \nu \nabla^2 \mathbf{V} \tag{5.1}$$

where ν is viscosity due to ion-ion collisions and $\tau_{i0} \approx (n_0 \langle \sigma_{cx} v \rangle)^{-1}$ is the ion-neutral collision time; σ_{cx} is the charge-exchange cross-section, as given in Section 4.1.

Assuming axisymmetry with a perturbed flow $\mathbf{V} + \mathbf{u} = [u_r, V_0 + u_\theta, u_z]$ and $\bar{\omega} = \frac{\delta P}{\rho}$, the linearized momentum equation is:

$$\frac{\partial u_r}{\partial t} - 2\frac{V_0 u_\theta}{r} = -\frac{\partial \bar{\omega}}{\partial r} - \frac{u_r}{\tau_{i0}} + \nu(\nabla^2 u_r - \frac{u_r}{r^2}) \tag{5.2}$$

$$\frac{\partial u_\theta}{\partial t} + \left(\frac{V_0}{r} + \frac{\partial V_0}{\partial r}\right) u_r = -\frac{u_\theta}{\tau_{in}} + \nu \nabla^2 u_\theta \tag{5.3}$$

$$\frac{\partial u_z}{\partial t} = -\frac{\partial \bar{\omega}}{\partial z} - \frac{u_z}{\tau_{in}} + \nu \nabla^2 u_z \tag{5.4}$$

Here, the base flow V_0 is the equilibrium ion-neutral damped plasma Couette flow profile given by Eq. 4.3. Suppose the system is periodic in the z-direction and perturbations are of the form:

$$\begin{aligned} u_r &= e^{\gamma t} u(r) \mathrm{cos}(kz) && (5.5) \\ u_\theta &= e^{\gamma t} v(r) \mathrm{cos}(kz) && (5.6) \\ u_z &= e^{\gamma t} w(r) \mathrm{sin}(kz) && (5.7) \\ \bar{\omega} &= e^{\gamma t} \bar{\omega}(r) \mathrm{cos}(kz) && (5.8) \end{aligned}$$

These vortex-shaped perturbations feature sinusoidal variation in the z-direction with periodicity described by the axial wavenumber k, a growth rate γ, and perturbation amplitudes which depend on the radial position.

Substituting these perturbations into the linearized momentum equations (Eq. 5.4) leads to:

$$\nu \left[\frac{d^2 u}{dr^2} + \frac{1}{r}\frac{du}{dr} - \left(\frac{1}{r^2} + k^2 + \frac{1}{\tau_{i0}\nu} + \frac{\gamma}{\nu} \right) u \right] + \frac{2V_0 v}{r} = \frac{d\bar{\omega}}{dr} \tag{5.9}$$

$$\nu \left[\frac{d^2 v}{dr^2} + \frac{1}{r}\frac{dv}{dr} - \left(\frac{1}{r^2} + k^2 + \frac{1}{\tau_{i0}\nu} + \frac{\gamma}{\nu} \right) v \right] - \left(\frac{dV_0}{dr} + \frac{V_0}{r} \right) u = 0 \tag{5.10}$$

$$\nu \left[\frac{d^2 w}{dr^2} + \frac{1}{r}\frac{dw}{dr} - \left(k^2 + \frac{1}{\tau_{i0}\nu} + \frac{\gamma}{\nu} \right) w \right] = -k\bar{\omega} \tag{5.11}$$

Additionally, an incompressible flow where $\nabla \cdot \mathbf{V} = 0$ says that:

$$\frac{du}{dr} + \frac{u}{r} + kw = 0 \tag{5.12}$$

Finally, using the notation $\frac{d}{dr} \rightarrow D$ and $\frac{d}{dr} + \frac{1}{r} \rightarrow D_*$, the equations can be written as:

$$\nu \left[DD_* - (k^2 + \frac{1}{\tau_{i0}\nu} + \frac{\gamma}{\nu} \right] u + \frac{2V_0 v}{r} = \frac{d\bar{\omega}}{dr} \tag{5.13}$$

$$\nu \left[DD_* - \left(k^2 + \frac{1}{\tau_{i0}\nu} + \frac{\gamma}{\nu} \right) \right] v - (D_* V_0)\, u = 0 \tag{5.14}$$

$$\frac{\nu}{k^2} \left[D_* D - \left(k^2 + \frac{1}{\tau_{i0}\nu} + \frac{\gamma}{\nu} \right) \right] D_* u = \bar{\omega} \tag{5.15}$$

These equations can be combined and neatly written as:

$$\frac{\nu}{k^2} \left[DD_* - \left(k^2 + \frac{1}{\tau_{i0}\nu} + \frac{\gamma}{\nu} \right) \right] \left(DD_* - k^2 \right) u = \frac{2V_0}{r} v \tag{5.16}$$

$$\nu \left[DD_* - \left(k^2 + \frac{1}{\tau_{i0}\nu} + \frac{\gamma}{\nu} \right) \right] v = (D_* V_0) u \tag{5.17}$$

As shown in Appendix D, these equations can be discretized and transformed into an eigenvalue problem at marginal stability (where $\gamma = 0$),which can then be solved in MATLAB. The calculation uses a specified value for the momentum diffusion length parameter, $L_v = \sqrt{\tau_{i0}\nu}$ (as defined in Eq. 4.5) and assumes the axial wavenumber $k = \pi/(R_2 - R_1)$ with PCX dimensions $R_1 = 0.13$ m and $R_2 = 0.3$ m. The eigenvalue solver then finds the critical Reynold's number at the inner boundary ($Re_1 = V_1 L/\nu$) for each prescribed Re_2. The results of the marginal stability analysis are shown in Fig. 5.2. Stability curves for several values of L_v are plotted in the parameter space of dimensionless fluid Reynold's numbers of the inner and outer cylinders (Re_1, Re_2). At large values of L_v, ion-neutral collisions are unimportant, and the azimuthal velocity profile takes on the classical form for Taylor-Couette flow of a viscous fluid. In this limit, the minimum critical Re_1 is determined by viscosity, and the stability curve asymptotes to Rayleigh's prediction for stability of inviscid fluid ($\Omega_1 R_1^2 = \Omega_2 R_2^2$), which is plotted as a dashed line in Fig. 5.2.

As L_v decreases, ion-neutral collisions become more important, and the flow becomes unstable in regions which would otherwise be Rayleigh stable. Presumably, this is in part due to the increased shear in the velocity profile created by momentum loss in ion-neutral collisions. In Fig. 5.3, profiles of flow and $d(r^2\Omega)/dr$ are plotted for various neutral gas pressures ($2 \times 10^{-7} - 3 \times 10^{-5}$ Torr), which correspond to different values of L_v. These profiles are with $Re_1 = 800$ and $Re_2 = 300$ (marked by the star in the stability diagram Fig. 5.2), and velocity is calculated based on fixed helium parameters $n = 3 \times 10^{10}$ cm^{-3}, $T_e = 8$ eV, and $T_i = 0.1$ eV. It seems that instability can occur in regions where $d(r^2\Omega)/dr < 0$ and the centrifugal acceleration of perturbed fluid can overcome viscous damping.

Historically, this linear stability analysis accurately predicts the critical velocity for Taylor vortices, at least in the case of large aspect ratio, purely viscous Couette flow experiments. This analysis might also hold for plasma flows in PCX, especially since the unique multicusp boundary conditions at the top and bottom endcaps could minimize Ekman circulation which might otherwise influence the global stability. Measurements of the onset of Taylor vortices in the experiment may prove challenging, since the axial and radial velocities of the vortices are typically only a few percent of V_1, which would likely be in the error bars for Mach probes. It would be interesting

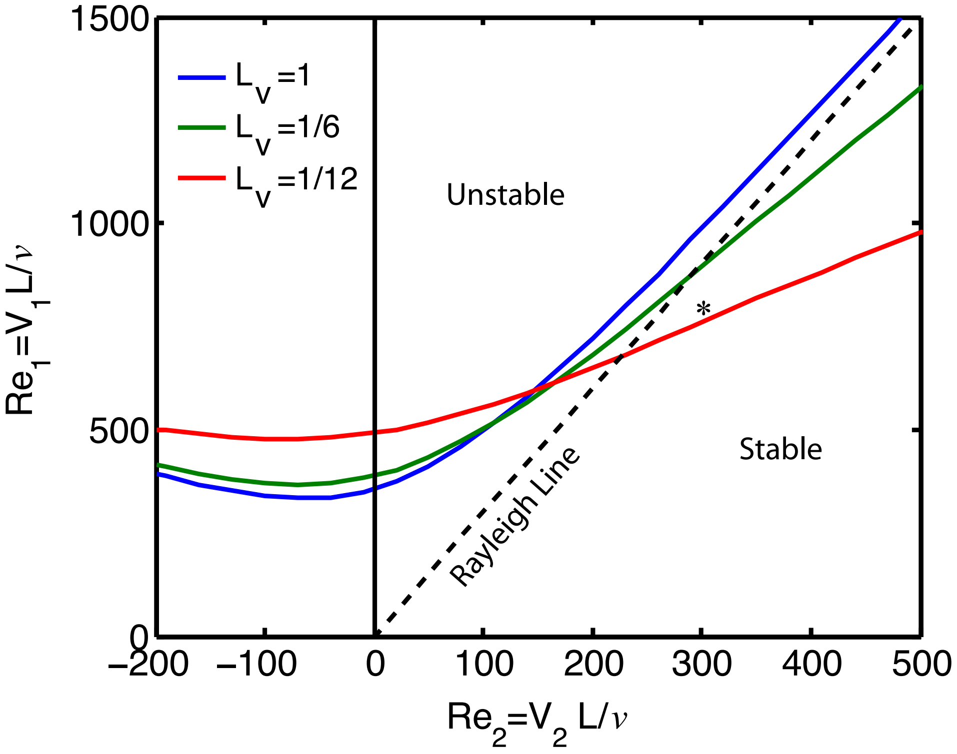

Figure 5.2: Marginal stability diagram for Taylor Couette flow. As the momentum diffusion length decreases, flow becomes unstable in regions which would otherwise be Rayleigh stable.

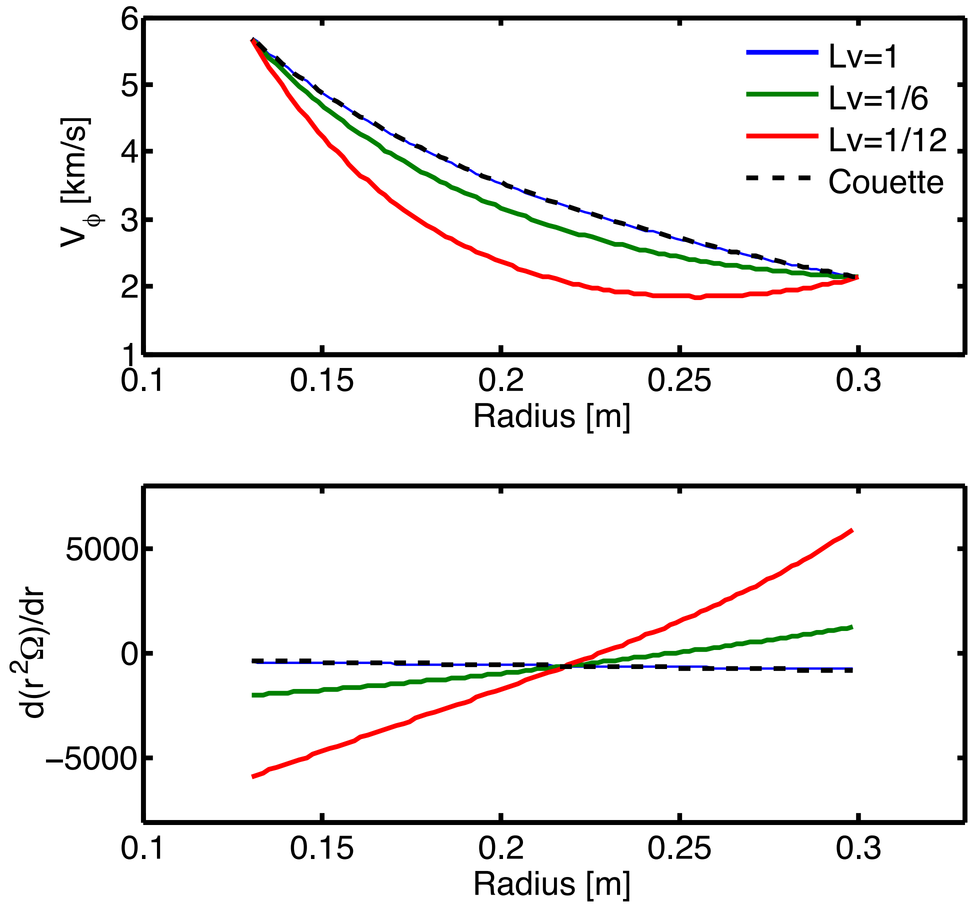

Figure 5.3: Top) Representative flow profiles for various momentum diffusion lengths with $Re_1 = 800$ and $Re_2 = 300$. Bottom) Corresponding calculation of $d(r^2\Omega)/dr$. Flows can be unstable in regions where perturbations are not damped out by viscosity and $d(r^2\Omega)/dr < 0$.

to compute mode structures and amplitudes with global simulations which incorporate ion-neutral damping.

5.2 Magnetohydrodynamic Stability

While the observation of hydrodynamic instabilities such as Taylor-vortex flow in a plasma would be in itself an interesting contribution to an already rich history of Couette flow studies, the primary motivation for PCX is to study the MRI in a plasma. In the case of the standard MRI, an otherwise hydrodynamically stable, differentially rotating, conducting disk with $\frac{d}{dr}(r^2\Omega) > 0$ and $\frac{d\Omega}{dr} < 0$ should be destabilized by an applied, vertical magnetic seed field. In PCX, it may be possible to experimentally identify effects beyond ideal MHD in MRI theory. In particular, two-fluid effects involving the Hall term and plasma-neutral interactions are expected to be important.

The Hall effect could play a role in protostellar and protoplanetary disks, which are typically cold and have regions with very low ionization fractions. The Hall effect can arise when ions collide with neutrals and become decoupled from the magnetic field, while the electrons remain frozen-in to the field. The linear stability of the MRI with the inclusion of the Hall term was first studied by Wardle [22] and then more generally by Balbus & Terquem [23]. It was found that the Hall term changes the behavior of the MRI significantly; positive growth rate occurs only when the magnetic field is antiparallel to the rotation axis.

Low ionization can also give rise to ambipolar diffusion, where the neutrals can become coupled to the magnetic field through collisions (elastic, ionization, recombination) with ions. The linear growth of the MRI in weakly ionized, weakly magnetized shear flows in the ambipolar limit was first examined by Blaes & Balbus [81]. They found that the MRI is damped if the ion-neutral collision frequency is smaller than the orbital frequency (when the ion-neutral coupling is poor). In PCX, the neutral gas is a stationary, uniform background which behaves independently of the ions. This is in contrast to an accretion disk, where both neutrals and ions are in orbit together. When charge exchange occurs in the experiment, the mean free path for the resulting neutral is large, and the neutral escapes the experiment before being ionized. Thus, the neutrals are not coupled to the ions, and ion-neutral collisions simply represent a momentum sink which can be included through a charge-exchange drag term in the momentum equation. Therefore, in the experiment, it might be expected that an increase in ion-neutral collision frequency would interrupt and suppress the growth of the MRI and possibly act to dampen the MRI driven turbulent transport.

Resistivity and kinematic viscosity should also be considered, which can both reduce the growth rate of unstable modes [4]. At the linear growth stage, viscosity can suppress growth of unstable modes and change the wavelength of the fastest growing mode. Resistivity suppresses unstable wavelengths when the resistive diffusion time becomes comparable to the growth rate and is especially important at very weak magnetic fields.

Both linear and nonlinear global computations have been performed in the past by Ebrahimi (2011) [27] using the geometry and expected plasma parameters for the PCX experiment and assuming Keplerian flow profiles. However, the actual measured plasma density obtained in the experiment is at least an order of magnitude lower than that used in [27], and the flow profiles are strongly shaped by the ion-neutral damping, leading to increased shear. The goal of this section, then, is to develop the appropriate local dispersion relation for the MRI in the PCX by considering that the plasma is only partially ionized. One question is, does increased shear in the velocity profiles make it easier to excite the MRI, or does ion-neutral damping end up suppressing the instability?

The local analysis performed here is not rigorous and is meant to give a rough estimate for stability. Of course, a global analysis is needed to calculate the exact mode structure and amplitude during linear growth. Ultimately, diagnosing the nonlinear, saturated state of MRI and associated momentum transport will require careful measurements of changes in the steady-state toroidal velocity profile, as well as the Reynolds and Maxwell stresses due to fluctuations in velocity and magnetic field components. It is encouraging that there is reasonable qualitative agreement between the local Hall-MHD approximation and the global simulations in [27], so the local analysis here may nonetheless be a useful guide.

5.2.1 Governing Equations

We begin by considering a fluid in which the ions and electrons have different velocities. If $\mathbf{V}_{\mathrm{i}} = \mathbf{V}$, and $\mathbf{J} = e(n_{\mathrm{i}}\mathbf{V}_{\mathrm{i}} - n_{\mathrm{e}}\mathbf{V}_{\mathrm{e}})$, then

$$\mathbf{V}_{\mathrm{e}} = \mathbf{V} - \frac{\mathbf{J}}{ne} \tag{5.18}$$

Ohm's law becomes

$$\mathbf{E} + \mathbf{V} \times \mathbf{B} = \eta \mathbf{J} + \frac{1}{ne}\mathbf{J} \times \mathbf{B} \tag{5.19}$$

where η is magnetic diffusivity, and we have ignored the terms involving anisotropic electron pressure, ambipolar diffusion, and the time variation of current from electron inertia. The evolution of the magnetic field is determined by the induction equation, which becomes

$$-\frac{\partial \mathbf{B}}{\partial t} = \nabla \times \mathbf{E} \tag{5.20}$$

$$= \nabla \times \left[\mathbf{V} \times \mathbf{B} - \eta(\nabla \times \mathbf{B}) - \frac{(\nabla \times \mathbf{B}) \times \mathbf{B}}{\mu_0 ne} \right], \tag{5.21}$$

where η is magnetic diffusivity. The last term represents the two-fluid Hall term, which notably has introduced an anti-symmetry that leads to a directional dependence of magnetic field.

The momentum equation is

$$\frac{\partial \mathbf{V}}{\partial t} + (\mathbf{V} \cdot \nabla)\,\mathbf{V} = \frac{(\mathbf{B} \cdot \nabla)\mathbf{B}}{\mu_o \rho} - \frac{1}{\rho}\nabla(p + \frac{B^2}{2\mu_o}) + \nu \nabla^2 \mathbf{V} - \frac{\mathbf{V}}{\tau_{in}}, \tag{5.22}$$

where ν is viscosity due to ion-ion collisions and $\tau_{i0} \approx (n_0 \langle \sigma_{cx} v \rangle)^{-1}$ is the ion-neutral collision time; σ_{cx} is the charge-exchange cross-section. It is assumed that ions lose momentum to a uniform and stationary background of neutrals. In addition, the incompressible and divergence free conditions lead to:

$$0 = \nabla \cdot \mathbf{V} \tag{5.23}$$

$$0 = \nabla \cdot \mathbf{B} \tag{5.24}$$

5.2.2 Linear Dispersion Relation

Assuming axisymmetric flow with perturbations $\mathbf{B} = B_0\hat{z} + \mathbf{b}$ and $\mathbf{V} = V_0\hat{\theta} + \mathbf{v}$, the linearized force balance equation becomes:

$$\hat{r}: \quad \frac{\partial v_r}{\partial t} - 2\frac{V_0 v_\theta}{r} = \frac{V_A^2}{B_0}\frac{\partial b_r}{\partial z} - \frac{1}{\rho_0}\frac{\partial p}{\partial r} - \frac{V_A^2}{B_0}\frac{\partial b_z}{\partial r} + \nu\nabla^2 v_r - \frac{v_r}{\tau_{in}} \tag{5.25}$$

$$\hat{\theta}: \quad \frac{\partial v_\theta}{\partial t} + \left(\frac{V_0 v_r}{r} + v_r\frac{\partial V_0}{\partial r}\right) = \frac{V_A^2}{B_0}\frac{\partial b_\theta}{\partial z} + \nu\nabla^2 v_\theta - \frac{v_\theta}{\tau_{in}} \tag{5.26}$$

$$\hat{z}: \quad \frac{\partial v_z}{\partial t} = -\frac{1}{\rho_0}\frac{\partial p}{\partial z} + \nu\nabla^2 v_z - \frac{v_z}{\tau_{in}} \tag{5.27}$$

where $V_A = \frac{B_0}{\sqrt{\rho_0\mu_0}}$. The linearized diffusion equation results in

$$\hat{r}: \quad \frac{\partial b_r}{\partial t} = B_0\frac{\partial v_r}{\partial z} + \eta\left(\frac{\partial^2 v_r}{\partial r^2} + \frac{\partial^2 v_r}{\partial z^2}\right) + \frac{B_0}{\mu_0 ne}\frac{\partial^2 b_\theta}{\partial z^2} \tag{5.28}$$

$$\hat{\theta}: \quad \frac{\partial b_\theta}{\partial t} = b_r\frac{\partial \Omega}{\partial lnr} + B_0\frac{\partial v_\theta}{\partial z} + \eta\left(\frac{\partial^2 v_\theta}{\partial r^2} + \frac{\partial^2 v_\theta}{\partial z^2}\right) - \frac{B_0}{\mu_0 ne}\left(B_0\frac{\partial^2 b_r}{\partial z^2} - \frac{\partial}{\partial r}\frac{\partial b_z}{\partial z}\right) \tag{5.29}$$

$$\hat{z}: \quad \frac{\partial b_z}{\partial t} = B_0\frac{\partial v_z}{\partial z} + \eta\left(\frac{\partial^2 v_z}{\partial r^2} + \frac{\partial^2 v_z}{\partial z^2}\right) - \frac{B_0}{\mu_0 ne}\frac{\partial}{\partial r}\frac{\partial b_\theta}{\partial z} \tag{5.30}$$

where $\eta = 1.03 \times 10^{-4}\Lambda T_e^{-1.5}/\mu_0$ [m^2/s] is the magnetic diffusivity (with the Coulomb logarithm given in Eq. 3.7) and $\Omega = V_0/r$.

Consider now the Wentzel-Kramers-Brillouin (WKB) analysis method, which assumes that the amplitudes and gradients of the primary background state do not change under infinitesimal perturbations, and that the perturbation scale is much smaller than the scale of the system. The perturbation takes the form of $\mathbf{q} = \tilde{\mathbf{q}}e^{(\gamma t - (ik_r r + ik_z z))}$. If the growth rate, γ, is real and positive, the amplitude of the instability will grow, and if γ is imaginary, the motion is purely oscillatatory. The linearized equations become

$$k_r v_r + k_z v_z = 0 \tag{5.31}$$

$$k_r b_r + k_z b_z = 0 \tag{5.32}$$

$$\gamma v_r - 2\Omega v_\theta = -ik_z V_A^2 \frac{b_r}{B_0} + ik_r \frac{p}{\rho_0} + ik_r V_A^2 \frac{b_z}{B_0} - k^2 \nu v_r - \frac{v_r}{\tau_{in}} \tag{5.33}$$

$$\gamma v_\theta + \kappa^2 \frac{v_r}{2\Omega} = -ik_z V_A^2 \frac{b_\theta}{B_0} - k^2 \nu v_\theta - \frac{v_\theta}{\tau_{in}} \tag{5.34}$$

$$\gamma v_z = ik_z \frac{p}{\rho_0} - \nu k^2 v_z - \frac{v_z}{\tau_{in}} \tag{5.35}$$

$$\gamma b_r = -iB_0 k_z v_r - \eta k^2 b_r - k_z^2 \frac{B_0}{\mu_0 ne} b_\theta \tag{5.36}$$

$$\gamma b_\theta = b_r \frac{\partial \Omega}{\partial \ln r} - iB_0 k_z v_\theta - \eta k^2 b_\theta + k_z^2 \frac{B_0}{\mu_0 ne} b_r - k_z k_r \frac{B_0}{\mu_0 ne} b_z \tag{5.37}$$

After eliminating the z-components, these equations reduce to the eigenvalue problem $(A - \gamma I)\mathbf{x} = 0$, where the eigenvector is $\mathbf{x} = [b_r b_\theta v_r v_\theta]$. The characteristic equation is determined by:

$$\det \begin{vmatrix} -\eta k^2 - \gamma & -\frac{B_0}{\mu_0 ne} k_z^2 & -iB_0 k_z & 0 \\ \frac{\partial \Omega}{\partial \ln r} + \frac{B_0}{\mu_0 ne} k^2 & -\eta k^2 - \gamma & 0 & -k_z B_0 \\ \frac{ik_z V_A^2}{B_0} & 0 & -\nu k^2 - \tau_{in}^{-1} - \gamma & \frac{2\Omega k_z^2}{k^2} \\ 0 & -\frac{ik_z V_A^2}{B_0} & -\frac{\kappa^2}{2\Omega} & -\nu k^2 - \tau_{in}^{-1} - \gamma \end{vmatrix} = 0 \tag{5.38}$$

where the epicyclic frequency is $\kappa = 4\Omega^2 + \partial \Omega^2 / \partial \ln r$. The resulting dispersion relation is

$$\begin{aligned} &\left[(\gamma + \eta k^2)(\gamma + \nu k^2 + \tau_{i0}^{-1}) + (k_z V_A)^2\right]^2 \frac{k^2}{k_z^2} + \kappa^2 (\gamma + \eta k^2)^2 + \frac{\partial \Omega^2}{\partial \ln r} (k_z V_A)^2 \\ &+ C_H \Omega \frac{k^2}{k_z^2} \left[\left((\gamma + \nu k^2 + \tau_{i0}^{-1})^2 + \frac{k_z^2}{k^2} \kappa^2 \right) \left(\frac{\partial \Omega}{\partial \ln r} + C_H \Omega \frac{k^2}{k_z^2} \right) + k_z^2 V_A^2 \left(4\Omega + \frac{\partial \Omega}{\partial \ln r} \right) \right] = 0 \end{aligned} \tag{5.39}$$

with the Hall parameter is defined as $C_H = (k_z^2 B_0)/(\mu_0 ne \Omega)$.

The dispersion relation in Eq. 5.39 has been color-coded to highlight the components due to dissipative MHD (black), the addition of the Hall term (blue), and the addition of the ion-neutral drag term (red). If $C_H = 0$ and $\tau_{i0}^{-1} = 0$, the expression reduces exactly to the standard MRI dispersion as written in [17]. The relation can be expanded and written instead in the form

$$\gamma^4 + C_3 \gamma^3 + C_2 \gamma^2 + C_1 \gamma + C_0 = 0 \tag{5.40}$$

where

$$\begin{aligned}
C_3 &= 2k^2(\eta+\nu)+2\tau_{i0}^{-1}\\
C_2 &= \kappa^2\frac{k_z^2}{k^2}+2(k_zV_A)^2+(\eta+\nu)^2k^4+2\eta\nu k^4+C_H\Omega\left(C_H\Omega\frac{k^2}{k_z^2}+\frac{\partial\Omega}{\partial\ln r}\right)\\
&\quad+\tau_{i0}^{-2}\left(1+2\nu k^2\tau_{i0}+4\eta k^2\tau_{i0}\right)\\
C_1 &= 2\eta\kappa^2k_z^2+2(\eta+\nu)k^2(k_zV_A)^2+2\nu\eta k^6(\eta+\nu)+2C_H\Omega\nu k^2\left(C_H\Omega\frac{k^2}{k_z^2}+\frac{\partial\Omega}{\partial\ln r}\right)\\
&\quad+2\tau_{i0}^{-1}C_H\Omega\left(\frac{\partial\Omega}{\partial\ln r}+\frac{C_H\Omega k^2}{k_z^2}\right)+2\tau_{i0}^{-1}\left(\eta k^4\left(2\nu+\eta+(\tau_{i0}k^2)^{-1}\right)+(k_zV_A)^2\right)\\
C_0 &= \eta^2k_z^2k^2\kappa^2+(k_zV_A)^4+\frac{\partial\Omega^2}{\partial\ln r}\frac{k_z^2}{k^2}(k_zV_A)^2+\nu\eta k^4(\nu\eta k^4+2(k_zV_A)^2)\\
&\quad+C_H\left((k_zV_A)^2\left(\frac{\kappa^2}{2}+2\Omega^2\right)+C_H\Omega^2\kappa^2+\frac{k_z^2}{2k^2}\kappa^2\frac{\partial\Omega^2}{\partial\ln r}+\nu^2k^4\left(\frac{1}{2}\frac{\partial\Omega^2}{\partial\ln r}+C_H\Omega^2\frac{k^2}{k_z^2}\right)\right)\\
&\quad+C_H\Omega\tau_{i0}^{-1}(2\nu k^2+\tau_{i0}^{-}1)\left(C_H\Omega\frac{k^2}{k_z^2}+\frac{\partial\Omega}{\partial\ln r}\right)+2\eta^2\tau_{i0}^{-2}\left(k^4\left(\nu k^2\tau_{i0}+\frac{1}{2}\right)+\frac{\tau_{i0}k^2(k_zV_A)^2}{\eta}\right)
\end{aligned}$$

If the terms due to ion-neutral collisions are ignored, the equation is identical to the Hall-MHD dispersion in [27].

5.2.3 Magnetohydrodynamic Stability Analysis

By specifying the geometry and plasma parameters, the azimuthal flow profiles can be calculated based on ion-neutral damped plasma Couette flow profile given by Eq. 4.3. The viscosity is assumed to be isotropic and is calculated using the unmagnetized value, which is acceptable as long as the applied seed field is weak and ions remain unmagnetized. Various approaches can be used to specify the local angular velocity, Ω, and the variables related to its radial derivative. In this analysis, these values are simply just evaluated at a chosen radial position. It is convenient to cast in terms of the scaled vorticity, $\zeta=(r\Omega)^{-1}\partial(r^2\Omega)/\partial r$, so that

$$\frac{\partial\Omega}{\partial\ln r}=(\zeta-2)\Omega \tag{5.41}$$

$$\frac{\partial\Omega^2}{\partial\ln r}=2\Omega^2(\zeta-2) \tag{5.42}$$

$$\kappa=\sqrt{4\Omega\zeta} \tag{5.43}$$

The wavenumbers used here are not necessarily the most unstable mode, but are based on the height of the plasma ($h = 0.52$ m) and the outer and inner radii, so that $k_z = \pi/h$, $k_r = \pi/(R_2 - R_1)$, and $k = \sqrt{k_r^2 + k_z^2}$. The four roots of Eq. 5.40 can be found using a built-in root finding routine in MATLAB, and the MRI occurs when the maximum real growth rate is positive.

In Figs. 5.4a-c, linear stability is analyzed in helium for three different (hypothetical) combinations of density and neutral pressure. These plasma densities of $2 \times 10^{10-11}$ cm^{-3} have been achieved experimentally, but only at higher neutral pressures 1×10^{-4} Torr. In all cases, $T_e = 8$ eV, $T_i = 0.1$ eV, and the velocity profile boundary conditions are fixed with $V_1 = 6$ km/s and $V_2 = 10$. The rotation properties for each combination of plasma settings are plotted in Figs. 5.4d-g, with asterisks marking the local values used for the analysis. The magnetic Reynolds number is defined here as $R_m = hV_\phi/\eta$, where $h = 0.52$ m is the height of the plasma, and $P_m = \nu/\eta$.

At these low densities, the standard MHD-MRI is either restricted to very weak seed field or absent entirely. The effect of Hall-MHD is obvious: a large growth rate appears when the magnetic seed field is antiparallel to the rotation axis (represented by negative Bz). Note that the ion inertial length at these densities, $d_i = c/\omega_{pi}$, is 1- 3.2 meters, much larger than the device size.

The first point is that, as neutral pressure is increased and the viscous diffusion length L_v decreases, the rotation profiles change from circular Couette (black) to neutral-damped (nearly identical blue and red). In going from Fig. 5.4(a$\rightarrow$ b) , the viscosity does not change, and the Hall-MHD growth rate decreases due to the decrease in the local rotation properties. This is in agreement with the Hall MRI growth rate relation that was derived in Balbus & Terquem [23], who found that $\gamma \propto \Omega(\zeta - 2)$. Next, if the density is then decreased (while maintaining the same rotation properties), the viscosity increases and the Hall-MHD growth rate further decreases, as shown in Fig. 5.4(b $\rightarrow$ c). The ion-neutral collision term also acts to decrease the growth rate.

A second point is that in the neutral-damped rotation profiles plotted in Fig. 5.4(d-g), $\Omega(r)$ begins *increasing* with radius for the outer half of the plasma. Thus, $\frac{d\Omega}{dr} > 0$ and the outer half of the plasma is no longer quasi-Keplerian flow. While the profiles in Fig. 5.4 were selected because they are hydrodynamically stable, regions of the plasma can become hydrodynamically unstable, for example, if the neutral pressure is further increased. The boundary between the

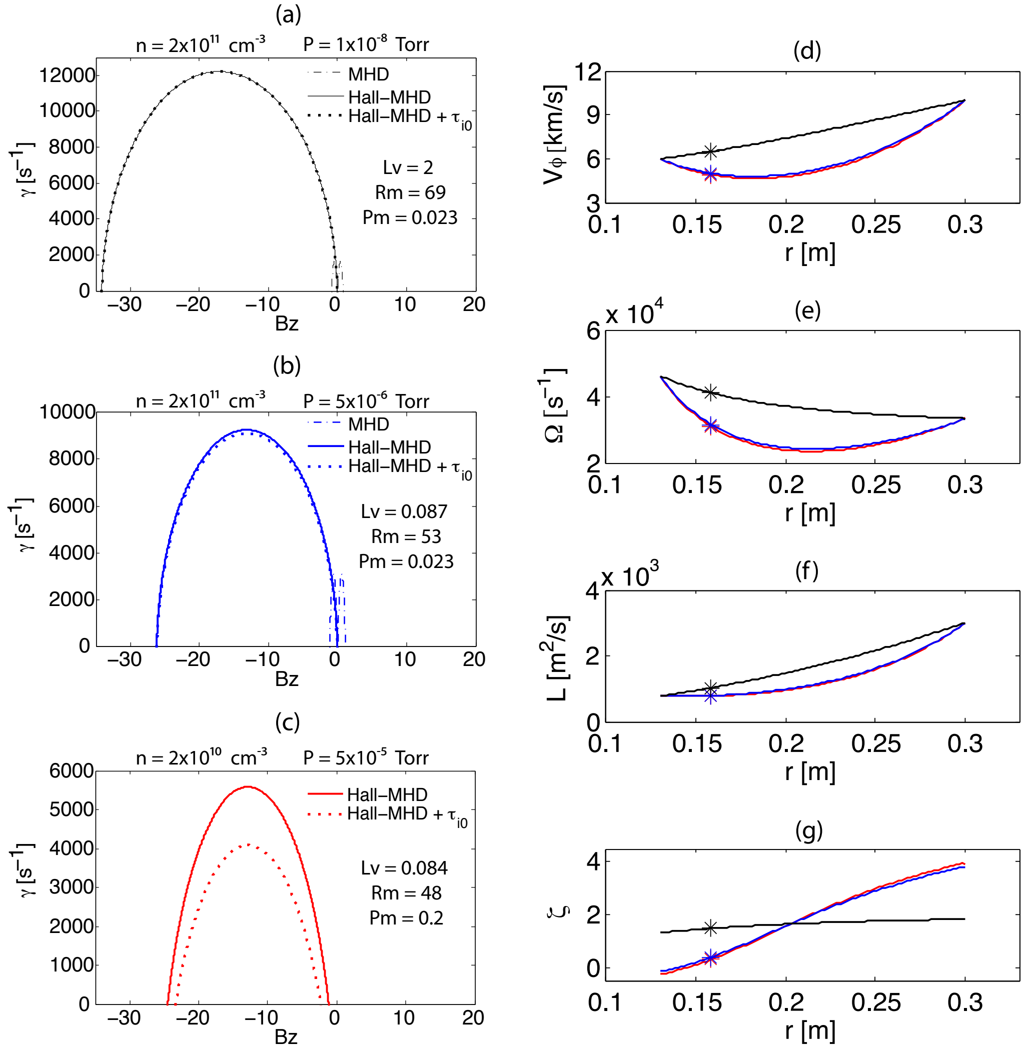

Figure 5.4: (a-c) Linear stability for helium, $T_e = 8$ eV, $T_i = 0.1$ eV, at various combinations of density and neutral pressure. (d-g) Rotation properties for the 3 different parameters in (a-c), with asterisks marking values used in analysis.

hydrodynamically unstable region and the hydrodynamically stable, MRI unstable region based on the local stability analysis will be explored in the next section.

5.2.4 Marginal Stability in Velocity Space at Realistic Experimental Parameters

Another useful approach is to map the MRI stability boundary in velocity space (V_1 vs. V_2). Using the same method in Section 5.2.3, the azimuthal flow profile is computed and local Hall-MRI dispersion (with ion-neutral collisions) is solved for each set of boundary conditions (V_1, V_2). Again, if $\gamma > 0$, the flow is Hall-MRI unstable. An example of a stability diagram for argon is shown in Fig. 5.5. The parameters used here are based on those measured in spinning Argon plasma listed in Table 3.1, with $T_i = 0.14$ eV, $T_e = 6$ eV, $n = 3 \times 10^{10}$ cm^{-3}, and P=1×10^{-6} Torr. The local dispersion relation is solved at $r = 0.16$ m with $Bz = -10$ Gauss, which indicates instability in Region (III).

Hydrodynamic stability can be found by setting $Bz = 0$, thereby eliminating all terms with V_A and C_H. As in Section 5.1.3, it is assumed that the the transition between stability and instability occurs through $\gamma = 0$. In that case, Eq. 5.40 leads to the stability requirement for the dimensionless vorticity parameter:

$$\zeta \geq \frac{-k^2}{2k_z^2\Omega^2}\left[\nu^2 k^4 + \tau_{i0}^{-2}\left(1 + 2\nu k^2 \tau_{i0}\right)\right] \tag{5.44}$$

In purely inviscid flow with no ion-neutral collisions, the Rayleigh condition for stability ($\zeta \geq 0$) is recovered. The results of the WKB analysis (Eq. 5.44) are plotted along with the hydrodynamic stability predicted by the vortex-shape perturbation used in Section 5.1.3. It should be noted that the with $Bz = 0$, the WKB analysis does not exactly agree with the hydrodynamic stability analysis, because the WKB analysis assumes the value for the radial wavenumber, kr, which is a less-exact approach compared to incorporating the radial information into the perturbation amplitude, as done in Section 5.1.3. Solving the dispersion relation using the WKB approach is useful for understanding the general importance of each term, but a more exact MHD analysis should follow the technique used in Section 5.1.3. In Fig. 5.5, region (I) is centrifugally unstable according

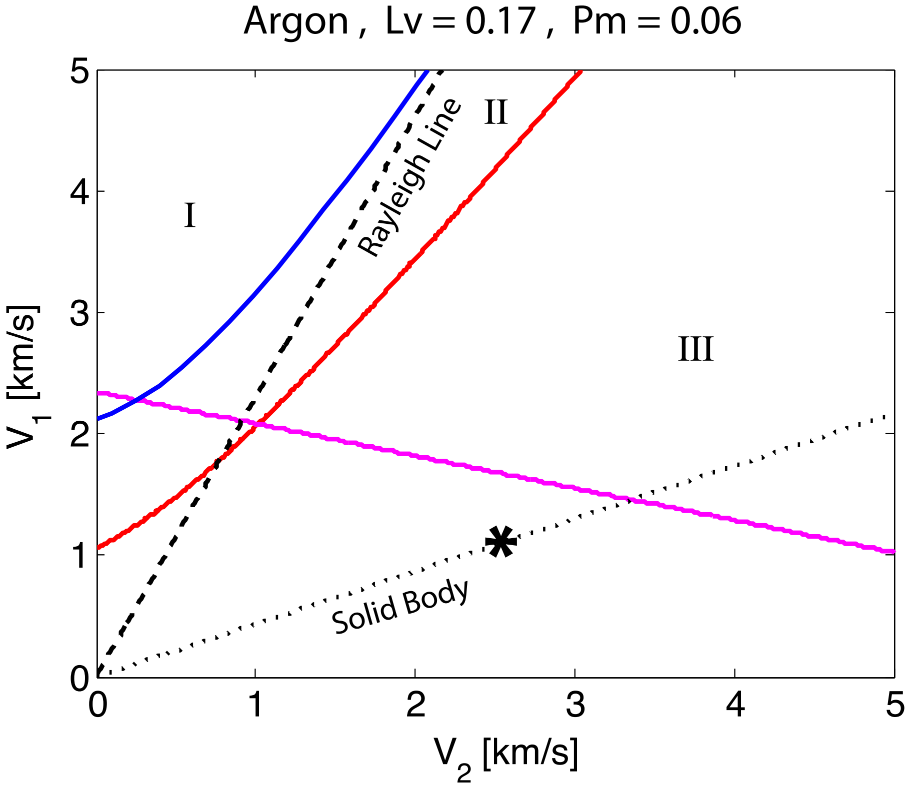

Figure 5.5: Stability diagram for argon at $r = 0.16$ m with $Bz = -10$ Gauss, $T_i = 0.14$ eV, $T_e = 6$ eV, $n = 3 \times 10^{10}$ cm^{-3}, and $P = 1 \times 10^{-6}$ Torr. The asterisk marks flow that has been achieved at these parameters experimentally, without a magnetic seed field. Region (I) is centrifugally unstable according to the eigenvalue analysis in Section 5.1.3. Region (II) is centrifugally unstable according to the WKB analysis with $Bz = 0$. Region (III) is Hall-MRI unstable.

to the eigenvalue analysis in Section 5.1.3, while Region (II) is centrifugally unstable according to the WKB analysis with $Bz = 0$ (Eq. 5.44).

Interestingly, Fig. 5.5 indicates that the Hall-MRI is unstable for rotation profiles with $\frac{d\Omega}{dr} \geq 0$. This is consistent with Balbus & Terquem [23], who noted that the Hall MRI can destabilize for *any* differential rotation profile, even if the angular velocity is increasing with radius. While a solid-body rotation profile might not look like an accretion disk, it is relatively easy to produce in the PCX experiment. As marked by the asterisk in Fig. 5.5, the flow that has been achieved at these parameters experimentally, without a magnetic seed field, is intriguingly close to that needed for instability.

5.2.5 Generating MRI Relevant Flows In PCX

In order to pursue quasi-Keplerian flows with $\frac{d}{dr}(r^2\Omega) > 0$ and $\frac{d\Omega}{dr} < 0$, rotation was also driven at the inner boundary of PCX (see Fig. 2.2 for a diagram of the inner boundary stirring assembly). As mentioned in Section 3.2.1, the position of the inner boundary electrodes was optimized to drive helium flow. Rotation profiles in helium (with no vertical magnetic field), measured by a radially scanned Mach probe at the midplane, are shown in Fig. 5.6. Flow speeds peaked at 3.5 km/s at the inner boundary and 12 km/s in the magnetized region at the outer boundary. A summary of the measured plasma parameters can be found in Table 5.1. Of course, the question is, can the MRI be unstable in any of these flows?

As shown in Fig. 5.7, it is apparent that stability is quite sensitive to slight changes in the ion temperature, density, and neutral pressure. The plasma parameters in Fig. 5.7a are representative of those produced in the experiment, except that experimentally, larger neutral pressures (at least $P = 1 \times 10^{-4}$ Torr) are needed to maintain the discharge. A stability diagram based on the parameters measured in case labeled “5 / 550 V” in Table 5.1 is shown in Fig. 5.7b, which indicates that a larger Prandtl number requires a larger flows and stronger magnetic seed field to destabilize.

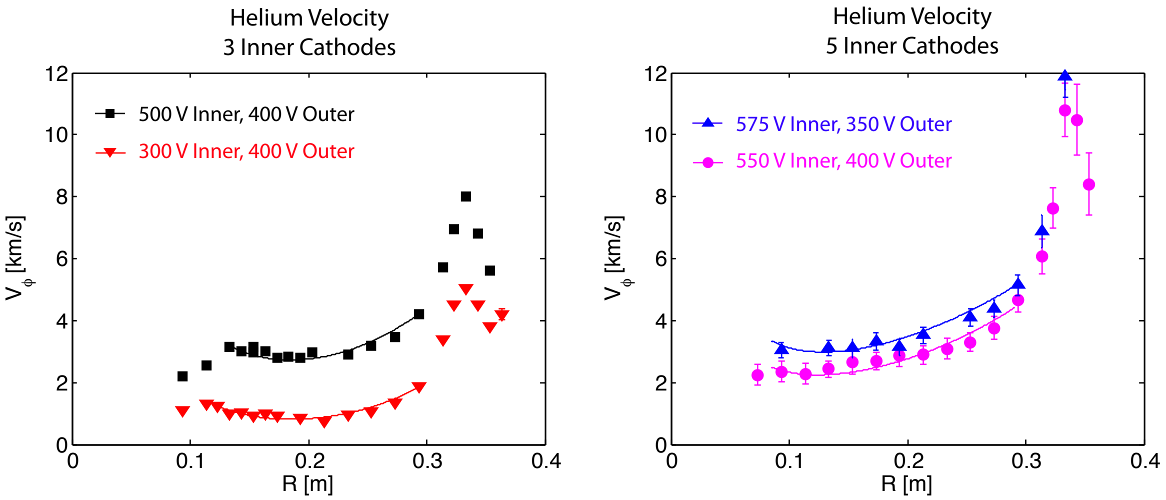

(a) (b)

Figure 5.6: Helium azimuthal velocity measurements with both inner and outer boundary flow drive, but with no vertical seed field applied.

# Inner Cathodes / **Bias Voltage**	**n x 10^{11}** (cm^{-3})	f_{ion} %	**Te** (eV)	**Ti**$_{fit}$ (eV)	**Rm**$_1$	**Rm**$_2$	**Pm**
3 / 300 V	1.7	0.35	5.9	0.11	5.1	19	0.2
3 / 500 V	1.8	0.37	5.3	0.22	10	25	0.88
5 / 550 V	2.4	0.74	6.5	0.25	11	46	1.3
5 / 575 V	2.3	0.65	7.5	0.32	17	64	2.9

Table 5.1: Summary of rotation driven at both inner and outer boundary.

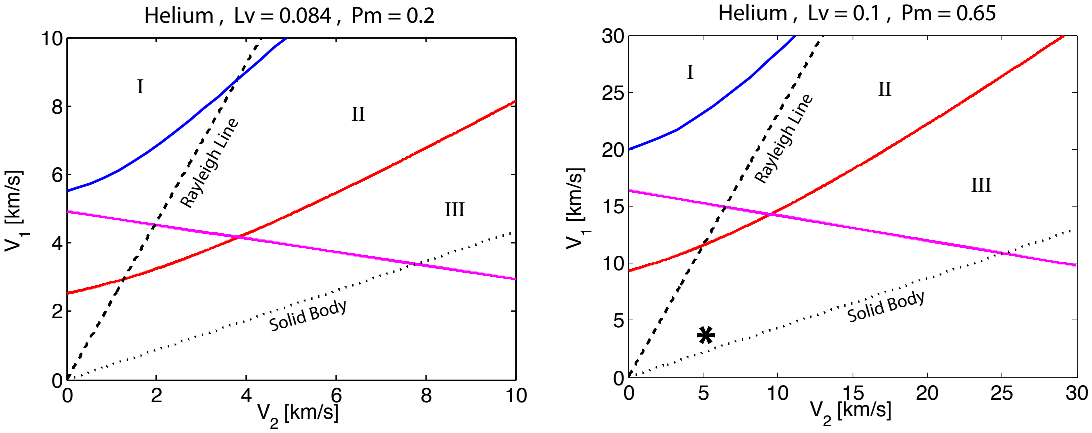

(a) (b)

Figure 5.7: Stability diagrams for helium at at r=0.16 m with a) $Bz = -5$ Gauss, $T_e = 8$ eV, $T_i = 0.1$ eV, $n = 2 \times 10^{10}$ cm^{-3}, and $P = 5 \times 10^{-5}$ Torr, and b) $Bz = -20$ Gauss, $T_i = 0.2$ eV, $T_e = 7$ eV, $n = 3 \times 10^{10}$ cm^{-3}, and P=1×10^{-4} Torr. Flow achieved at these parameters without a magnetic seed field applied is marked by asterisk.

5.2.6 Prospects for Observing the MRI in PCX

In PCX, the primary effect of the neutrals on the MRI is through modification of the flow profile itself, causing increased shear but lower azimuthal velocities compared to a neutral-free, "ideal" Couette flow profile. A secondary effect is the decrease of the Hall-MRI growth rate. Another significant factor which determines MRI growth is plasma viscosity. In PCX, it has been recognized that plasma flow is optimized at low density (where viscosity is largest) and a low neutral pressure (where neutral drag is minimized). However, high viscosity also tends to damp out perturbations, making it more difficult to excite instabilities such as the MRI or even Taylor vortices. At high viscosity, larger flow rates are required for instability. Unfortunately, as long as the plasma is partially ionized, flow speeds are apparently limited by the critical ionization velocity. A fully ionized plasma presumably does not have such velocity limits.

Besides parameter optimization and engineering improvements, it would be helpful to compute mode structures and amplitudes with global simulations at low plasma densities with the inclusion of ion-neutral damping. Experiments characterizing the MRI will need to compare the onset threshold to theoretical and numerical predictions, look for altered velocity profiles due to momentum transport during nonlinear saturation, and identify two-fluid effects expected to arise from the Hall term and plasma-neutral interactions. Better measurements of plasma parameters with improved diagnostics, including full probe arrays to define mode structures, will be essential for comparing to theory.

Chapter 6

Summary and Future Work

The Plasma Couette Experiment has been constructed, and a new technique for spinning weakly magnetized plasma has been successfully demonstrated. In the experiment, plasma is confined by a cylindrical bucket assembly of permanent magnets, arranged in rings of alternating polarity, to form an axisymmetric cusp magnetic field. The field is localized to the boundaries, leaving a large, unmagnetized plasma in the bulk with $T_e < 10$ eV and $n = 10^{10} - 10^{11}$ cm^{-3} produced by microwave heating. The plasma is stirred using $\mathbf{J} \times \mathbf{B}$ torques, where current is driven by toroidally-localized electrostatically biased electrodes in the magnetized edge region. Electrode assemblies have been constructed to induce flow at both the inner and outer boundaries of the plasma.

Most notably, the Mach probe profile measurements show that the azimuthal flow viscously couples momentum from the magnetized edge into the unmagnetized bulk. Measurements at several toroidal positions have also confirmed that the axisymmetric magnetic geometry effectively imposes an azimuthal symmetry on the flow. Interestingly, the presence of neutrals allows for measurement of plasma viscosity. Measured flow profiles are in excellent agreement with a model based on a Bessel function solution for the steady-state velocity profile, which assumes that the main ion momentum loss mechanism is ion-neutral collisions. The measured viscosity agrees with Braginskii's formula up to a factor of T_i.

A number of experimental observations have been made which strongly support the concept that the plasma is indeed rotating due to the edge-applied $\mathbf{J} \times \mathbf{B}$ forces:

1. Bulk plasma flow, as measured by Mach probes, is only observed when cathodes are biased.

2. Rotation is in the direction of expected $\mathbf{E} \times \mathbf{B}$ flow, the flow changes direction when the electric field is reversed.

3. The measured flow increases with applied bias voltage and cathode emission current.

4. There exists an optimal electrode location for inducing flow. This is consistent with the idea that the electrodes must be in a strong enough magnetic field to induce flow, but not too strong, as momentum coupling to the bulk is inhibited since Braginskii viscosity decreases with magnetization.

5. It has been recognized that plasma conditions are optimized at low density (where viscosity is largest) and a low neutral pressure (where neutral drag is minimized). Time-dependent flow measurements in discharges with puffed gas follow this theory, showing increased rotation as density decreases and neutrals are pumped out.

6. A self-consistent, rotation-induced radial electric field is measured. It only appears when there is flow, it scales with the magnitude of the flow and the ion mass, and it is in agreement with the predicted profile calculated from fitted velocity measurements.

7. The T_e measurements of Langmuir probes have been independently confirmed by a newly developed Optical Emission Spectroscopy technique, leading to further confidence in the *magnitude* of the Mach probe velocity measurements. Furthermore, the T_e profiles are flat, so the changes in potential profiles are an important confirmation of Mach probe measurements.

8. The rotation drive is spatially localized. Vertically scanned Mach probes show that rotation is only observed near the biased cathodes, and is absent at the unbiased cathodes. That is, if only the two central cathodes are biased, rotation is induced exclusively at the midplane and exponentially decreases away from the midplane, in agreement with theory. If all cathodes are biased, the entire column of plasma spins.

9. Flow is also observed at the inner boundary, where the geometry is slightly different with smaller cathodes and stronger center stack magnets.

10. Maximum speed limits have been observed for various gas species (He $\sim$ 12 km/s, Ne $\sim$ 4 km/s, Ar $\sim$ 3.2 km/s, Xe $\sim$ 1.4 km/s), consistent with the well documented but poorly understood critical ionization velocity limit phenomenon, which exists in partially ionized plasma.

The ability to create a sheared, unmagnetized Couette flow of plasma, driven by biased electrodes in the magnetized edge, is a major advance for carrying out future flow-driven MHD experiments. An analytical model has been developed to understand the flow profiles based on Braginskii viscosity and momentum loss through ion-neutral charge exchange, and the model very accurately matches the flow measurements. Flows can be adjusted in the experiment to mimic those of accretion disks, making it possible to study, for the first time, the magnetorotational instability in a plasma. From an experimental point of view, the ingredients for MRI seem simple: a hydrodynamically stable Keplerian-like flow of a conducting fluid should suddenly be destabilized by an applied, weak magnetic seed field. In the experiment, the Hall effect, which may also be relevant in proto-planetary disks, will likely play a role in MRI onset. Large growth rates are expected to appear only when the magnetic seed field is anti-parallel to the rotation axis. Global Hall-MHD simulations for PCX have been performed by Ebrahimi [27], which predict that the MRI is feasible with magnetic fields of only 10 Gauss, assuming fully ionized helium plasma at densities $> 10^{11}$ cm^{-3} with 6 km/s Keplerian flow profiles. In Section 5.2.3, the local WKB stability analysis at the current parameters in PCX seems to indicate that high viscosity, while excellent for efficiently spinning the plasma, also tends to damp perturbations, making it harder to access MRI unstable regimes. The presence of neutrals primarily affects the flow profiles, but can also dampen the MRI growth rate.

6.1 Future Work

It seems that the next steps for PCX are clear. The MRI can be created by learning to operate with:

- Higher plasma density (lower viscosity)

- Lower neutral density
- Vertical magnetic seed field

Spinning the plasma at higher plasma densities would make it easier to excite the MRI. In PCX, it was difficult to spin at high density due to arcing and destruction of the biased cathodes, the cause of which was not fully understood. Cathode behavior might be better understood through further studies of the edge region in overdense plasmas. Perhaps this problem can be solved by using a different cathode material and design. Improvements to the LaB_6 cathode design are currently being tested on the recently constructed, much larger Madison Plasma Dynamo Experiment at the University of Wisconsin. It may be that cathode materials such as CeB_6 may work even better, which could be explored on PCX. Moving away from tungsten filaments might also help to keep probes clean. Over time, the insulating surfaces became coated with a conducting material (probably tungsten), to the point that the probes required cleaning after only about several dozen plasma pulses. Design improvements should also be made to the inner cathodes, which were particularly vulnerable and would burn out with just a few accidental arcs.

Rotation would improve at increased ionization fractions, which could be accessed through additional vacuum pumping and stronger multicusp magnets for better confinement. On PCX, confinement could be improved by replacing the first generation of ceramic magnets on the endcaps and outer boundaries with a second generation of the high-field, neodymium type. Additional microwave power and launching of X-mode waves ($\mathbf{E} \perp \mathbf{B}$), which are not restricted by density cutoffs, could also be explored.

Of course, the next step also involves demonstrating that MRI-relevant plasma parameters and flow can also be generated with the applied seed field. Center stack stirring electrodes are currently located in a region where $Bz_{min} \approx 20$ Gauss, so the position of the electrodes will need to be adjusted to achieve maximum flow drive as the vertical seed field is applied. An automated mechanism for adjusting cathode position would be ideal.

Global simulations at low plasma densities ($10^{10} - 10^{11}$ cm^{-3}) which include ion-neutral damping, along with a better understanding of the boundary conditions (which are complicated by the multicusp field), will be helpful in fully characterizing the behavior of the MRI in PCX. A sophisticated diagnostics campaign will be required, as accurate measurements of plasma parameters will be essential for comparing to theory and simulations. For example, the plasma density is an important parameter which has thus far only been measured with Langmuir probes collecting ion saturation current, which become less understood in flowing plasmas. Non-invasive optical measurements like interferometry would be preferable. Ion temperature has also not been measured reliably, but is especially crucial for calculating viscosity. Perhaps the MRI is already occurring in PCX, but detection requires internal Mach probe and magnetic probe arrays, which will need to be able to measure the unstable regions of the plasma without causing significantly plasma loss and undesirable perturbations of plasma parameters.

Finally, the cylindrical geometry of PCX lends itself to a long list of future possibilities. It could be feasible to access the helical MRI mode by adding a toroidal magnetic field in addition to the vertical seed field. In addition to the present Taylor-Couette flow drive scheme, a combination of radial current drive and axial magnetic field would result in an additional, bulk $\mathbf{J} \times \mathbf{B}$ force to drive azimuthal flow. It may be possible to excite the MRI in this type of "Taylor-Dean" flow [82]. The experiment could also be arranged to generate cylindrical Von Kármán flow, in which the top and bottom halves of the plasma could be made to rotate in opposite directions, forming two, coaxial, counterrotating disks. Cylindrical Von Kármán flow is predicted to generate a laminar magnetic dynamo at parameters which may be experimentally accessible, as predicted by numerical simulations with the NIMROD code using Hall-MHD and PCX geometry [83]. Ultimately, the results of this thesis have shown that plasma experiments which create flow-driven instabilities such as the MRI and dynamo are well within reach, marking the beginning of an exciting era of laboratory plasma astrophysics.

References

[1] M. J. McCaughrean, K. R. Stapelfeldt, and L. M. Close. High-Resolution Optical and Near-Infrared Imaging of Young Circumstellar Disks. In *Protostars and Planets IV*, page 485. Tuscon: Univ. Arizona Press, 2000.

[2] J. Frank, A. King, and D. Raine. *Accretion Power in Astrophysics*. Cambridge University Press, 3 edition, 2002.

[3] S.A. Balbus. Enhanced Angular Momentum Transport in Accretion Disks. *Annu. Rev. Astron. Astrophys.*, 41:555–97, 2003.

[4] S.A. Balbus and J.F. Hawley. Instability, Turbulence and Enhanced Transport in Accretion Disks. *Rev. Mod. Phys.*, 70:1, 1998.

[5] N.I. Shakura and R.A. Sunyaev. Black Holes in Binary Systems: Observational Appearance. *Astron. Astrophys.*, 24:337, 1973.

[6] U. Frisch and S.A. Orszag. Turbulence: Challenges for Theory and Experiment. *Phys. Today*, 43:24, 1990.

[7] S.A. Balbus and J.F. Hawley. Transport in Accretion Disks. *Phys. Plasmas*, 6:4444, 1999.

[8] L. Rayleigh. On the Dynamics of Rotating Fluid. *Proc. R. Soc. Lond.*, A93:148–154, 1916.

[9] H. Ji, M. Burin, E. Schartman, and J. Goodman. Hydrodynamic Turbulence Cannot Transport Angular Momentum Effectively in Astrophysical Disks. *Nature*, 444:343, 2006.

[10] E.P. Velikhov. Stability of an Ideally Conducting Liquid Flowing Between Cylinders Rotating in a Magnetic Field. *Soviet Phys.-JETP*, 36:995–998, 1959.

[11] S. Chandrasekhar. The Stability of Non-dissipative Couette Flow in Hydromagnetics. *Proc. Natl. Acad. Sci.*, 46:253–257, 1960.

[12] S.A. Balbus and J.F. Hawley. A Powerful Local Shear Instability in Weakly Magnetized Disks. I. Linear Analysis. *Astrophys. J.*, 376:214, 1991.

[13] J.F. Hawley. Global Magnetohydrodynamical Simulations of Accretion Tori. *Astrophys. J.*, 528:462, 2000.

[14] J.F. Hawley. Global Magnetohydrodynamic Simulations of Cylindrical Keplerian Disks. *Astrophys. J.*, 554:534, 2001.

[15] J.F. Hawley, C.F. Gammie, and S.A. Balbus. Local Three-dimensional Magnetohydrodynamic Simulations of Accretion Disks. *Astrophys. J.*, 440:742, 1995.

[16] P.-Y. Longaretti and G. Lesur. MRI-Driven Turbulent Transport: The Role of Dissipation, Channel Modes and Their Parasites. *Astron. Astrophys.*, A51:516, 2010.

[17] H. Ji, J. Goodman, and A. Kageyama. Magnetorotational Instability in a Rotating Liquid Metal Annulus. *Mon. Not. Roy. Astron. Soc.*, 325:L1–L5, 2001.

[18] A. Roach, E. Spence, C. Gissinger, E. Edlund, P. Sloboda, J. Goodman, and H. Ji. Observation of a Free-Shercliff-Layer Instability in Cylindrical Geometry. *Phys. Rev. Lett.*, 108:154502, 2012.

[19] C. Gissinger, J. Goodman, and H. Ji. The Role of Boundaries in the Magnetorotational Instability. *Phys. Fluids*, 24:074109, 2012.

[20] F. Stefani, T. Gundrum, G. Gerbeth, G. Rudiger, M. Schultz, J. Szklarski, and R. Hollerbach. Experimental Evidence for Magnetorotational Instability in a Taylor-Couette Flow Under the Influence of a Helical Magnetic Field. *Phys. Rev. Lett.*, 97:184502, 2006.

[21] C. Gissinger, H. Ji, and J. Goodman. Instabilities in Magnetized Spherical Couette Flow. *Phys. Rev. E.*, 84:026308, 2011.

[22] M. Wardle. The Balbus-Hawley Instability in Weakly Ionized Discs. *Mon. Not. Roy. Astron. Soc.*, 307:849, 1999.

[23] S.A. Balbus and C. Terquem. Linear Analysis of the Hall Effect in Protostellar Disks. *Astrophys. J.*, 552:235, 2001.

[24] K. Noguchi and V. Pariev. Magnetorotational Instability in a Couette Flow of Plasma. *AIP Conf. Proc.*, 692:285, 2003.

[25] Z. Wang, J. Si, W. Liu, and H. Li. Equilibrium and Magnetic Properties of a Rotating Plasma Annulus. *Physics of Plasmas*, 15:102109, 2008.

[26] E.G. Zweibel and C. Heiles. Magnetic Fields in Galaxies and Beyond. *Nature*, 385:131, 1997.

[27] F. Ebrahimi, B. Lefebvre, C.B. Forest, and A. Bhattacharjee. Global Hall-MHD Simulations of Magnetorotational Instability in the Plasma Couette Flow Experiment. *Phys. Plasmas*, 18: 062904, 2011.

[28] R. Limpaecher and K.R. MacKenzie. Magnetic Multipole Containment of Large Uniform Collisionless Quiescent Plasmas. *Rev. Sci. Instrum.*, 44:726, 1973.

[29] K.N. Leung, N. Hershkowtitz, and K.R. MacKenzie. Plasma Confinement by Localized Cusps. *Phys. Fluids*, 19:1045, 1976.

[30] A. Lang and N. Hershkowitz. Multidipole Plasma Density. *J. Appl. Phys.*, 49:4707, 1978.

[31] M-H. Cho, N. Hershkowitz, and T. Intrator. Particle and Power Balance of Hot-Filament Discharge Plasmas in a Multidipole Device. *J. Appl. Phys.*, 67:3254, 1990.

[32] J. Ghosh, R. Elton, H. Griem, A. Case, A.W. DeSilva, R.F. Ellis, A. Hassam, R. Lunsford, and C. Teodorescu. Radially Resolved Measurements of Plasma Rotation and Flow-Velocity Shear in the Maryland Centrifugal Experiment. *Phys. Plas.*, 13:022503, 2006.

[33] R.J. Taylor, M.L. Brown, B.D. Fried, H. Grote, J.R. Liberati, G.J. Morales, and P. Pribyl. H-mode Behavior Induced by Cross-Field Currents in a Tokamak. *Phys. Rev. Lett.*, 63:2365, 1989.

[34] A. Almagri, J.T. Chapman, C. S. Chiang, D. Craig, D.J. Den Hartog, C. C. Hegna, and S. C. Prager. Momentum Transport and Flow Damping in the Reversed-Field Pinch Plasma. *Phys. Plasmas*, 5:3982, 1998.

[35] D. Craig, A.F. Almagri, J.K. Amderson, J.T. Chapman, C.-S. Chiang, N.A. Crocker, D.J. Den Hartog, G. Fiksel S., C. Prager, J.S. Sarff, and M.R. Stoneking. Enhanced Confinement with Plasma Biasing in the MST Reversed Field Pinch. *Phys. Rev. Lett.*, 79:1865, 1997.

[36] M. Krishnan, M. Geva, and J. L. Hirshfield. Plasma Centrifuge. *Phys. Rev. Lett.*, 46:36, 1981.

[37] B. Lehnert. Rotating Plasmas. *Nucl. Fusion.*, 11:485, 1971.

[38] C. Collins, N. Katz, J. Wallace, J. Jara-Almonte, I. Reese, E. Zweibel, and C.B. Forest. Stirring Unmagnetized Plasma. *Phys. Rev. Lett.*, 108:115001, 2012.

[39] N. Katz, C. Collins, J. Wallace, M. Clark, and D. Weisberg. Magnetic Bucket for Rotating Unmagnetized Plasma. *Rev. Sci. Instrum.*, 83:063502, 2012.

[40] E. Spence, K. Reuter, and C.B. Forest. Numerical Simulations of a Spherical Plasma Dynamo Experiment. *Astrophys. J.*, 700:470–478, 2009.

[41] R. Limpaecher and K.R. MacKenzie. Magnetic Multipole Containment of Large Uniform Collisionless Quiescent Plasmas. *Rev. Sci. Instrum.*, 44(6):726–731, 1973.

[42] K.W. Ehlers and K.N. Leung. Characteristics of the Berkeley Multicusp Ion Source. *Rev. Sci. Instrum.*, 50:1353, 1979.

[43] C.M. Cooper, W. Gekelman, P. Pribly, and Z. Lucky. A New Large Area Lanthanum Hexaboride Plasma Source. *Rev. Sci. Instrum.*, 81:083503, 2010.

[44] L. Pomathiod, R. Debrie, Y. Arnal, and J. Pelletier. Microwave Excitation of Large Volumes of Plasma at Electron Cyclotron Resonance in Multipolar Confinement. *Phys. Lett. A*, 106A (7):301–304, 1984.

[45] H. Amemiya and S. Ishii. Electron Energy Distribution in Multicusp-Type ECR Plasma. *Jpn. J. Appl. Phys.*, 28(11):2289–2297, 1989.

[46] M. Moisan and Z. Zakrzewski. Plasma Sources Based on the Propagation of Electromagnetic Surface Waves . *J. Phys. D: Appl. Phys.*, 24:1025–1048, 1991.

[47] M. Tuda, K. Ono, H. Ootera, M. Tsuchihashi, M. Hanazaki, and T. Komemura. Large-Diameter Microwave Plasma Source Excited By Azimuthally Symmetric Surface Waves. *J. Vac. Sci. Technol. A*, 18(3):840–848, 2000.

[48] M. Lieberman and A. Lichtenberg. *Principles of Plasma Discharges and Materials Processing*. John Wiley and Sons, Inc., 2 edition, 2005.

[49] W. Brattain and J. Becker. Thermionic and Adsorption Characteristics of Thorium on Tungsten. *Phys. Rev.*, 43:428, 1933.

[50] K.N. Leung, P.A. Pincosy, and K.W. Ehlers. Directly Heated Lanthanum Hexaboride Filaments. *Rev. Sci. Instrum.*, 55:1064, 1984.

[51] E. A. Lederer. Filaments and Cathodes, Part I. In *Vacuum Tube Design*, pages 1–10. RCA Manufacturing Company, 1940.

[52] T. Intrator, M.H. Cho, E.Y. Wang, N. Hershkowitz, D. Diebold, and J. DeKock. The Virtual Cathode as a Transient Double Sheath. *J. Appl. Phys.*, 64:2927, 1988.

[53] M. Hudis and L.M. Lidsky. Directional Langmuir Probe. *J. Appl. Phys.*, 41:5011, 1970.

[54] I. H. Hutchinson. The Invalidity of a Mach Probe Model. *Phys. Plasmas*, 9:1832, 2002.

[55] L. Oksuz and N. Hershkowitz. Understanding Mach Probes and Langmuir Probes in a Drifting, Unmagnetized, Non-Uniform Plasma. *Plasma Sources Sci. Technol.*, 13:263–271, 2004.

[56] I. H. Hutchinson. Ion Collection by a Sphere in a Flowing Plasma: I. Quasineutral. *Plasma Phys. Control. Fusion*, 44:1953, 2002.

[57] I. H. Hutchinson. Ion Collection by a Sphere in a Flowing Plasma: 2. Non-Zero Debye Length. *Plasma Phys. Control. Fusion*, 45:1477, 2003.

[58] E. Ko and N. Hershkowitz. Asymmetry Reversal of Ion Collection by Mach Probes in Flowing Unmagnetized Plasmas. *Plasma Phys. Control. Fusion*, 48:621, 2006.

[59] N. Hershkowitz. How Langmuir Probes Work. In *Plasma Diagnostics*, pages 113–183. Academic Press, Inc., 1989.

[60] S. Chen and T. Sekiguchi. Instantaneous Direct Display System of Plasma Parameters By Means of Triple Probe. *J. Appl. Phys.*, 36:2363, 1965.

[61] J. B. Boffard, R. O. Jung, C. C. Lin, and A. E. Wendt. Optical Emission Measurements of Electron Energy Distributions in Low-Pressure Argon Inductively Coupled Plasmas. *Plasma Sources Sci. Technol.*, 19:065001, 2010.

[62] M.J. Goeckner, J. Goree, and T.E. Sheridan. Laser Induced Fluorescence Characterization of a Multidipole Filament Plasma. *Phys. Fluids*, 3:2913, 1991.

[63] S.I. Braginskii. Transport Processes in a Plasma. *Rev. Plasma Phys.*, 1:250, 1965.

[64] N. Brenning. Review of the CIV Phenomenon. *Space Sci. Rev.*, 59:209–314, 1992.

[65] S. Lai. A Review of Critical Ionization Velocity. *Rev. Geophys.*, 39:471–506, 2001.

[66] H. Helm. The Cross Section for Symmetric Charge Exchange of He+ in He at Energies Between 0.3 and 8 eV. *J. Phys. B: At. Mol. Phys.*, 10:3683, 1977.

[67] Y. Kaneko, N. Kobayashi, and I. Kanomata. Low Energy Ion-Neutral Reactions. *J. Phys. Soc. Jpn.*, 27:992, 1969.

[68] R. Hegerberg, M.T. Elford, and H.R. Skullerud. The Cross Section for Symmetric Charge Exchange of Ne+ in Ne and Ar+ in Ar at Low Energies . *J. Phys. B: At. Mol. Phys.*, 15:797, 1982.

[69] J. Miller, S. Pullins, D. Levandier, Y. Chiu, and R. Dressler. Xenon Charge Exchange Cross Sections for Electrostatic Thruster Models. *J. Appl. Phys.*, 91:984, 2002.

[70] N. Hershkowitz, K.N. Leung, and T. Romesser. Plasma Leakage Through a Low-beta Line Cusp. *Phys. Rev. Lett.*, 35:277, 1975.

[71] J.A. Wesson. Poloidal Distribution of Impurities in a Rotating Tokamak Plasma. *Nucl. Fusion*, 37:577, 1997.

[72] I. H. Hutchinson. *Principles of Plasma Diagnostics*. Cambridge University Press, 2 edition, 2002.

[73] I. V. Khalzov, B.P. Brown, N. Katz, and C.B. Forest. Modeling the Parker Instability in a Rotating Plasma Screw Pinch. *Phys. Plasmas*, 19:022107, 2012.

[74] B.W. James and S.W. Simpson. Isotope Separation in the Plasma Centrifuge. *Plasma Physics*, 18:289, 1976.

[75] T. Ohkawa and R.L. Miller. Band Gap Ion Mass Filter. *Physics of Plasmas*, 9:5116, 2002.

[76] A.J. Fetterman and N.J. Fisch. The Magnetic Centrifugal Mass Filter. *Physics of Plasmas*, 18(9):094503, 2011.

[77] A.P. Willis and C.F. Barenghi. A Taylor-Couette Dynamo. *Astron. Astrophys.*, 393:339–343, 2002.

[78] C.D. Andereck, S.S. Liu, and H.L. Swinney. Flow Regimes in a Circular Couette System with Independently Rotating Cylinders. *J. Fluid Mech.*, 164:155–183, 1986.

[79] O. Czarny, E. Serre, P. Bontoux, and R. Lueptow. Interaction Between Ekman Pumping and the Centrifugal Instability in Taylor-Couette Flow. *Phys. Fluids*, 15:467, 2003.

[80] S. Chandrasekhar. *Hydrodynamic and Hydromagnetic Stability*. Clarendon Press, Oxford, 3 edition, 1961.

[81] O. Blaes and S. Balbus. Local Shear Instabilities in Weakly Ionized, Weakly Magnetized Disks. *Astrophys. J.*, 421:163–177, 1994.

[82] F. Stefani and G. Gerbeth. MRI in Taylor-Dean Flows. *AIP Conf. Proc.*, 733:100, 2004.

[83] I.V. Khalzov, B.P. Brown, F. Ebrahimi, D.D. Schnack, and C.B. Forest. Numerical Simulation of Laminar Plasma Dynamos in a Cylindrical Von Kármán Flow. *Phys. Plasmas*, 18:032110, 2011.

[84] T. Shikama, S. Kado, A. Okamoto, S. Kajita, and S. Tanaka. Practical Formula for Mach Number Probe Diagnostics in Weakly Magnetized Plasmas. *Phys. Plasmas*, 12:044504, 2005.

[85] J.E. Maggs, T.A. Carter, and R.J. Taylor. Transition from Bohm to Classical Diffusion Due to Edge Rotation of a Cylindrical Plasma. *Phys. Plasmas*, 14:052507, 2007.

[86] G.I. Taylor. Stability of a Viscous Liquid Contained Between Two Rotating Cylinders. *Phil. Trans. R. Soc. Lond*, 223:289, 1923.

Appendix A:
PCX Data Acquisition System

The LabVIEW Real-Time platform allows us to develop and debug all of the LabVIEW VIs and files using the graphical LabVIEW environment on the host computer (PCX Control) and save the entire collection under a single NI LabVIEW Real-Time Project. LabVIEW files are then uploaded and executed on a stand-alone CompactRIO Real-Time target. The CompactRIO system has an embedded processor and real-time operating system that specifically runs the RT Engine and LabVIEW VIs. Meanwhile, LabVIEW VIs running on the host computer can communicate over the network with VIs running on the Real-Time target to provide real-time user interface. Additional computers running LabVIEW VIs can also be added (i.e. Midna) and can communicate using network published variables.

In MDSplus, data is stored into a hierarchical tree structure. On PCX, data is stored in two trees on our MDSplus server, Ooccoo. The CompactRIO data is stored in the pdp tree at 100 samples/sec with 1 second per segment, while the DTACQ data is stored in pcxdata tree at 10,000 samples/sec with 8 seconds per segment. Data is backed up to a 7TB, RAID 5 array (PCX Data) and can be accessed on the local campus network for analysis with Matlab or IDL.

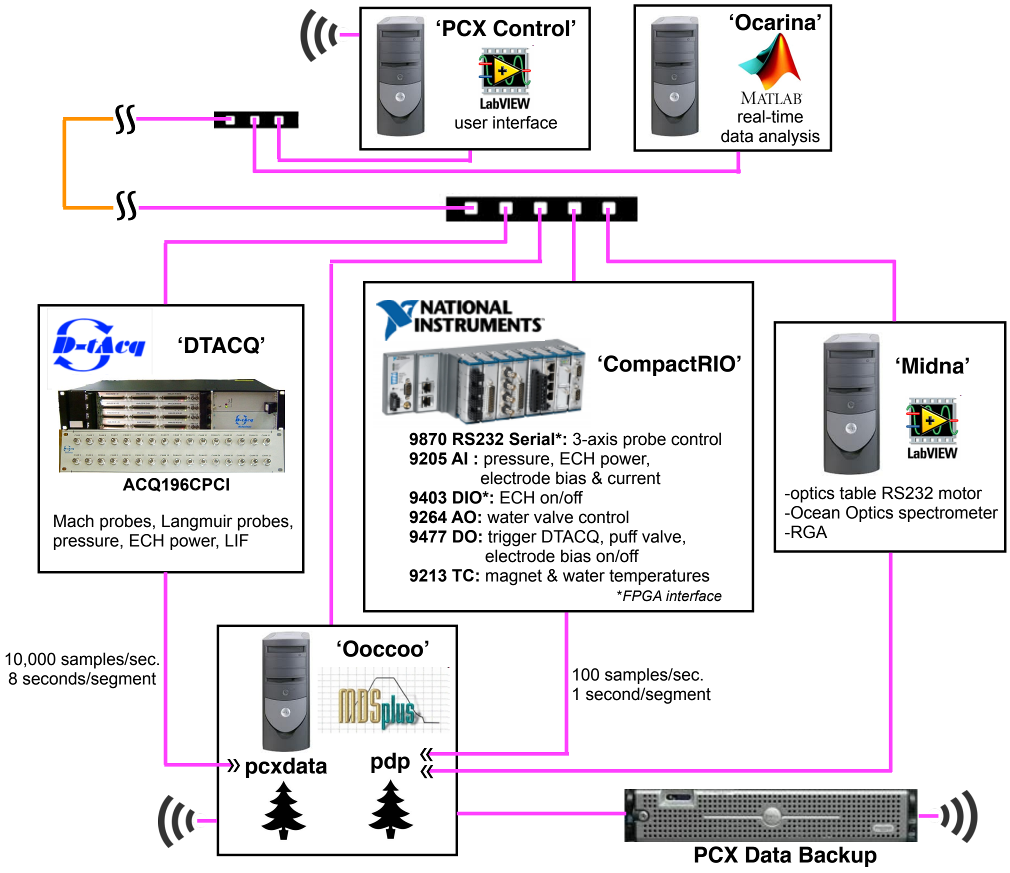

Figure A.1: PCX data acquisition system. More detailed information is available at the UW Plasma Physics PCX Wiki (http://hackserver.physics.wisc.edu/wiki/index.php/PCX).

Appendix B:
Probe Circuit Diagrams

There are quite a few circuits involved in the many probe diagnostics on PCX. For reference, some of the most essential circuits are shown here. The most important and fail-proof component, which has been used in all PCX probe circuits, is the isolation amplifier (Fig. B.1). These boards were originally designed by Mikhail Reyfman and David Deicher and are widely used in the UW Plasma Physics Group.

The mach probe circuits simply use isolation amplifiers to measure the voltage across a resistor inline with a negatively biased probe tip. The triple probe circuit uses three isolation amplifiers to measure the ion saturation current and the floating and bias voltages with respect to machine ground. The triple probe circuit is shown in Fig. B.2.

The swept Langmuir probe circuit (Fig. B.3) is considerably more complicated. The circuit is based on a design by Dr. David Hannum and was built for PCX by Mikhail Reyfman and David Deicher. A BK Precision function generator, two DC power supplies, and a high power op amp (PB58) are used to supply the probe with a triangle wave (usually 100 Hz) swept from -90 V to 20 V with respect to ground. Isolation amplifiers are used to measure swept voltage and current (through a variable resistor R_j). After a few accidental probe shorting incidents, the original op-amp (PB58A) has since been replaced with a slightly less powerful and less expensive PB58 (150 V / 1.5 A), and an inline fuse has been installed at the output to the probe for added protection.

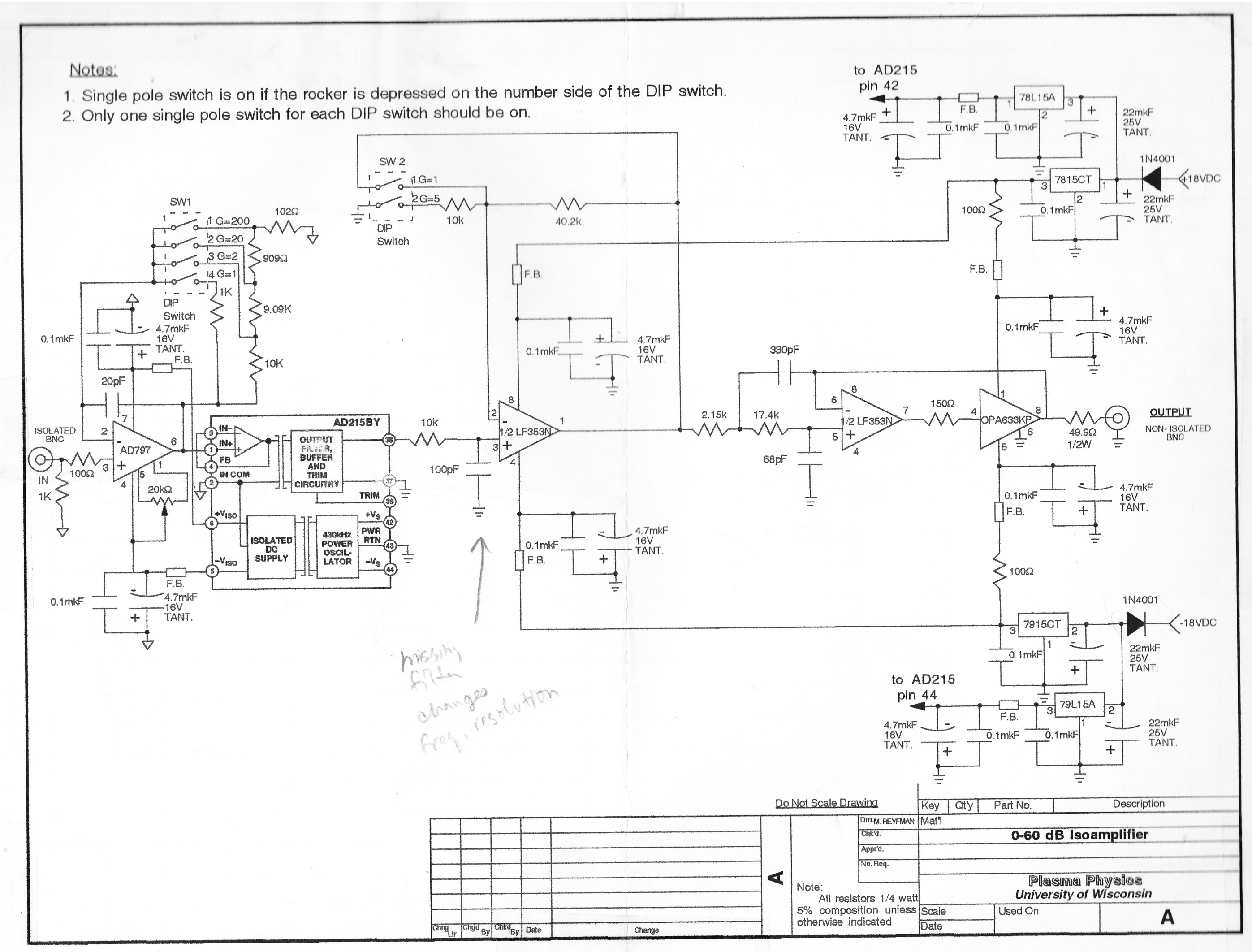

Figure B.1: AD215 Isolation amplifier circuit. Note that the input impedence is only 1 kΩ to ground. In some cases, this resistor has been swapped for 10 kΩ.

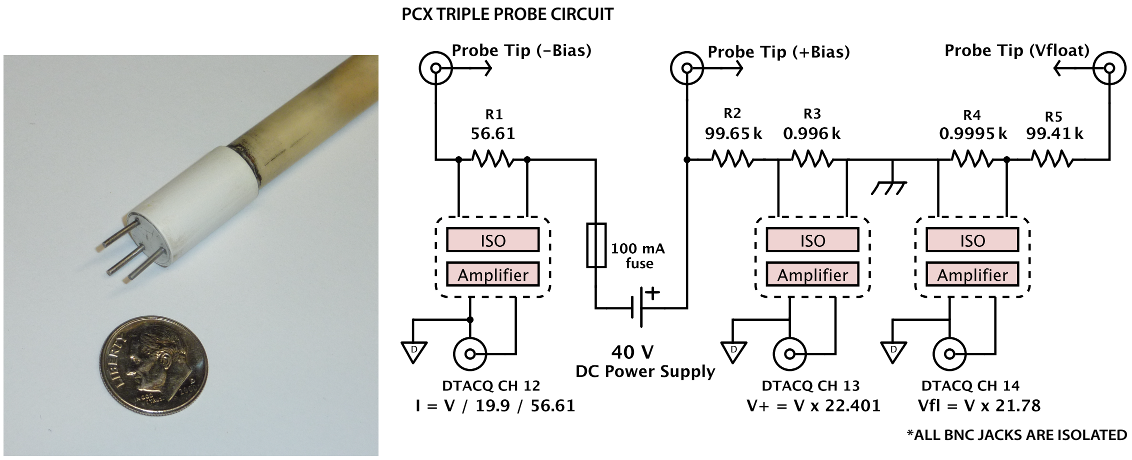

Figure B.2: Triple probe and triple probe circuit.

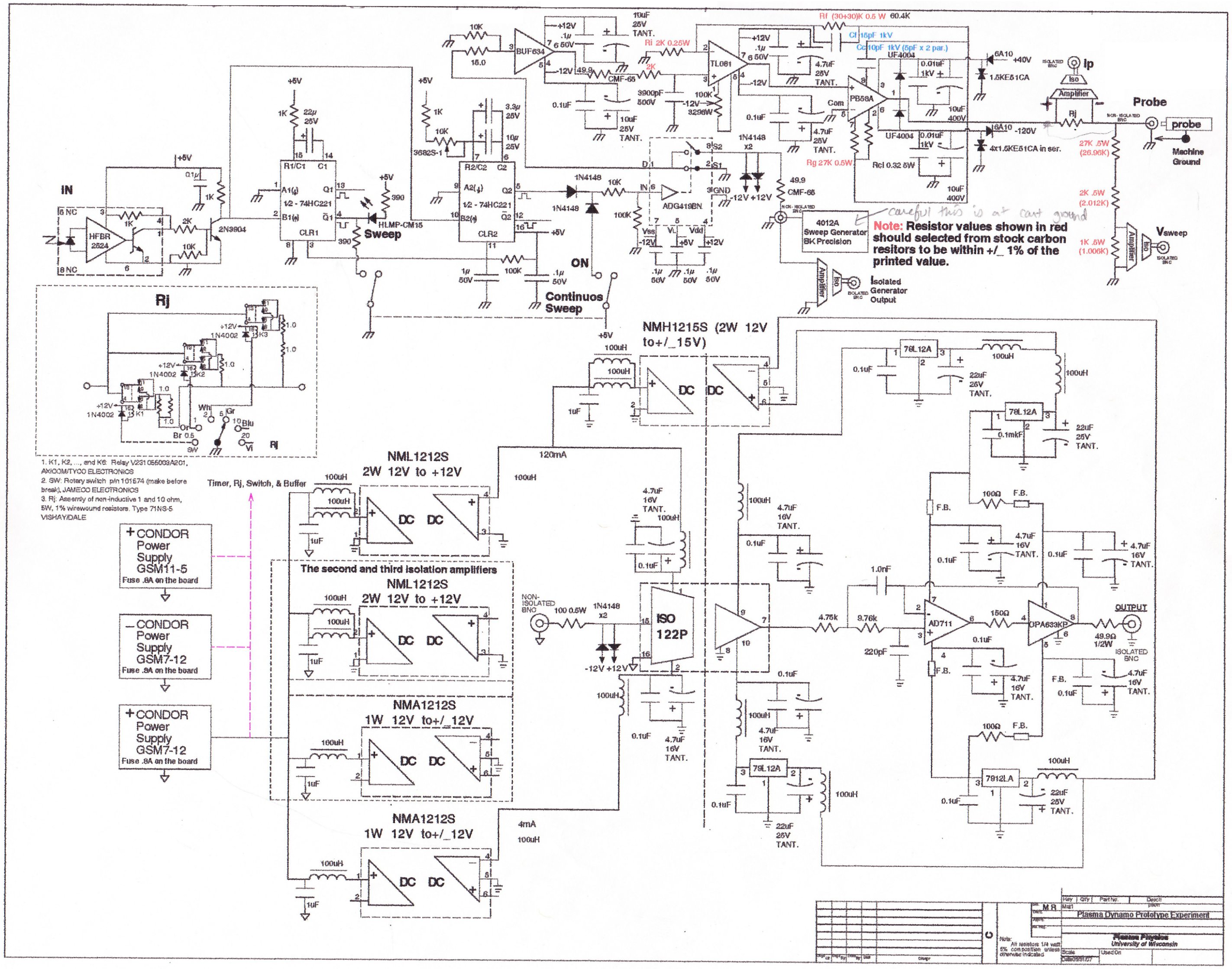

Figure B.3: Swept Langmuir probe circuit.

Appendix C:
Measurements in the Strongly Magnetized Cusp Field Region

The strongly magnetized edge region is highly complicated by sharp gradients in density, temperature, and magnetic cusp field. In an effort to understand how the diamagnetic, $\mathbf{E} \times \mathbf{B}$, ∇B, and curvature drifts determine ion flow, measurements were taken using Mach probe, single swept langmuir probe, the floating potential rake probe, and LIF at 668 nm and 1047 nm, as shown in Figs. C.2 and C.3. Note that these measurements were made when the cathodes were biased -350 V with respect to the floating anodes, but the measurements were made at the midplane in the region behind the anode and the face of the magnets, denoted "limiter" in these figures.

In the magnetized region, the orientation of the Mach probe tips with respect to the magnetic field can affect the absolute flow velocity measurement [84]. More accurate measurements can be obtained using the formula as presented in [85];

$$K \ln R_{\pm 45} = M_{||} \mp \frac{1}{\sqrt{2}} M_{\perp} \tag{C.1}$$

where $M_{||}$ and $M_{\perp}$ are the parallel and perpendicular Mach numbers, and $R_{\pm 45}$ is the ratio of the ion saturation current collected by two oppositely facing Mach probe tips with tip normal $\pm 45°$ to the magnetic field (see Fig. C.1). The constant K is taken as $K = 1.34$ (as done in Section 2.6.1). Solving for the perpendicular Mach number leads to

$$V_{\perp} = C_s \frac{\sqrt{2}}{2} K (\ln R_{-45} - \ln R_{+45}) \tag{C.2}$$

where $C_s = 9.79 \times 10^3 \sqrt{(5/3) T_e(r)/\mu}$ depends on the radially varying temperature (which is measured by the swept Langmuir probe).

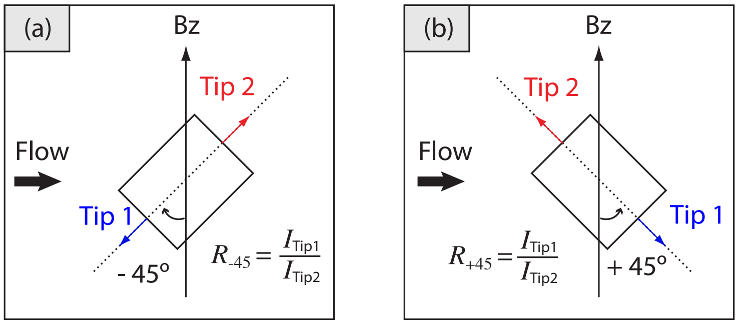

Figure C.1: In the magnetized edge, the Mach probe was rotated a) $-45°$ or b) $+45°$ with respect to the vertical B field.

The expected drifts can be estimated by taking into account radial gradients in both T_i and n ($T_i' > 0$ and $n' < 0$), so that for ions:

$$\mathbf{V_{di}} = -\frac{\nabla P \times \mathbf{B}}{enB^2} = \frac{T_i}{B_z}\frac{|n'|}{n}(-\hat{\phi}) + \frac{|T_i'|}{B_z}(+\hat{\phi}) \tag{C.3}$$

$$\mathbf{V_{\nabla B}} + \mathbf{V_{curv}} = \frac{1}{2}v_\perp r_L \frac{\mathbf{B} \times \nabla B}{B^2} + \frac{M_i v_{||}^2}{eB^2}\frac{\mathbf{R_c} \times \mathbf{B}}{R_c^2} = r_L v_{ti}\frac{|B'|}{B_z}(+\hat{\phi}) \tag{C.4}$$

$$\mathbf{V_{ExB}} = \frac{\mathbf{E} \times \mathbf{B}}{B^2} \tag{C.5}$$

where r_L is the ion gyroradius and v_{ti} is the ion thermal velocity. The floating potential measurements can be combined with T_e measurements to find the plasma potential using $\Phi_p = \Phi_{fl} - \frac{T_e}{2}(\ln(2\pi m_e/m_i) - 1)$ [72].The radial electric field is $E_r = -\Phi_p'$, and $|\mathbf{V_{ExB}}| = E_r/B_z$. It is not clear why the E/B velocity predicted by the floating potential measurements and magnetic field simulated by Maxwell SV (Eq. 2.1) is several orders of magnitude larger than anything measured by Mach probes or LIF, as shown in Fig. C.3b. One caveat of the rake probe is that the floating potential tips were oriented to measure plasma in the region approximately 1 cm above the plane of the mach probe, which probably doesn't make a difference in the bulk unmagnetized plasma, but could matter in the edge region where sharp spatial gradients exist.

It was assumed that $n_e = n_i$, so that gradients in n_e measured by the Langmuir probe can be used to compute ion diamagnetic drift. Furthermore, LIF measurements indicated a gradient in T_i which is also assumed to be representative of the entire ion population in this region. The sum

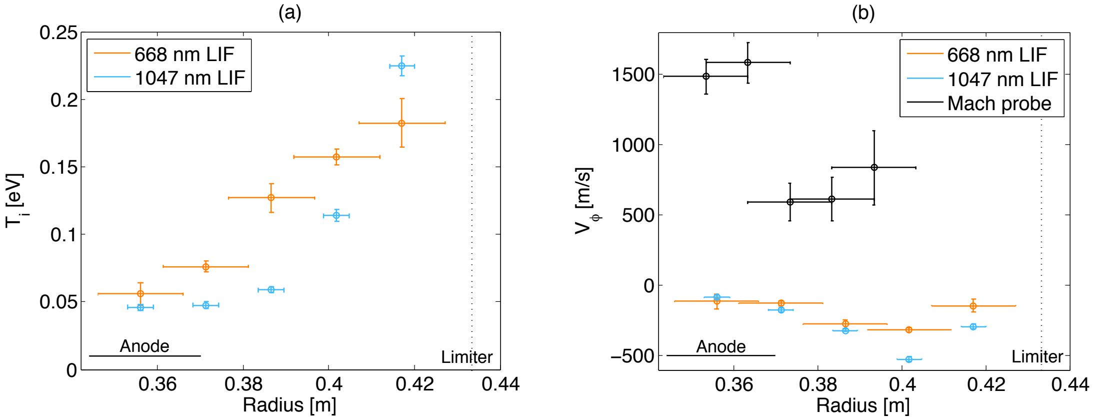

Figure C.2: Comparison of 1047 nm and 668 nm LIF measurements of Ti and V_ϕ in the cusp field region at midplane (same plane as anode) in argon plasma with -350 V biased cathodes. The LIF velocity measurements do not agree with Mach probe. The Mach probe velocity in (b) was computed using the T_e measurements in Fig. C.3c.

of the ion diamagnetic, ∇B, and curvature drifts seems to match the Mach probe measurements in both magnitude and sign. However, the LIF velocity measurements indicate flow opposite that measured by the Mach probe (Fig. C.2b). The Mach probe measures $+\hat{\phi}$ flow induce by the stirring anode at $r \sim 0.36$ m, which is the expected direction of flow induced by the electrostatic stirring assembly. The orientation of the magnetic field has also been confirmed by measurements with a handheld Gaussmeter. Still, the cusp field region remains poorly understood.

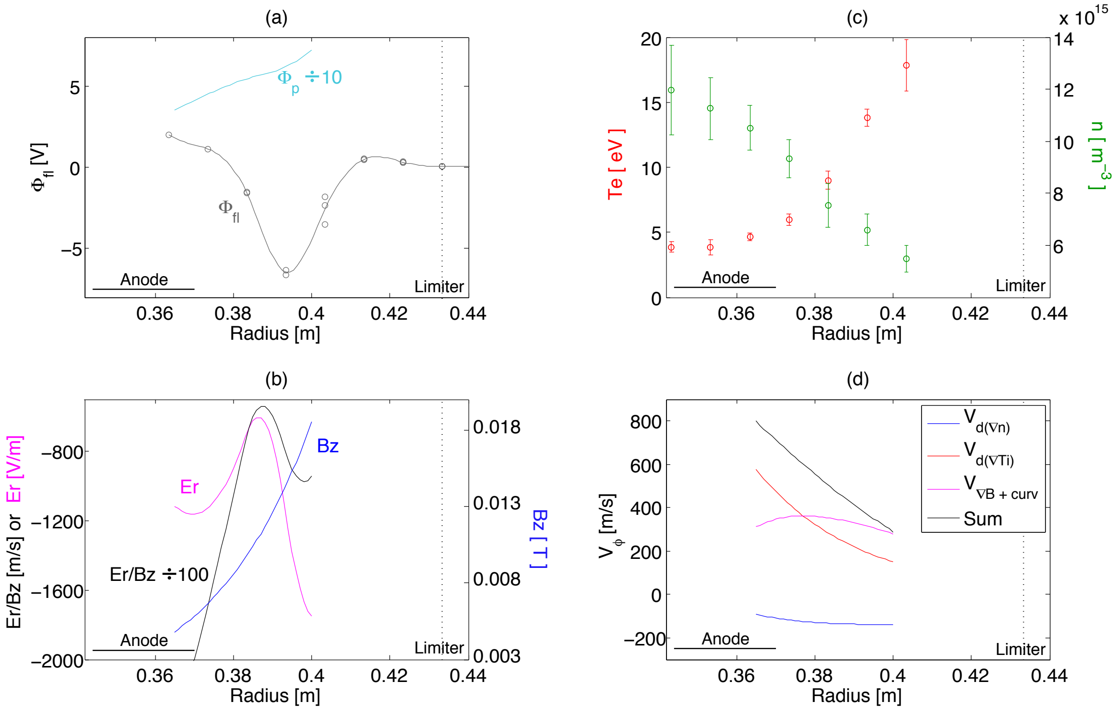

Figure C.3: Study of cusp field region at midplane (same plane as anode) in argon plasma with -350 V biased cathodes. a) Floating potential measurements (with spline fit) and Φ_p (calculated using T_e measurements in (c)). b) Computed E_r/B_z velocity in edge cusp field, which seems several orders of magnitude too large. c) n and T_e measured by swept Langmuir probe. d) Computed ion diamagnetic, ∇B and curvature drifts based on measured n, T_i (from LIF), and simulated magnetic field. The sum is comparable in magnitude to the velocity measurements in Fig. C.2b but does not agree in sign with the LIF measurements.

Appendix D:
Details in Solving the Linear Stability of Taylor Vortices

The goal is to use the following system of equations to estimate the velocities required for the onset of Taylor vortices in the experiment:

$$\frac{\nu}{k^2}\left[DD_* - \left(k^2 + \frac{1}{\tau_{i0}\nu} + \frac{\gamma}{\nu}\right)\right]\left(DD_* - k^2\right)u = \frac{2V_0}{r}v \tag{D.1}$$

$$\left[DD_* - \left(k^2 + \frac{1}{\tau_{i0}\nu} + \frac{\gamma}{\nu}\right)\right]v = \frac{(D_* V_0)u}{\nu} \tag{D.2}$$

where $D = \frac{d}{dr}$ and $D_* = \frac{d}{dr} + \frac{1}{r}$. Since an analytical solution was not easy to find, the numerical solution was achieved with the assistance of Dr. Ivan Khalzov. The algebraic details of the method are outlined here in case others would like to use it in the future.

The approach is to calculate marginal stability by first setting $\gamma = 0$ and then transforming the above set of equations into a generalized eigenvalue problem,

$$\mathrm{A}\mathbf{u} = \lambda \mathrm{B}\mathbf{u} \tag{D.3}$$

to solve for λ using MATLAB. In this problem, λ is the fluid Reynold's number of the inner cylinder, $Re_1 = V_1 L/\nu$, where L is a characteristic length scale. The matrices A and B depend on physical parameters in the system and the fluid Reynold's number of the outer cylinder, $Re_2 = V_2 L/\nu$.

To begin, Eqs. D.1 and D.2 are non-dimensionalized, so that $r \to r/L$, $k \to k/L$. Taking $\gamma = 0$, $\alpha^2 = L(\tau_{i0}\nu)^{-1}$, and multiplying by r, we have

$$r\left\{\left[DD_* - \left(k^2 + \alpha^2\right)\right]\left(DD_* - k^2\right)u = \frac{k^2}{\nu}\frac{2LV_0}{r}v\right\} \tag{D.4}$$

$$r\left\{\left[DD_* - \left(k^2 + \alpha^2\right)\right]v = \frac{L}{\nu}(D_* V_0)u\right\} \tag{D.5}$$

Note that $DD_*f(r) = \frac{d}{dr}\left(\frac{1}{r}\frac{d(rf(r))}{dr}\right)$. With the change of variables $x = r^2$, then $rDD_*f(r) = 4xD_{xx}\left(rf(r)\right)$, where $D_{xx} = \frac{d^2}{dx^2}$, resulting in:

$$\left[4xD_{xx} - \left(k^2+\alpha^2\right)\right]\left(4xD_{xx} - k^2\right)(ru) = \frac{2Lk^2}{\nu}(V_0)(rv) \tag{D.6}$$

$$\left[4xD_{xx} - \left(k^2+\alpha^2\right)\right](rv) = \frac{L}{\nu}(D_*V_0)(ru) \tag{D.7}$$

The right hand sides can be evaluated using the equilibrium solution for the velocity function (from Eq. 4.3)

$$\begin{aligned} V_0 &= C_1I_1(\alpha r) + C_2K_1(\alpha r) \\ C_1 &= \frac{K_1(\alpha R_2)V_1 - K_1(\alpha R_1)V_2}{D} \\ C_2 &= \frac{I_1(\alpha R_1)V_2 - I_1(\alpha R_2)V_1}{D} \\ D &= I_1(\alpha R_1)K_1(\alpha R_2) - I_1(\alpha R_2)K_1(\alpha R_1) \end{aligned} \tag{D.8}$$

In order to separate the inner and outer boundary velocities and eventually solve for Re_1, the equilibrium velocity function is written in the form

$$\begin{aligned} V_0 &= S_1V_1 + S_2V_2 \\ S_1 &= \frac{1}{D}\left[K_1(\alpha R_2)I_1(\alpha r) - I_1(\alpha R_2)K_1(\alpha r)\right] \\ S_2 &= \frac{1}{D}\left[I_1(\alpha R_1)K_1(\alpha r) - K_1(\alpha R_1)I_1(\alpha r)\right] \end{aligned} \tag{D.9}$$

The derivatives of the modified Bessel function can be found using known identities, leading to:

$$\begin{aligned} D_*V_0 &= T_1V_1 + T_2V_2 \\ T_1 &= \frac{\alpha}{D}\left[K_1(\alpha R_2)I_0(\alpha r) + I_1(\alpha R_2)K_0(\alpha r)\right] \\ T_2 &= -\frac{\alpha}{D}\left[K_1(\alpha R_1)I_0(\alpha r) + I_1(\alpha R_1)K_0(\alpha r)\right] \end{aligned} \tag{D.10}$$

Denoting $\nabla_{xx} = 4xD_{xx} - k^2$, Eqs. D.6 and D.7 become

$$(\nabla_{xx} - \alpha^2)\nabla_{xx}(ru) = \frac{2Lk^2}{\nu}(S_1V_1 + S_2V_2)(rv) \tag{D.11}$$

$$(\nabla_{xx} - \alpha^2)(rv) = \frac{L}{\nu}(T_1V_1 + T_2V_2)(ru) \tag{D.12}$$

Making use of the definitions $Re_1 = V_1 L/\nu$ and $Re_2 = V_2 L/\nu$, the system can be conveniently written as

$$\begin{bmatrix} -Re_2 T_2 & \nabla_{xx} - \alpha^2 \\ \nabla_{xx}\nabla_{xx} - \alpha^2 \nabla_{xx} & -2Re_2 k^2 S_2 \end{bmatrix} \mathbf{u} = Re_1 \begin{bmatrix} T_1 & 0 \\ 0 & 2k^2 S_1 \end{bmatrix} \mathbf{u} \tag{D.13}$$

To solve, the spatial derivatives are discretized using the finite difference method over N intervals in x with step size h, so that $u''(x) = \frac{u(x+h)-2u(x)+u(x-h)}{h^2}$, with boundary conditions $u(R_1) = u(R_2) = 0$. After k and α are specified based on the physical dimensions and parameters, the stability in Re_1, Re_2 space is found from the minimum eigenvalue, Re_1, for each Re_2. It is worth noting that the code properly solves for stability in the limit of $\alpha \to 0$ when the equilibrium flow is simply Couette flow, as shown in Fig. D.1.

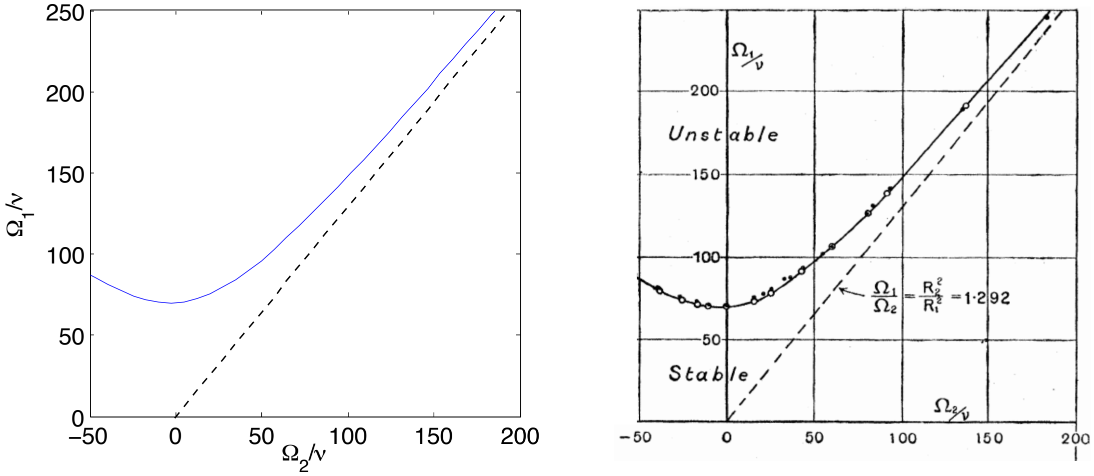

(A) (B)

Figure D.1: Excellent agreement is found between (A) the eigenvalue solver results and (B) Taylor's original calculations for $R_1 = 3.55$ cm and $R_2 = 4.035$ cm [86]. The eigenvalue solver precisely matches Taylor's calculated minimum threshold value of $\Omega_1/\nu = 69.8$.